The Thesis committee for Keith Joseph Faria
Certifies that this is the approved version of the following thesis:

Doubly-Fed Induction Generator based Wind Power Plant Models

APPROVED BY

SUPERVISING COMMITTEE:

Supervisor: ________________________________

Surya Santoso

____

W. Mack Grady

Doubly-Fed Induction Generator based Wind Power Plant Models

by

Keith Joseph Faria, B.Tech.

THESIS

Presented to the Faculty of the Graduate School of
The University of Texas at Austin
in Partial Fulfillment
of the Requirements
for the Degree of

Master of Science in Engineering

THE UNIVERSITY OF TEXAS AT AUSTIN
December 2009

Dedicated to my parents, Ronald and Petronella, who have always supported me in all my endeavours.

Acknowledgments

This thesis is an important milestone in my life. It represents the fulfillment of my childhood dream of completing a postgraduate degree in engineering. I have managed to reach this point and complete this thesis only as a result of the many experiences I have encountered and the encouragement and support that I have received from some remarkable individuals who I wish to acknowledge.

First and foremost I wish to thank my advisor, Prof. Surya Santoso. He has been enthusiastic about my work since the day I met him. He immediately gave me good topics in power system modeling to work on. Ever since, Dr. Santoso has supported me not only by providing me with teaching and research assistant positions over these past two years, but also academically and emotionally through the rough road to finish this thesis. Thanks to him I had the opportunity to work in various simulation environments and real-life machines. He also gave me the opportunity to intern and co-op at a wind energy company which has greatly enhanced my knowledge. He came up with the thesis topic and guided me through its development. And during the most difficult times while writing this thesis, he gave me the moral support and the freedom I needed to move on.

I would like to thank the National Renewable Energy Laboratory (NREL) and the National Science Foundation (NSF) for providing the funding and data required for the completion of this thesis. The model guidelines provided by the Western Electricity Coordinating Council (WECC) have been invaluable starting points for all the models developed.

There have been many special people who have been instrumental in encouraging me in my career. To name the ones that stand out most of all, I would like to thank my undergraduate advisors, Prof. B.G.Fernandes and Prof. B.N.Chaudhari; my teachers Prof. M.Prakash and Prof. B.Madhani; and my teacher and friend Mr. S.Kantarao. I wish to thank my colleague and friend, Mohit Singh, for all the help and input he gave me during the course of my research uptil the completion of this thesis. This thesis was made possible largely due to the brainstorming we would do on the models developed. I would also like to thank my friend Gysler Castelino who was always there to help me and clear my doubts.

I would like to end with India, where the most basic source of my life energy resides: my family. I have been blessed to be part of an amazing family, unique in many ways. Their support has been unconditional all these years; they have given up many things so that I could be at UT Austin; they have cherished with me every great moment and supported me whenever I needed it. Words don't do justice to what I feel, but I wish to thank my dear Dad, Mom and little sister Michelle for everything. I owe it all to them.

Statement of Originality and Academic Integrity

I certify that I have completed the online ethics training modules[1], particularly the Academic Integrity Module[2], of the University of Texas at Austin - Graduate School. I fully understand, and I am familiar with the University policies and regulations relating to Academic Integrity, and the Academic Policies and Procedures.[3]

I also attest that this thesis/dissertation is the result of my own original work and efforts. Any ideas of other authors, whether or not they have been published or otherwise disclosed, are fully acknowledged and properly referenced.

I also acknowledge the thoughts, direction, and supervision of my research advisor, Prof. S. Santoso.

---

[1] The University of Texas at Austin - Graduate School's online ethics training modules, http://www.utexas.edu/ogs/ethics/

[2] The University of Texas at Austin - Graduate School's online ethics training on academic integrity, http://www.utexas.edu/ogs/ethics/transcripts/academic.html

[3] The University of Texas at Austin, General Information, 2006-2007, Chapter 11, Sec. 11 - 101, http://www.utexas.edu/student/registrar/catalogs/gi06-07/app/appc11.html

Division of Labour

The research required for this thesis was done by Keith Faria and Mohit Singh under the supervision and guidance of Dr. S. Santoso. The following shows who took the lead for various parts of the project.

Keith Faria

- Model development in phasor-domain
- Model performance testing in phasor-domain
- Model validation in phasor-domain
- Case V-4 validation of model in time-domain

Mohit Singh

- Model development in time-domain
- Model performance testing in time-domain
- Model validation in time-domain

Doubly-Fed Induction Generator based Wind Power Plant Models

Keith Joseph Faria, M.S.E.
The University of Texas at Austin, 2009

Supervisor: Surya Santoso

This thesis describes the generic modeling of a Doubly-Fed Induction Generator (DFIG) based wind turbine. The model can also represent a wind plant with a group of similar wind turbines lumped together. The model is represented as a controlled current source which injects the current needed by the grid to supply the demanded real and reactive power. The DFIG theory is explained in detail as is the rationale for representing it by a regulated current source. The complete model is then developed in the time-domain and phasor-domain by the interconnection of various sub-systems, the functions of which have been described in detail. The performance of the model is then tested for steady-state and dynamic operation. The model developed can be used for bulk power system studies and transient stability analysis of the transmission system. This thesis uses as its basis a report written for NREL[1].

Table of Contents

List of Tables

List of Figures

Chapter 1

Introduction

Wind energy has become the need of the hour to solve the energy crisis faced by the world today. The continual upgrading of wind turbine technology is essential to the future development of wind power. The interconnecting of large-scale wind power plants into the bulk power system has become an important and critical issue and requires steady-state and dynamic transient models of the wind power plant along with its collector system.

The simulation models needed to perform the interconnection studies are usually developed and supplied by the wind turbine manufacturers. Each manufacturer model is based on its own particular wind turbine design and technology and are usually proprietary. Such models can be used directly in power system studies as they are accurate and very detailed. however, non-disclosure agreements restrict the use of these models only to specific wind power projects. This limits model sharing and collaboration among wind project operators. Fortunately, there are efforts underway to resolve this issue.

Although wind turbine designs and technologies vary from one manufacturer to another, there exist common underlying fundamental concepts and principles. Generic models have been developed based on these fundamental principles to emulate the operational behavior and response to wind and grid events. According to mandatory NERC standards (MOD 012, 013 and 014), acceptable dynamic models must be available to reliability entities for power system planning. Acceptable models are ones that are validated, standard library and non-proprietary. The Wind Generator Modeling Group of the Western Electricity Coordinating Council is working with the National Renewable Energy Laboratory and wind turbine manufacturers to develop such generic steady-state and dynamic stability models. This shall help to bridge the gap between the turbine manufacturers and system planners.

There are four major types wind turbine generators topologies called Type 1, 2, 3 and 4 respectively. Type 1 consists of a squirrel-cage induction generator coupled directly to the grid. The Type 2 consists of a wound-rotor induction generator whose rotor winding is connected to an external resistance. This resistance is changed electronically causing variable slip and thus dynamically changing the torque-speed characteristics. Type 3 consists of a doubly fed induction generator (DFIG), which is a wound rotor induction machine with a power electronic converter connected between the rotor terminals and grid. This converter decouples the torque and flux which provides quick separate active and reactive power control. The stator winding is connected directly to the grid. This is also referred to as the partial conversion topology as only part of the generator power flows through the converter. Type 4, called the full conversion topology, has the power converter on the stator and thus has all the power flowing through it. Here too, real and reactive power can be independently controlled over various speeds. A synchronous or induction generator may be used in the Type 4 topology. For each of the above topologies, generic models are being developed.

This thesis documents the modeling of a Type 3 generator (DFIG) utilized for wind power generation. The various components of the wind turbine generator are modeled separately and then combined to make the complete model. These include the generator, the rotor-side converter, the drive-train of the turbine-generator shaft and the aerodynamic representation of the turbine blades. The response of the wind farm is modeled as a single equivalent regulated current source. The rating of this source can be tailored to the power requirement of the model. It can represent outputs of models ranging from a single turbine upto an entire wind farm. The real and reactive power delivered by the generator can be independently controlled by injecting a required set of three-phase currents into the grid using the converter model. The performance of the generic DFIG model is then evaluated and validated with wind power data collected from actual wind power plants having DFIG turbines.

The structure of the thesis is as follows. The concepts explaining the operation and control of DFIG turbines are described in Chapter 2. The dynamic machine model for the generator is discussed here, as is the vector control method for decoupling the real and reactive power control. The strategy of using a single equivalent regulated current source to model the entire wind power plant is also justified. A detailed description of the complete time-domain DFIG wind plant model and the sub-models developed to build it are included. The performance of the developed DFIG wind power plant model is dealt with in Chapter 3. Aspects of performance like the wind power curve, steady-state performance, and quasi-steady-state performance during wind speed changes are examined here. Validation of the simulation results using analytical methods is also introduced. Chapter 4 describes the validation process of the simulation model during dynamic conditions with actual data from real-world wind farms. Additional considerations for the modeling process, such as the inclusion of the collector system in the model, are discussed in this chapter. The model is validated for steady-state and fault conditions. Chapter 5 considers a single-phase phasor-domain model of the DFIG wind plant. The differences between this model and the time-domain model are discussed. Similar performance tests are applied to the model and its behavior is observed during dynamic conditions.

Chapter 2

Modeling of Doubly-Fed Induction Generator Wind Turbines

This chapter is an expansion of the work done for NREL in [1]. It also draws material from [2]. The lead for this part of the project was taken by Mohit Singh.

Section 2.1 describes the concepts underlying the operation of DFIG turbines and their control mechanisms. The dynamic machine model for the generator is discussed in this section, as is the vector control method for decoupling the real and reactive power control. The modeling strategy of using a single equivalent regulated current source to model the entire wind plant is discussed in Section 2.2. The developed DFIG wind plant model and its sub-models are described in detail in Section 2.3.

2.1 Concepts of Doubly-Fed Induction Generators

In electrical engineering, a rotating machine that converts mechanical power to electrical power is defined as a generator. There are mainly 2 kinds of rotating electrical machines, synchronous and asynchronous. Synchronous machines or alternators operate only at the synchronous speed of the electrical system to which they are connected. Asynchronous or induction machines always operate at speeds above or below the synchronous speed of the system. In this thesis only the induction machine is discussed. To act as generators, induction machines have to be operated at speeds greater than their synchronous speeds. Doubly-Fed Induction Generators or DFIGs have the same physical structure as conventional wound-rotor induction machines. The only difference is that there are additional power electronic circuits externally on the rotor windings.

For modeling purposes, the main components of a wind turbine are the turbine rotor (prime mover), a shaft and gear-box unit (drive-train and speed changer), an electric generator and a control system [3]. As wind turbine technology has progressed, turbines have been getting larger in diameter to sweep larger areas and thus achieve higher power ratings. This requires longer rotor blades. The longer the blades, the slower should be the angular speed so that the blade linear tip speed does not exceed the speed of sound and thus physiclly damage the turbine. On the other hand, the electrical generator attached to the turbine requires much higher shaft speeds to operate. Therefore, the turbine blades and hub assembly are connected to the generator shaft through a gearbox which steps up the angular speed and interfaces with the induction generator. Figure 2.1 shows a schematic representation of a typical DFIG wind turbine system.

In DFIG wind turbines, the electrical generator is a wound-rotor induction machine. Slip-rings and brushes are usually used to access the rotor

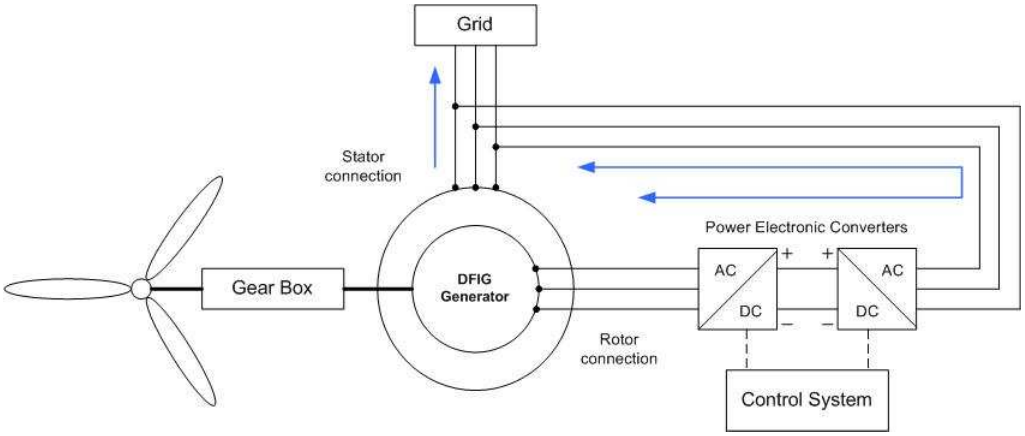

Figure 2.1: Schematic of a Doubly-Fed Induction Generator (DFIG)

circuit, though brushless machines are also available. Unlike a conventional squirrel cage induction machine which is singly-excited, the stator and rotor windings of a DFIG are independently excited. The three-phase stator winding is fed directly from the three-phase supply voltage which is typically below 1 kV at the power system frequency (50/60 Hz). A back-to-back AC-DC-AC power electronic converter is used to rectify the supply voltage and convert it to three-phase AC at the desired frequency for rotor excitation. These circuits help extract and regulate mechanical power from the available wind resource better than would be possible with conventional induction generators. Only a small portion of the real power flows through the rotor circuit. Thus, the rating of the converter need only be about 20% of the rated turbine output [4]. To extract the maximum possible power from the wind, a control system is employed to regulate the rotor frequency (and thus the voltages and currents in the rotor). The control methods employed are vector control or field oriented control and direct torque control (DTC). This thesis concentrates on vector control as it is currently the predominant control method. Vector control allows decoupling of grid-injected direct and quadrature axis currents, i.e. reactive power can be independently controlled without affecting the active power output and vice versa.

Although DFIG wind turbines are generally more complex and expensive than wind turbines employing uncontrolled squirrel-cage induction generators or rotor-resistance controlled wound-rotor machines, they have certain advantages:

- independent real and reactive power control is possible,
- wide generator shaft speed range of up to 20% above and below rated speed for which generation can take place without slip losses,
- maximized power extraction,
- improved fault ride-through performance, and
- reduced mechanical stress.

DFIGs have some advantages over full-converter machines (Type 4) as well. Full-converter machines use an AC-DC-AC convertor for the stator. This causes the converter to be rated for the entire output power of the generator, thus increasing the cost relative to DFIGs. Also, having a convertor on the stator implies that the machine is decoupled from the grid entirely and thus does not provide any additional inertia to the power system. DFIGs, on the other hand, do provide additional inertia and help improve the grid's fault ride-through capability.

The electrical dynamic performance of the DFIG at the fundamental frequency is dominated by the converter [5]. The conventional aspects of generator performance related to internal angle, excitation voltage and synchronism are relevant only in the case of synchronous machines. These are thus not relevant in the case of the DFIG, as it is an induction machine. Since the rotor rotates faster than the rotating magnetic field set up by the stator, the internal angle changes continuously. The excitation voltage fed to the rotor is determined by the control system for the desired values of real and reactive power. The electrical behavior of the generator and converter in the DFIG is largely like that of a current-regulated voltage source inverter, which may be simplified for modeling purposes as being a regulated current source.

The behavior of the wound-rotor induction machine must be understood in order to apply the vector control method to control real and reactive power output of a DFIG. In Subsection 2.1.1, the winding arrangement, equivalent circuit and principle of operation of a wound-rotor machine are described, along with detailed equations. The equations show that in the stationary *abc* reference frame, machine parameters such as inductance are time-varying. To simplify the model, the equivalent circuit in the stationary *abc* reference frame is transformed using the Park transform to the equivalent circuit in the rotating *qd*0 reference frame. This makes the machine parameters such as inductance time-invariant [6]. In the $qd0$ reference frame, the q-axis and d-axis are 90 degrees apart and are hence, decoupled. In Section 2.2, it is shown that q-axis currents can be used to control real power and d-axis currents can be used to control reactive power. This section also validates the simplified representation of the power electronic converter and induction generator as a regulated current source.

2.1.1 Dynamic Modeling Of Induction Machines

The winding arrangement of a conventional 2-pole, 3-phase, wye connected symmetrical induction machine is shown in Figure 2.2 [6]. Here, the winding of each phase is represented by an elementary coil. One side of the coil is represented by a $\otimes$ indicating that the assumed positive direction of current is down the length of the stator (into the paper). The other side of the same coil is represented by a $\odot$ which indicates that the assumed positive direction of current is out of the paper. The axes as, bs and cs represent the positive directions of the magnetic fields produced due to the currents flowing in the stator windings of phase a, b and c respectively. These directions are obtained using the right hand rule on the phase windings. Together they form the stationary abc reference frame. Similarly axes ar, br and cr with respect to the rotor windings are shown. These rotor axes are fixed to the rotor and rotate with it at an angular velocity of ω_r. The angular displacement along the stator circumference is given by ϕ_s. The angular displacement of the rotor with respect to the positive as axis is θ_r.

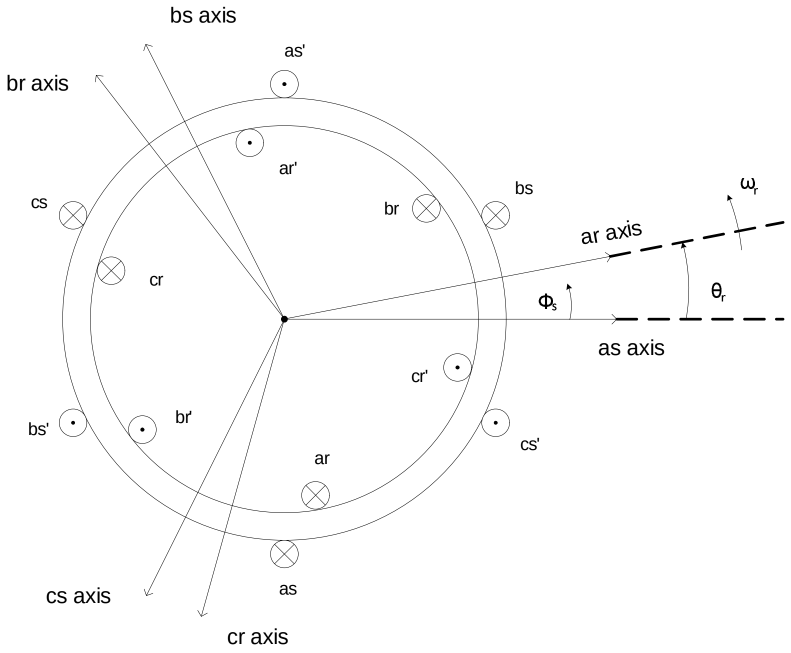

(a) Schematic winding diagram

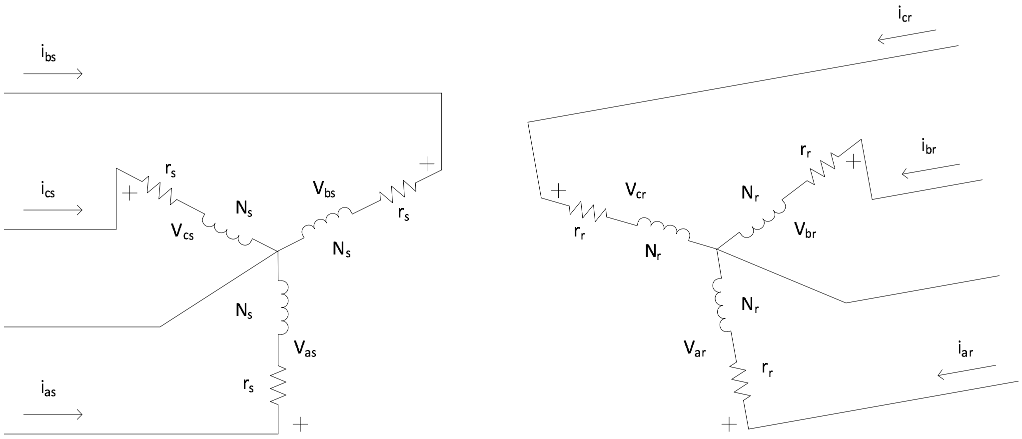

(b) Equivalent circuit

Figure 2.2: Schematic winding diagram and an equivalent circuit of a two-pole, 3-phase, wye-connected symmetrical induction machine

For the machine shown in Figure 2.2, the stator windings are identical and simplified with equivalent turns N_s and resistance r_s. The rotor windings have also been approximated as identical simplified windings with equivalent turns N_r and resistance r_r. Both N_s and N_r are the equivalent number of turns of sinusoidally distributed windings which would give rise to the same fundamental components as their actual respective winding distributions. The windings are thus assumed to be sinusoidally distributed.

The equations for various parameters of the machine shall be derived below. The parameters will be derived with respect to winding as. Similar calculations with displacement shifts of $-\frac{2\pi}{3}$ and $+\frac{2\pi}{3}$ shall give the parameters for windings bs and cs respectively. Exactly the same calculations can be carried out for the rotor windings as well.

The distribution of the as winding may be written as

$$N_{as}(\phi_s) = \begin{cases} \frac{N_s}{2} \cdot \sin\phi_s & 0 \leq \phi_s \leq \pi \\ -\frac{N_s}{2} \cdot \sin\phi_s & \pi \leq \phi_s \leq 2\pi \end{cases} \tag{2.1}$$

where $\frac{N_s}{2}$ is the maximum turn or conductor density expressed in turns per radian.

The magnetomotive force or MMF is defined to be the line integral of the magnetic field intensity H. This along with Ampere's law applied to Eqn. 2.1 gives the MMF of the equivalent as winding as

$$MMF_{as}(\phi_s) = \frac{N_s}{2} \cdot i_{as} \cdot \cos\phi_s \tag{2.2}$$

where i_{as} is the current in the as winding. The air-gap length is uniform with a value g. This along with the definition of MMF for winding as gives

$$MMF_{as}(\phi_s) = g \cdot H_{as}(\phi_s) \tag{2.3}$$

Note that the values of MMF and H depend on the displacement along the stator circumference.

Now, the air-gap flux density due to i_{as} with all other currents zero can be expressed using Eqns. 2.3 and 2.2 as

$$B_r(\phi_s, \theta_r) = \mu_0 \cdot H_{as}(\phi_s) = \mu_0 \cdot \frac{MMF_{as}(\phi_s)}{g} = \frac{N_s}{2} \cdot \frac{\mu_0 \cdot i_{as} \cdot \cos\phi_s}{g} \tag{2.4}$$

where μ_0 is the permeability of free space.

To calculate the self-inductance of winding as, the flux linking it due to its own current i_{as} must be determined. Consider a single turn of the stator winding located at an angle ϕ_s. It spans π radians and has flux linkages determined by performing a surface integral of the air gap flux density over its open surface.

$$\Phi(\phi_s, \theta_r) = \int_{\phi_s}^{\phi_s+\pi} B_r(\sigma, \theta_r) \cdot r \cdot l \; d\sigma \tag{2.5}$$

where,
- l is the axial length of the air gap,
- r is the radius to the mean of the air gap, and
- σ is the dummy variable of integration.

To get the flux linkages for the entire winding, the flux linked by each turn must be integrated over all coil sides carrying current in the same direction. The flux linkages due to stator leakage because of current i_{as} must also be included in the equation. Thus total flux linkages of winding *as* only due to current i_{as} is given by

$$\lambda_{asas} = L_{ls} \cdot i_{as} + \int N_{as}(\phi_s) \cdot \Phi(\phi_s, \theta_r) \; d\phi \tag{2.6}$$

where L_{ls} is the stator leakage inductance mainly due to leakage flux at the end turns.

Equation 2.6 can be solved by substituting in Eqns. 2.1 and 2.5 to give

$$\lambda_{asas} = L_{ls} \cdot i_{as} + \left(\frac{N_s}{2}\right)^2 \cdot \frac{\pi \cdot \mu_0 \cdot r \cdot l}{g} \cdot i_{as} \tag{2.7}$$

The self inductance L_{asas} of winding *as* is now obtained by dividing both sides of Eqn. 2.7 by i_{as} as inductance is equal to flux linkages divided by current. Thus

$$L_{asas} = L_{ls} + \left(\frac{N_s}{2}\right)^2 \cdot \frac{\pi \cdot \mu_0 \cdot r \cdot l}{g} \tag{2.8}$$

The second term on the right-hand side of Eqn. 2.8 is defined to be the stator magnetizing inductance L_{ms}. Thus,

$$L_{ms} = \left(\frac{N_s}{2}\right)^2 \cdot \frac{\pi \cdot \mu_0 \cdot r \cdot l}{g} \tag{2.9}$$

Also, note that by the symmetry of Eqn. 2.8, the self inductances of all the three windings are equal. Therefore,

$$L_{asas} = L_{bsbs} = L_{cscs} = L_{ls} + L_{ms} \tag{2.10}$$

To find the mutual inductance between the *as* and *bs* windings, the flux linking winding *as* due to the current i_{bs} flowing only in winding *bs* must be determined. This is given by

$$\lambda_{asbs} = \int N_{as}(\phi_s) \cdot \Phi(\phi_s, \theta_r)\ d\phi \tag{2.11}$$

Note that the magnetic coupling at the end turns of the windings are neglected. Here the integration over ϕ_s is carried out from π to 2π which causes a negative sign to appear in the simplification. Using Eqns. 2.1 and 2.5 we get

$$\lambda_{asbs} = -\left(\frac{N_s}{2}\right)^2 \cdot \frac{\pi \cdot \mu_0 \cdot r \cdot l}{2 \cdot g} \cdot i_{bs} \tag{2.12}$$

The mutual inductance between windings *as* and *bs* are obtained by dividing Eqn. 2.12 by i_{bs}. Thus,

$$L_{asbs} = -\left(\frac{N_s}{2}\right)^2 \cdot \frac{\pi \cdot \mu_0 \cdot r \cdot l}{2 \cdot g} \tag{2.13}$$

Once again by the symmetry of Eqn. 2.13, we see that the mutual inductances between all the three windings are equal. Substituting Eqn. 2.9 we get

$$L_{asbs} = L_{bscs} = L_{csas} = -\frac{1}{2} L_{ms} \tag{2.14}$$

Parallel calculations are done for the rotor windings. First, the air gap flux density due to the individual rotor currents is found. This is then integrated over a single turn to get the flux linkages of the single turn. These flux linkages are then in turn integrated over all the coil sides carrying current in the same direction to give the total flux linkages. Here too, after dividing by the current it is found that all the self inductances equal and given by

$$L_{arar} = L_{brbr} = L_{crcr} = L_{lr} + L_{mr} \tag{2.15}$$

where L_{lr} is the rotor leakage inductance and L_{mr} is the rotor magnetizing inductance given by

$$L_{mr} = \left(\frac{N_r}{2}\right)^2 \cdot \frac{\pi \cdot \mu_0 \cdot r \cdot l}{g} \tag{2.16}$$

Similarly, all the rotor mutual inductances are equal and are given by

$$L_{arbr} = L_{brcr} = L_{crar} = -\frac{1}{2}L_{mr} \tag{2.17}$$

The mutual inductance between the stator and the rotor windings is a little more tricky. The air gap flux density due to the rotor current is double integrated over the stator displacement to give the mutual flux linkages. This divided by current then gives the mutual inductance between the stator and rotor. The following equalities are obtained

$$L_{asar} = L_{bsbr} = L_{cscr} = \left(\frac{N_s}{2}\right) \cdot \left(\frac{N_r}{2}\right) \cdot \frac{\pi \cdot \mu_0 \cdot r \cdot l}{g} \cdot \cos\theta_r = L_{sr} \cdot \cos\theta_r \tag{2.18}$$

where L_{sr} is defined to be the mutual inductance between the stator and rotor windings given by

$$L_{sr} = \left(\frac{N_s}{2}\right) \cdot \left(\frac{N_r}{2}\right) \cdot \frac{\pi \cdot \mu_0 \cdot r \cdot l}{g} \tag{2.19}$$

Similarly,

$$L_{asbr} = L_{bscr} = L_{csar} = L_{sr} \cdot \cos\left(\theta_r + \frac{2\pi}{3}\right) \tag{2.20}$$

and,

$$L_{ascr} = L_{bsar} = L_{cscr} = L_{sr} \cdot \cos\left(\theta_r - \frac{2\pi}{3}\right) \tag{2.21}$$

Now, the total flux linkages for winding *as* is given by Eqn. 2.22. The total flux linkages for all the other stator and rotor windings are similar.

$$\lambda_{as} = L_{asas} \cdot i_{as} + L_{asbs} \cdot i_{bs} + L_{ascs} \cdot i_{cs} + L_{asar} \cdot i_{ar} + L_{asbr} \cdot i_{br} + L_{ascr} \cdot i_{cr} \quad (2.22)$$

From Figure 2.2(b) the voltage equation for the rotor winding *ar* is given by:

$$V_{ar} = r_r \cdot i_{ar} + \frac{d\lambda_{ar}}{dt} \quad (2.23)$$

The voltage equations for rotor windings *br* and *cr* are similar. The quantities in these rotor equations are then referred to the stator and rewritten (refer to Appendix A).

Thus, in the stationary *abc* reference frame, the relationships between voltages, currents and flux linkages of each phase for this machine can be written using Figure 2.2(b). They are as follows:

Stator Voltage Equations:

$$V_{as} = r_s \cdot i_{as} + \frac{d\lambda_{as}}{dt} \quad (2.24)$$

$$V_{bs} = r_s \cdot i_{bs} + \frac{d\lambda_{bs}}{dt} \quad (2.25)$$

$$V_{cs} = r_s \cdot i_{cs} + \frac{d\lambda_{cs}}{dt} \quad (2.26)$$

Rotor Voltage Equations (referred to the stator side):

$$V_{ar}^{'} = r_r^{'} \cdot i_{ar}^{'} + \frac{d\lambda_{ar}^{'}}{dt} \quad (2.27)$$

$$V_{br}^{'} = r_r^{'} \cdot i_{br}^{'} + \frac{d\lambda_{br}^{'}}{dt} \quad (2.28)$$

$$V_{cr}^{'} = r_r^{'} \cdot i_{cr}^{'} + \frac{d\lambda_{cr}^{'}}{dt} \tag{2.29}$$

where,

-λ stands for the flux linkage,

-Subscripts s and r stand for variables and parameters associated with the stator and rotor respectively, and

-Apostrophe ($'$) stands for variables and parameters referred to the stator side.

Rewriting the stator and rotor voltage equations in a compact matrix form yields:

$$[V_{abcs}] = r_s \cdot [i_{abcs}] + p \cdot [\lambda_{abcs}] \tag{2.30}$$

$$[V'_{abcr}] = r'_r \cdot [i'_{abcr}] + p \cdot [\lambda'_{abcr}] \tag{2.31}$$

where p stands for a time-derivative operator.

The flux linkages in Eqs. 2.30 and 2.31 are expressed as (refer to Appendix A):

$$[\lambda_{abcs}] = [L_{ss}] \cdot [i_{abcs}] + [L'_{sr}] \cdot [i'_{abcr}] \tag{2.32}$$

$$[\lambda'_{abcr}] = [L'_{sr}]^{\mathrm{T}} \cdot [i_{abcs}] + [L'_{rr}] \cdot [i'_{abcr}] \tag{2.33}$$

where, the winding inductance matrices are given by:

$$[L_{ss}] = \begin{bmatrix} L_{ls} + L_{ms} & -\frac{1}{2}L_{ms} & -\frac{1}{2}L_{ms} \\ -\frac{1}{2}L_{ms} & L_{ls} + L_{ms} & -\frac{1}{2}L_{ms} \\ -\frac{1}{2}L_{ms} & -\frac{1}{2}L_{ms} & L_{ls} + L_{ms} \end{bmatrix} \tag{2.34}$$

$$[L'_{rr}] = \begin{bmatrix} L'_{lr} + L_{ms} & -\frac{1}{2}L_{ms} & -\frac{1}{2}L_{ms} \\ -\frac{1}{2}L_{ms} & L'_{lr} + L_{ms} & -\frac{1}{2}L_{ms} \\ -\frac{1}{2}L_{ms} & -\frac{1}{2}L_{ms} & L'_{lr} + L_{ms} \end{bmatrix} \tag{2.35}$$

$$[L'_{sr}] = L_{ms} \cdot \begin{bmatrix} \cos(\theta_r) & \cos(\theta_r + \frac{2\pi}{3}) & \cos(\theta_r - \frac{2\pi}{3}) \\ \cos(\theta_r - \frac{2\pi}{3}) & \cos(\theta_r) & \cos(\theta_r + \frac{2\pi}{3}) \\ \cos(\theta_r + \frac{2\pi}{3}) & \cos(\theta_r - \frac{2\pi}{3}) & \cos(\theta_r) \end{bmatrix} \tag{2.36}$$

In Eqn. 2.35, L'_{lr} is the leakage inductance of the rotor windings referred to the stator. Also, note that Eqn. 2.36 depends on the angular displacement of the rotor θ_r which in turn depends on the angular speed of the rotor ω_r. Thus the inductances in the matrix $[L'_{sr}]$ are all time-variant.

Combining Eqs. 2.30 through 2.33, we get

$$[V_{abcs}] = ([r_s] + p \cdot [L_{ss}]) \cdot [i_{abcs}] + p \cdot [L'_{sr}] \cdot [i'_{abcr}] \tag{2.37}$$

$$[V'_{abcr}] = p \cdot [L'_{sr}]^{\mathrm{T}} \cdot [i_{abcs}] + ([r'_r] + p \cdot [L'_{rr}]) \cdot [i'_{abcr}] \tag{2.38}$$

The voltages, currents and inductances in Eqns. 2.37 and 2.38 are derived in the stationary *abc* reference frame and are thus, time-variant. Modeling and analysis for such a system is unnecessarily cumbersome. These time-variant quantities can be made time-invariant by transforming them into an appropriate rotating reference frame, in this case, the $qd0$ reference frame rotating at an angular speed determined by the synchronous angular speed of the system. By performing the Park transform (refer to Appendix B) on each quantity in Eqns. 2.37 and 2.38, they become,

$$[V_{qd0s}] = r_s \cdot [i_{qd0s}] + \omega_{qd0} \cdot [\lambda_{dqs}] + p \cdot [\lambda_{qd0s}] \tag{2.39}$$

$$[V'_{qd0r}] = r'_r \cdot [i'_{qd0r}] + (\omega_{qd0} - \omega_r) \cdot [\lambda'_{dqr}] + p \cdot [\lambda'_{qd0r}] \tag{2.40}$$

where

- ω_{qd0} is the angular speed in rad/s of the $qd0$ reference frame which is equal to the synchronous speed, and
- ω_r is the angular speed in rad/s of the rotor frame.

Here, the factor $(\omega_{qd0} - \omega_r)$ is the slip-speed of the machine. This factor comes into play due to the fact that the steady-state variables in the asynchronously rotating the rotor frame vary at the frequency corresponding to the slip-speed. Equations 2.39 and 2.40 can be written explicitly as follows.

Stator Voltage Equations:

$$V_{qs} = r_s \cdot i_{qs} + \omega_{qd0} \cdot \lambda_{ds} + p \cdot \lambda_{qs} \tag{2.41}$$

$$V_{ds} = r_s \cdot i_{ds} + \omega_{qd0} \cdot \lambda_{qs} + p \cdot \lambda_{ds} \tag{2.42}$$

$$V_{0s} = r_s \cdot i_{0s} + p \cdot \lambda_{0s} \tag{2.43}$$

Rotor Voltage Equations:

$$V'_{qr} = r'_r \cdot i'_{qr} + (\omega_{qd0} - \omega_r) \cdot \lambda'_{dr} + p \cdot \lambda'_{qr} \tag{2.44}$$

$$V'_{dr} = r'_r \cdot i'_{dr} + (\omega_{qd0} - \omega_r) \cdot \lambda'_{qr} + p \cdot \lambda'_{dr} \tag{2.45}$$

$$V'_{0r} = r'_r \cdot i'_{0r} + p \cdot \lambda'_{0r} \tag{2.46}$$

Likewise, the flux linkages in the rotating $qd0$ frame are given by:

Stator Flux Equations:

$$\lambda_{qs} = (L_{ls} + L_M) \cdot i_{qs} + L_M \cdot i'_{qr} \tag{2.47}$$

$$\lambda_{ds} = (L_{ls} + L_M) \cdot i_{ds} + L_M \cdot i'_{dr} \tag{2.48}$$

$$\lambda_{0s} = L_{ls} \cdot i_{0s} \tag{2.49}$$

Rotor Flux Equations:

$$\lambda'_{qr} = L_M \cdot i_{qs} + (L'_{lr} + L_M) \cdot i'_{qr} \tag{2.50}$$

$$\lambda'_{dr} = L_M \cdot i_{ds} + (L'_{lr} + L_M) \cdot i'_{dr} \tag{2.51}$$

$$\lambda'_{0r} = L'_{lr} \cdot i'_{0r} \tag{2.52}$$

where,

$$L_M = \frac{3}{2} L_{ms} \tag{2.53}$$

Eqs. 2.41 through 2.53 convert the circuit in Figure 2.2(b) to the following equivalent circuits shown in Figure 2.3.

The electromagnetic torque developed in the rotor winding corresponds to the electrical power generated over its synchronous speed. It is expressed as follows [6]:

$$T_{em} = \frac{3}{2} \cdot \frac{P}{2} \cdot (\lambda_{ds} \cdot i_{qs} - \lambda_{qs} \cdot i_{ds}) \ \ \text{[Nm]} \tag{2.54}$$

where P is the number of poles of the machine

This shows that the electromagnetic torque can be expressed in terms of q-axis and d-axis currents and flux linkages.

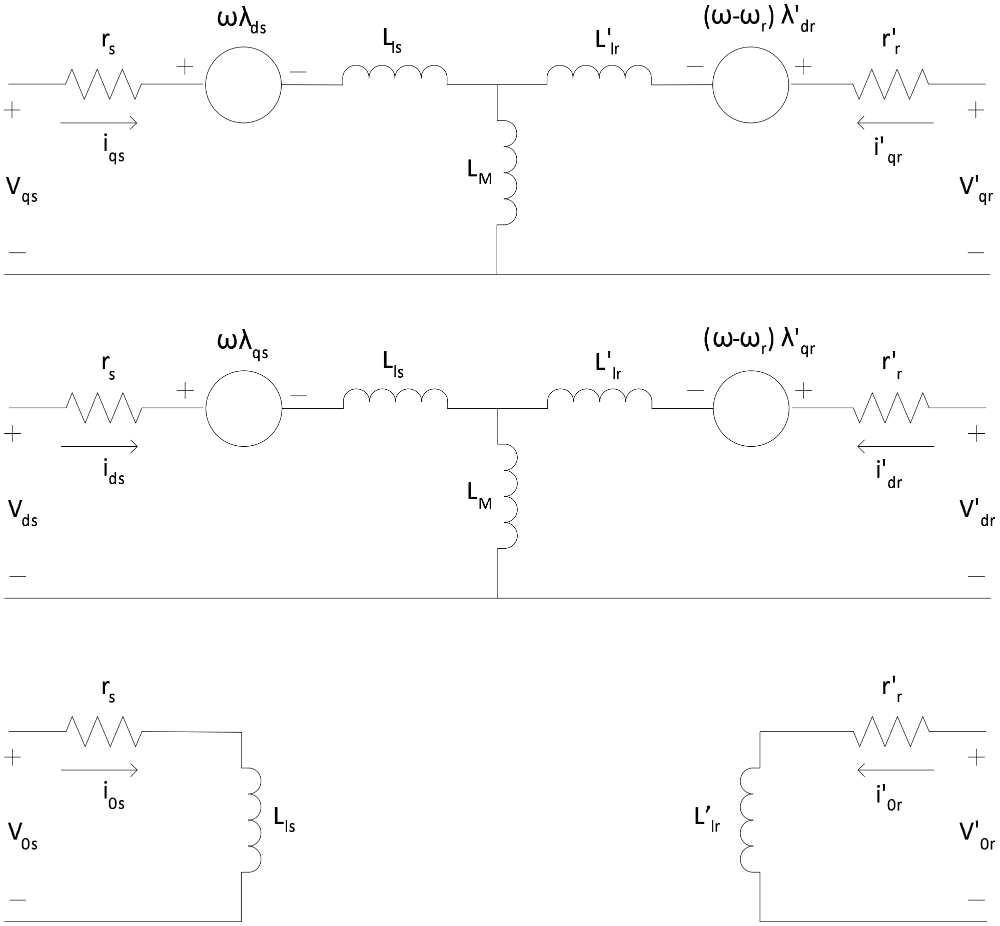

Figure 2.3: Equivalent circuits for a 3-phase, symmetrical induction machine in the *qd*0 reference frame

2.2 Modeling Approach: Regulated Current Source

The primary aim of the model to be designed is that is should be suitably generic. The ultimate purpose of the model is for load flow and dynamic stability studies. Thus, a highly detailed representation of the machine and converter is not necessary. The characteristic property of a DFIG control system is to independently control the real and reactive power. This allows the use of a regulated current source in the dynamic model to represent the induction generator and power electronics. This section presents the analysis behind the approximations of using a regulated current source representation instead of explicitly modeling the generator and power electronics. A simplified model of the device dynamics is adequate. The mechanical modeling of the system has also been considerably simplified, by representing the numerous rotating masses (turbine, gearbox, generator shaft etc.) with a one-mass model.

Let the wound rotor induction machine be represented in a synchronously rotating $qd0$ reference frame as described above in Section 2.1.1. The currents flowing in the stator are assumed to be balanced. These currents produce a resultant stator magnetic field which has a constant magnitude and is rotating at synchronous speed (refer to Appendix B). Since the angular speeds of the stator magnetic field and the $qd0$ rotating frame are identical, the vector of the stator magnetic field is fixed with respect to the q- and d-axes of the $qd0$ rotating frame. Let the d-axis of the reference frame be oriented in such a way that it aligns with the vector of the stator magnetic field. Figure 2.4 illustrates the orientation and alignment of the stationary abc frame, the $qd0$ frame, and the stator magnetic field at a particular instant in time.

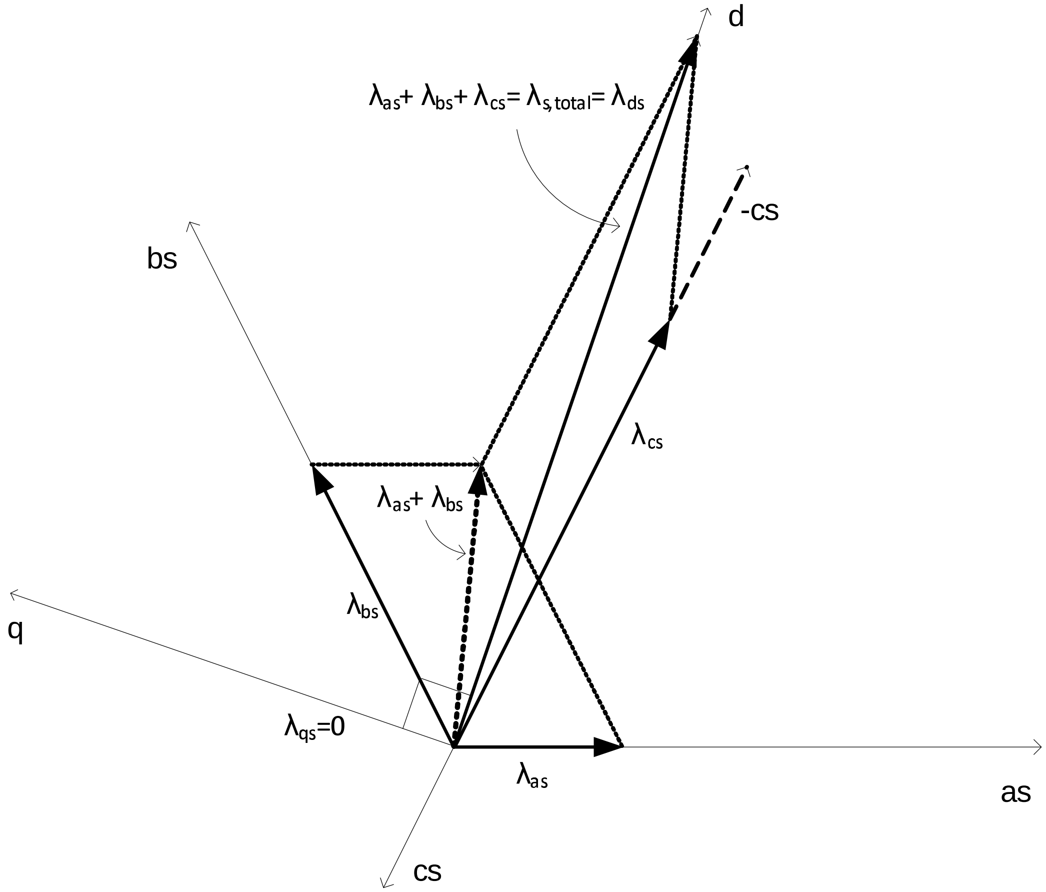

Figure 2.4: The vector sum of the stator fluxes in an induction machine. The *d*-axis of a synchronously rotating *qd*0 frame is aligned with the total stator magnetic field.

Because of the alignment, it is obvious that

$$\lambda_{qs} = 0, \text{ and} \tag{2.55}$$

$$\lambda_{ds} = \lambda_{s,total} \tag{2.56}$$

Substituting Eqs. 2.55 and 2.56 into Eqs. 2.41 and 2.42, and assuming the winding resistive element r_s is negligible, the following relationships are obtained:

$$V_{qs} = \omega_{qd0} \cdot \lambda_{ds} = \omega_{qd0} \cdot \lambda_{s,total} = \text{constant} \tag{2.57}$$

$$V_{ds} = 0 \tag{2.58}$$

Equations 2.57 and 2.58 suggest that the speed voltage (V_{qs}) is time-invariant, and the voltage across the stator d-axis is negligible. Using the stator and rotor flux equations given in Eqs. 2.47 and 2.48, and with $\lambda_{qs} = 0$, the stator q-axis current is

$$i_{qs} = \left(-\frac{L_M}{L_{ls} + L_M}\right) \cdot i'_{qr} \tag{2.59}$$

Similarly, the stator d-axis current is

$$i_{ds} = \left(\frac{\lambda_{ds} - L_M \cdot i'_{dr}}{L_{ls} + L_M}\right) \tag{2.60}$$

Inductance and flux quantities in Eqs. 2.59 and 2.60 are time-invariant, thus the stator q- and d-axis currents can be controlled by adjusting the rotor q- and d-axis currents respectively.

Now, the real and reactive power in the stator windings is given by

$$P_s = \frac{3}{2}(V_{ds} \cdot i_{ds} + V_{qs} \cdot i_{qs}) \tag{2.61}$$

$$Q_s = \frac{3}{2}(V_{ds} \cdot i_{qs} - V_{qs} \cdot i_{ds}) \tag{2.62}$$

Since the stator d-axis voltage is zero as derived in Eqn. 2.58, Eqns. 2.61 and 2.62 can be simplified as shown below,

$$P_s = \frac{3}{2}(V_{qs} \cdot i_{qs}) \tag{2.63}$$

$$Q_s = -\frac{3}{2}(V_{qs} \cdot i_{ds}) \tag{2.64}$$

Therefore, the real and reactive power can be controlled by adjusting the stator q- and d-axis currents respectively. Substituting Eqns. 2.59 and 2.60 here, the stator real and reactive power in terms of rotor currents are as follows:

$$P_s = -\frac{3}{2}\left(\frac{\omega_{qd0} \cdot \lambda_{ds} \cdot L_M}{L_{ls} + L_M}\right) \cdot i'_{qr} \tag{2.65}$$

$$Q_s = -\frac{3}{2}\left(\frac{\omega_{qd0} \cdot \lambda_{ds}}{L_{ls} + L_M}\right) \cdot (\lambda_{ds} - L_M \cdot i'_{dr}) \tag{2.66}$$

It is important to note that in the synchronously rotating reference frame, ω_{qd0}, λ_{ds}, L_M, and L_{ls} quantities are time invariant. Thus, Eqs. 2.65 and 2.66 can be further simplified as follows:

$$P_s = k_{ps} \cdot i'_{qr} \tag{2.67}$$

$$Q_s = -k_{qs1} + k_{qs2} \cdot i'_{dr} \tag{2.68}$$

where k_{ps}, k_{qs2}, and k_{qs2} are the respective constants for the stator real and reactive power. Equations 2.67 and 2.68 clearly show that the stator real and reactive power can be independently controlled by the rotor q- and d-axis currents respectively.

Thus, the desired real power and reactive power output of a DFIG can be realized by the generating the appropriate rotor q- and d-axis currents. Let us call these currents the reference rotor q- and d-axis currents, i.e. $i_{qr}^{\prime(ref)}$ and $i_{dr}^{\prime(ref)}$. These rotor reference currents can be generated by proportional integral controllers based on the difference between the measured and desired

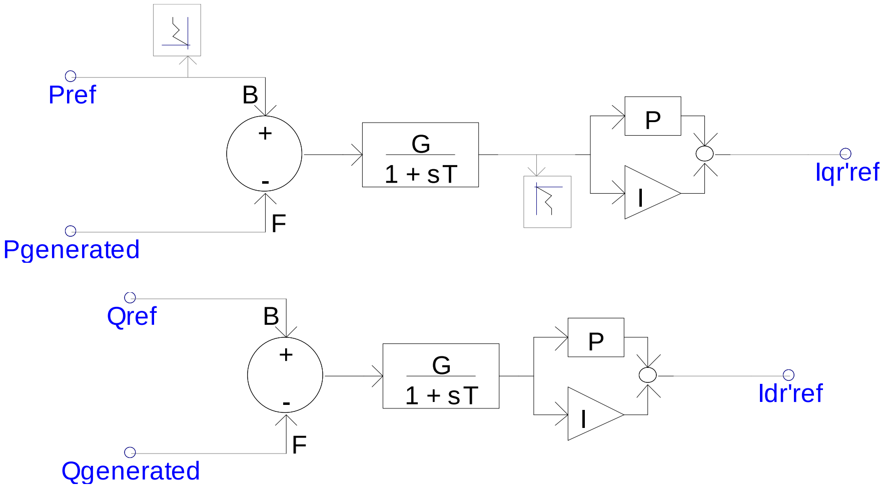

Figure 2.5: Rotor reference currents are generated using proportional integral controllers based on the difference between the measured and desired quantities.

power quantities. Figure 2.5 illustrates how the reference rotor q- and d-axis currents are generated in the model that is to be developed.

Once these reference currents are obtained, they are transformed back to the stationary abc frame. To summarize, the instantaneous abc reference current waveforms are obtained from the rotor's q- and d-axis reference currents through the inverse Park transformation and are fed into the three-phase controlled current source. An alternative two-step inverse transformation can be utilized as well, i.e. first from the synchronously rotating $qd0$ frame to the stationary $\alpha\beta$ frame transformation, and second from the stationary $\alpha\beta$ frame to the stationary abc frame (the inverse Clarke transformation [7]). Figure 2.6 illustrates the two-stage inverse transformation. This method is used in the wind power plant model developed.

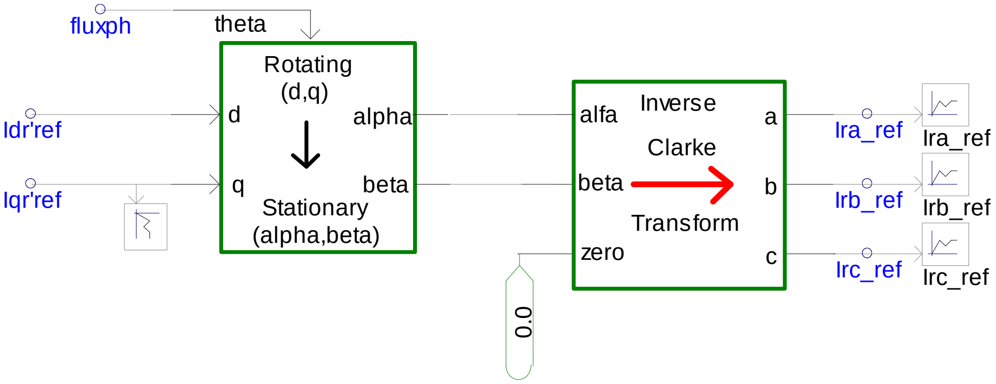

Figure 2.6: Rotor reference currents in the *qd*0 frame are transformed into three-phase currents in the *abc* stationary frame.

These instantaneous reference currents in the *abc* stationary frame are then used as inputs to a controlled current source block in the wind power plant model. The generator and converter have successfully been modeled using a regulated current source.

2.3 DFIG-Based Wind Turbine Dynamic Model

In an actual wind power plant, a local grid called the collector system collects the output from each wind turbine into a single point of interconnection on the grid. As a wind power plant is usually made up of several identical machines, it is a reasonable approximation to parallel all the turbines into a single equivalent large turbine behind a single equivalent impedance. The single equivalent wind turbine has a rated power rating equal to the combined rated power ratings of all wind turbines in the farm. The single equivalent impedance is the combined impedance of the cables of the collector system and all the turbine step-up transformers. The model developed here is consistent with this “paralleling” approach. However, there are a few limitations to the modeling process that are caused by this approach. Electrical disturbances within the collector system and underground cables interconnecting individual wind turbines cannot be analyzed. Also, there is a potentially significant variation in the equivalent impedance for the connection to each wind turbine. The single machine equivalent assumes that all the machines generate the same power output at the same time. This implies the assumption that the geographic dispersion of the farm is small enough that the wind speed profile over it is uniform; which may not be the case in real life.

The model developed is a simplified generic model intended for bulk power system studies where a detailed representation of a wind turbine generator is not required. The model can be used for positive sequence phasor-domain simulations e.g. PSLF or PSS/E. It is intended for transient stability analysis of grid disturbances. The actual device dynamics have been greatly simplified [8]. To be specific, the very fast dynamics involved with the control of the generator-converter have been modeled as algebraic approximations of their response. This makes the generator-converter dynamics instantaneous as compared to a delayed operation in real life. Simplified turbine mechanical controls along with its blade aerodynamic characteristics are included in the model.

This section presents the engineering assumptions, detailed structure and data for each of the component models necessary to represent a DFIG-based wind turbine.

2.3.1 Elements of a Generic DFIG-Based Wind Turbine Model

The generic dynamic model of a Type 3 wind turbine is represented by a combination of blocks based on the functionality of a typical DFIG turbine. These functionalities include the independent control of real (torque) and reactive power, and the control of generator speed and blade pitch angles. The dynamic model developed herein is thus divided into four sub-systems to emulate these functions. They are summarized as follows:

1. **Generator sub-system:** The generator is represented by a regulated current source described in Section 2.2 above. It injects proportional three-phase currents into the power system in response to the control commands from the Converter Control sub-system.
2. **Converter Control sub-system:** This sub-system consists of the Reactive Power Control and Real Power Control sub-systems. These sub-systems emulate power electronics controllers in regulating real and reactive power.
3. **Wind Turbine sub-system:** It is represented by a single-mass model and used to determine the mechanical input power and the angular speed of the wind turbine based on the wind speed and specified pitch angle.
4. **Pitch Control sub-system:** The primary function of the pitch controller is to determine the desired blade pitch angle based on desired

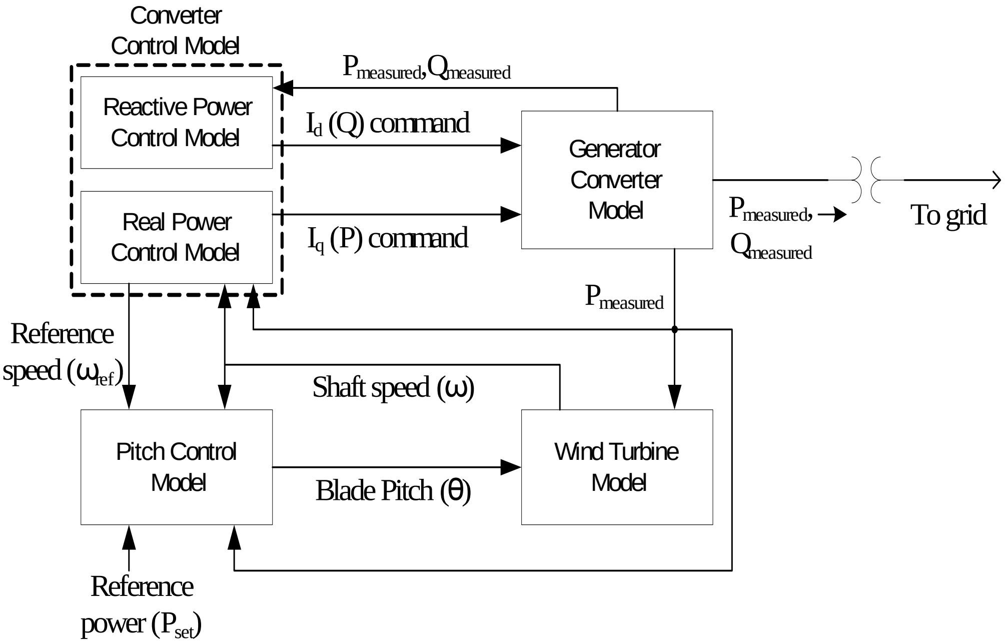

Figure 2.7: Dynamic model structure of a DFIG-based wind turbine

angular speed and real power requirement.

The interaction between the device models is illustrated in Figure 2.7.

2.3.2 Generator Model

The wound rotor induction model is represented with a current regulated source as described in Section 2.2. It emulates the functionality of an actual DFIG wind turbine in controlling real and reactive power independently. The implementation of the current-regulated source is described below.

Consider a three-phase current source illustrated in Figure 2.8. It is

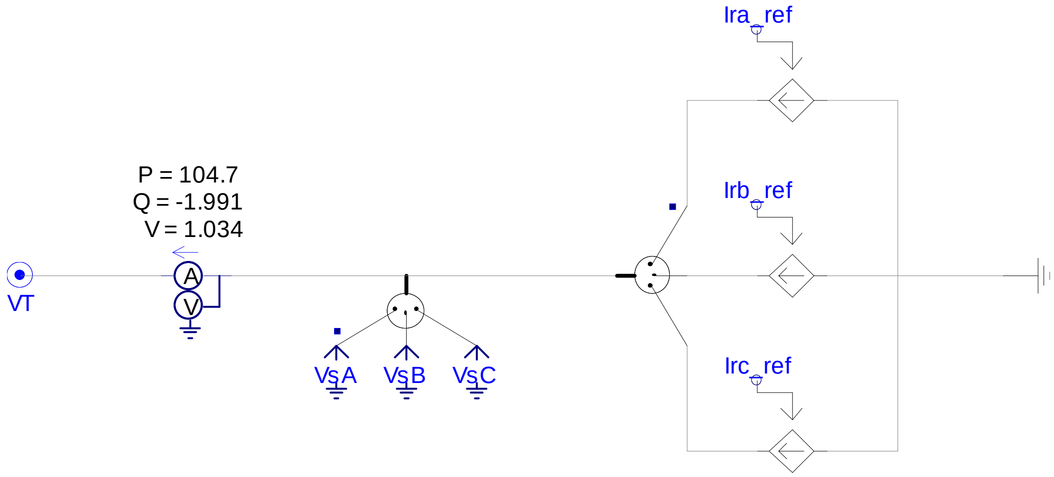

Figure 2.8: Current-regulated source implemented in a time-domain simulation platform.

interconnected to the power system grid at node VT. A multi-meter that measures real power, reactive power and rms voltage during the simulation runtime is shown in the diagram. Additionally, three phase-voltage measurements indicated as VsA, VsB, and VsC are also taken. They represent stator terminal voltages.

To align the d-axis of a synchronous rotating frame of reference to the stator magnetic flux, the instantaneous angular position of the stator magnetic flux must be precisely known. The angular position is determined using the instantaneous three-phase stator voltages (VsA, VsB, and VsC). The process is described below and illustrated in Figure 2.9.

The instantaneous stator voltages VsA, VsB, and VsC (Figure 2.8) are transformed into the stationary $\alpha\beta$ domain using the Clarke transform yielding

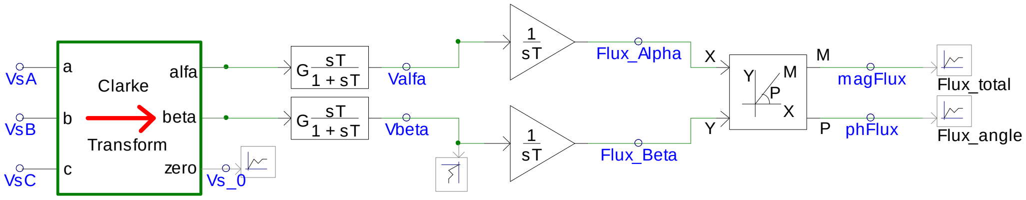

Figure 2.9: The stator flux magnitude and the instantaneous angular position are determined using the Clarke transform.

$Valpha$ and $Vbeta$. These voltages are smoothed with filters to remove any voltage transient that might be present. In the model, the Clarke Transform block is defined by $\frac{2}{3} \cdot [T_{abc2\alpha\beta0}]$ (refer to Appendix B) for scaling purposes.

The DFIG model is connected to a three-phase 34.5 kV system. The system peak voltage is thus 28.18 kV. The instantaneous phase A voltage is plotted in a bold line shown in Figure 2.10. The transformed voltage $Valpha$ is identical to VsA because of scaling. The transformed voltage $Vbeta$ lags $Valpha$ by 90°. These results are as expected.

The magnetic fluxes associated with $Valpha$ and $Vbeta$ are $Flux\_Alpha$ and $Flux\_Beta$ respectively (see Figure 2.9). They are obtained by integrating $Valpha$ and $Vbeta$ to become $Flux\_Alpha$ and $Flux\_Beta$ respectively, since the electromotive force (voltage) is proportional to the time rate of change of the flux. Note that $Flux\_Alpha$ and $Flux\_Beta$ quantities are time varying. The total magnitude and its instantaneous angular position are

$$magFlux = \sqrt{Flux\_Alpha^2 + Flux\_Beta^2} \tag{2.69}$$

$$phFlux = \arctan\left(\frac{Flux\_Alpha}{Flux\_Beta}\right) \tag{2.70}$$

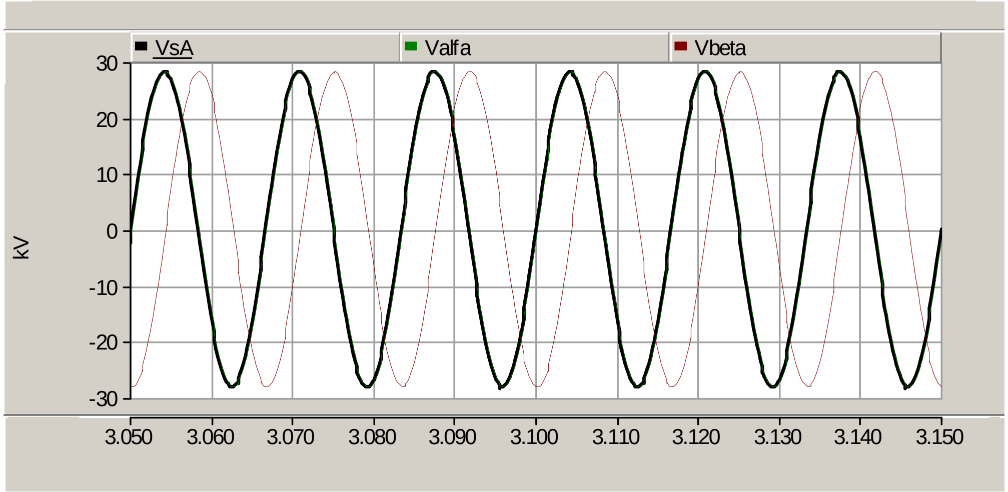

Figure 2.10: Instantaneous phase A voltage waveform and transformed voltage $Valpha$ and $Vbeta$ in the $\alpha\beta$ domain

The magnitude of the stator flux for this particular case is time invariant at 74.7 Wb. The actual magnitude of the flux is for illustration only and not important as it depends on a number of factors such as the stator resistance. The instantaneous flux position varies linearly from $-\pi$ to π as shown in Figure 2.11.

With the position of the stator magnetic field precisely known, the d-axis of a synchronous rotating reference can be oriented properly. A block is used to transform quantities from the stationary $\alpha\beta$ frame to the rotating $qd0$ frame. To check whether this block correctly aligns the d-axis with the total flux, the flux and voltage components in the stationary $\alpha\beta$ frame are transferred to the rotating $qd0$ frame. The instantaneous angular position used in the transformation is given in Eqn. 2.70. If the transformation block

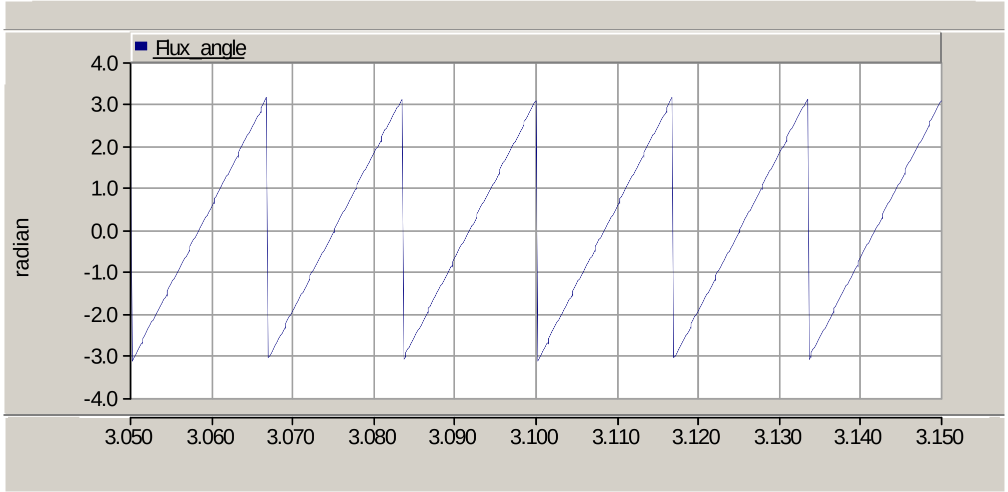

Figure 2.11: Instantaneous position of the stator magnetic flux

performs the alignment correctly, then the stator flux in the q- and d-axes ($Flux\_q$ and $Flux\_d$) should be zero and the time-invariant total magnetic flux should be as obtained in Eqn. 2.69 (in this case 74.7 Wb). Similarly, voltages in the q- and d-axes should be the peak system voltage and zero, respectively. The simulation results confirm these expectations as illustrated in Figures 2.12 and 2.13. Thus, the orientation of the rotating $qd0$ frame is validated.

The three-phase reference currents in the stationary abc frame can now be generated using reference currents in the $qd0$ frame, Iq_cmd and Id_cmd specified by the Converter Control sub-system. A two-stage transformation is used as illustrated in Figure 2.14. Desired currents Iq_cmd and Id_cmd in the synchronous rotating frame are transformed to the stationary $\alpha\beta$ frame and

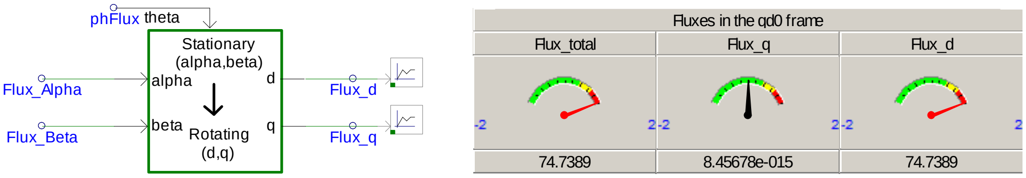

Figure 2.12: Fluxes in the $qd0$ frame. The simulation results confirm the synchronously rotating frame is properly oriented as evidence by the magnitude of the fluxes along the q- and d-axes.

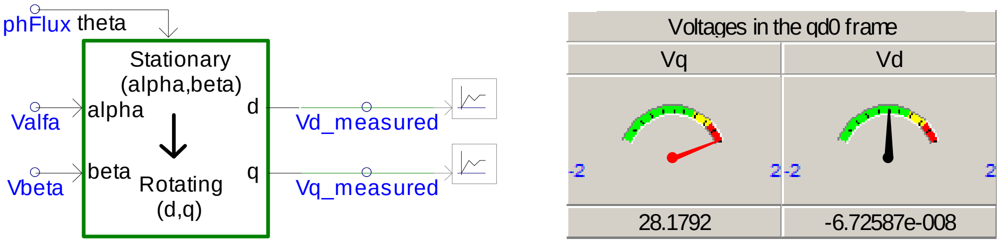

Figure 2.13: Voltages in the $qd0$ frame. The simulation results confirm the synchronously rotating frame is properly oriented as evidence by the voltage magnitudes in the q- and d-axes.

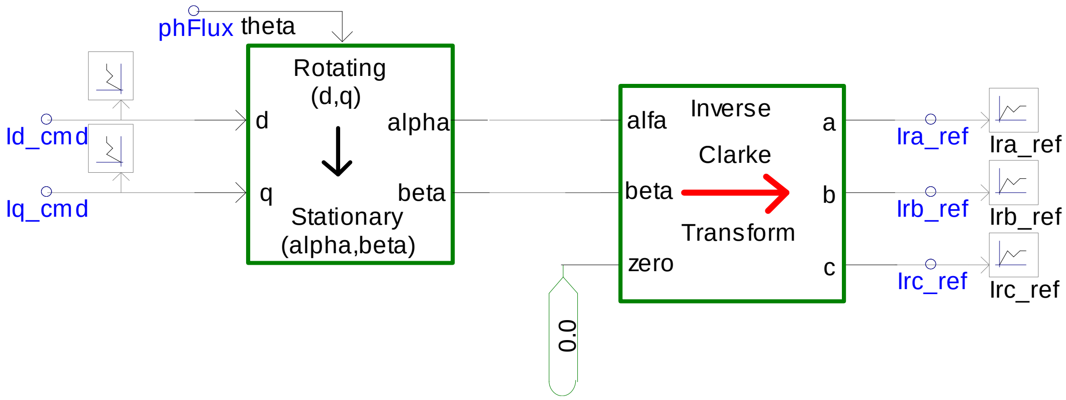

Figure 2.14: Reference currents for the regulated current source are generated using a two-stage transformation.

finally to the stationary *abc* frame to become Ira_ref, Irb_ref, and Irc_ref. These reference currents are injected to the grid through the current source model shown in Figure 2.8.

2.3.3 Converter Control Model

This model controls the active and reactive power to be delivered to the grid. The active and reactive power controls are independent of each other. The parameters and power signals for the active and reactive power control are per-unit of the specified MW capacity of the wind power plant.

Reactive Power Control Model

The reactive power control module generates the desired *d*-axis current Id_cmd for the Generator module. The desired *d*-axis current Id_cmd is obtained using a proportional integral controller shown in Figure 2.15. The

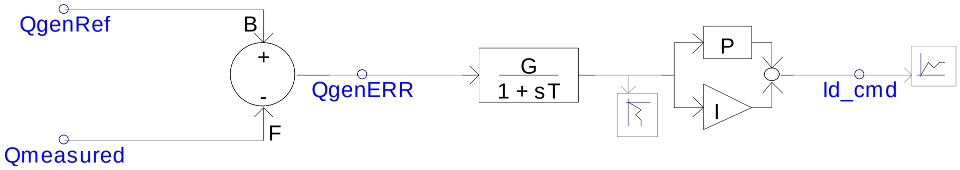

Figure 2.15: The desired d-axis current is generated using a proportional integral controller.

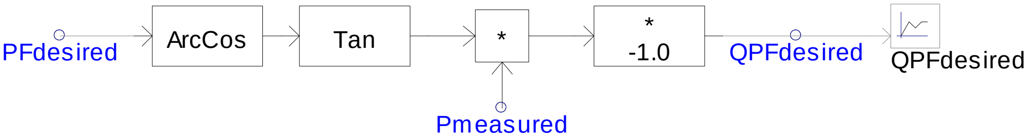

Figure 2.16: The calculation of the desired reactive power to achieve a constant power factor at the generator terminals.

difference between the actual or measured reactive power ($Qmeasured$) and the desired or reference reactive power ($QgenRef$) is used to drive the PI controller.

There are three modes of reactive power control - constant power factor, constant reactive power, and constant terminal voltage. The model described in this thesis implements the first two control modes only. The constant power factor control determines the reactive power ($QPFdesired$) required to achieve the desired constant power factor ($PFdesired$) at the generator terminals. This desired reactive power is given in Eqn. 2.71 and implemented as shown in Figure 2.16. It is then supplied directly as $QgenRef$ in Figure 2.15.

$$Q_{PFdesired} = -P_{measured} \cdot \tan(\arccos(PF_{desired})) \tag{2.71}$$

The constant reactive power mode is straightforward as the desired

Real Power (pu)	0.0	0.08	0.16	0.2	0.4	0.6	0.74	0.87	1
Rotor Speed (pu)	0.688	0.689	0.69	0.78	0.98	1.12	1.198	1.199	1.2

Table 2.1: Real Power vs. Rotor Speed

constant reactive power is supplied directly as $QgenRef$ in Figure 2.15.

Real Power Control Model

This block controls the real or active power delivered to the grid. The non-linear power-speed characteristic [8] shown in Figure 2.17 is used to model the desired generator speed as a function of the power level. The input data used for this function are values of the desired rotor speed at various levels of generated power output, with linear interpolation used between the specified values. All values are in per-unit. In the model, the per-unitized measured real power is fed to this function. The obtained output is then the required angular speed ωRef. The angular ωRef is then compared with the measured ω and converted into the required $Pord$ through a PI controller. This $Pord$ is compared with the measured real power P and fed through a PI controller to give Iq_cmd. The complete system is shown in Figure 2.18.

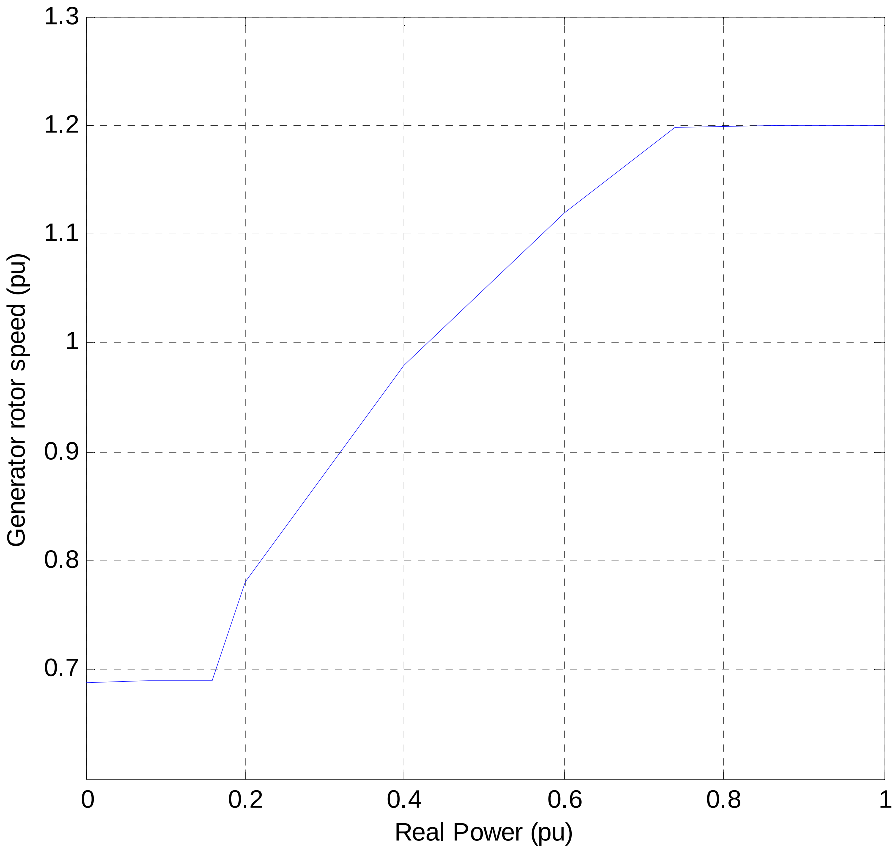

Figure 2.17: Power-Speed characteristic of generator obtained from Table 2.1

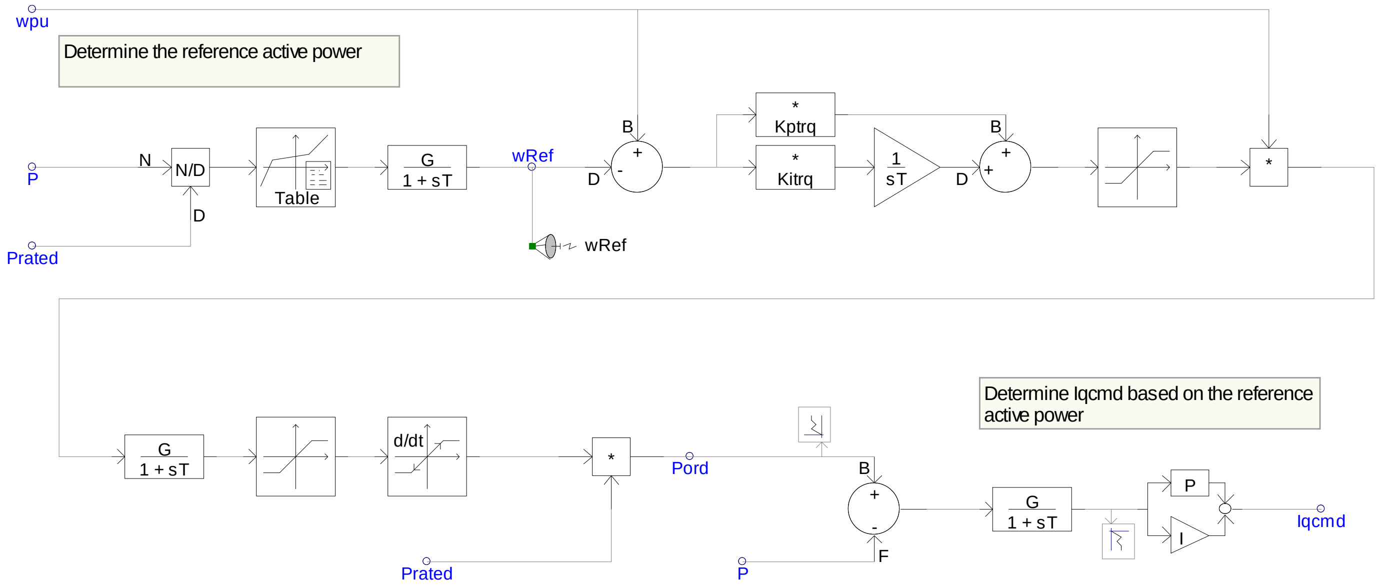

Figure 2.18: Active Power Control Model

2.3.4 Wind Turbine Model

This model calculates the instantaneous shaft speed ω of the wind turbine generator. For this purpose it uses data about the pitch angle, wind speed and real power. Parameters and power signals are per-unit of the rated power capacity specified for the model.

The wind turbine, the induction generator and all moving mechanical parts have been lumped together into a single mass for simplification. The rotor performance of a wind turbine is usually characterized by its power coefficient C_p [9]. C_p is the fraction of the power available in the wind that can be extracted by the rotor. A C_p curve is a graph of C_p versus wind speed for a fixed blade pitch. A wind turbine thus has various C_p curves for various pitch angles which characterize the given turbine. The model includes a simplified aerodynamic model to estimate the C_p curve using the current and initial pitch angles. Equation 2.72 below represents this aerodynamic model.

$$\Delta P = K_{aero} \cdot \theta \cdot (\theta - \theta_0) \tag{2.72}$$

where

- ΔP is the incremental real power
- K_{aero} is the aerodynamic gain factor
- θ is the pitch angle of the turbine blades
- θ_0 is the initial pitch angle

The aerodynamic gain factor K_{aero} has been given a default value of 0.007 determined from the analysis of one set of C_p curves [8]. The initial pitch angle θ_0 is calculated using Eqn. 2.73 below [8]:

$$\theta_0 = \frac{Theta2}{0.75} \cdot \left(1 - \frac{1}{V_{windpu}^2}\right) \tag{2.73}$$

Equation 2.73 assumes that the blade pitch is 0° at the rated wind speed and $Theta2$ degrees at twice rated wind speed. The value of $Theta2$ supplied is 26°. V_{windpu} is the velocity of the wind in per-unit of the rated wind velocity (13 m/s). The maximum power extractable from the incident wind is given by the expression [9]:

$$P_{wind} = \frac{1}{2} \cdot \rho \cdot A \cdot C_p \cdot V_{wind}^3 \tag{2.74}$$

where

- ρ is the density of the air
- A is the area swept by the turbine blades perpendicular to the incident wind
- C_p is the power coefficient of the wind turbine
- V_{wind} is the velocity of the incident wind

Converting Eqn. 2.74 into per-unit using MW capacity and rated wind speed as bases:

$$P_{windpu} = V_{windpu}^3 \tag{2.75}$$

Equation 2.72 represents the amount of power that is to be subtracted from the maximum power extractable from the wind to give the actual mechanical power delivered by the wind turbine to the generator. For wind speeds below rated, the Pitch Control Model (Section 2.3.5) generates a zero pitch angle. This causes ΔP in Eq. 2.72 to become zero. Thus the entire power extractable

from the wind is delivered as mechanical power to the generator. For wind speeds above rated, the Pitch Control Model generates a negative pitch angle and Eq. 2.73 gives a positive value of larger magnitude. These combine to give a net positive value of ΔP to be subtracted from the maximum extractable power from the wind. The positive value is controlled in such a way as to keep the output of the generator at a constant set value (usually the rated MW capacity) for wind speeds higher than rated speed (13 m/s).
Thus the Real Power vs Wind-Speed Curve obtained is as follows:

- **Below rated wind speed :**
  Real Power generated in per-unit is $P_{pu} = V_{windpu}^3$
- **Above rated wind speed :**
  Real Power generated in per-unit is $P_{pu} = 1$

Thus the power generated at wind speeds below rated is proportional to the power available in the wind. This curve is shown below in Figure 2.19.

Equation 2.76 is used to find the instantaneous shaft speed ω [10]. In transient stability studies, this is the fundamental equation that determines rotor dynamics. The speed of the rotating stator magnetic field ω_s, also called the synchronous speed, is set to $2\pi 60 = 377$ rad/s. Note that ω_s is the same as ω_{qdo} from Section 2.1.1.

$$P_{mechpu} - P_{elecpu} = \frac{2H}{\omega_s} \cdot \omega_{pu} \frac{d^2\delta}{dt^2} \tag{2.76}$$

$$\therefore \frac{d\delta}{dt} = \int \frac{(P_{mech} - P_{elecpu}) \cdot \omega_s}{2H \cdot \omega_{pu}} \tag{2.77}$$

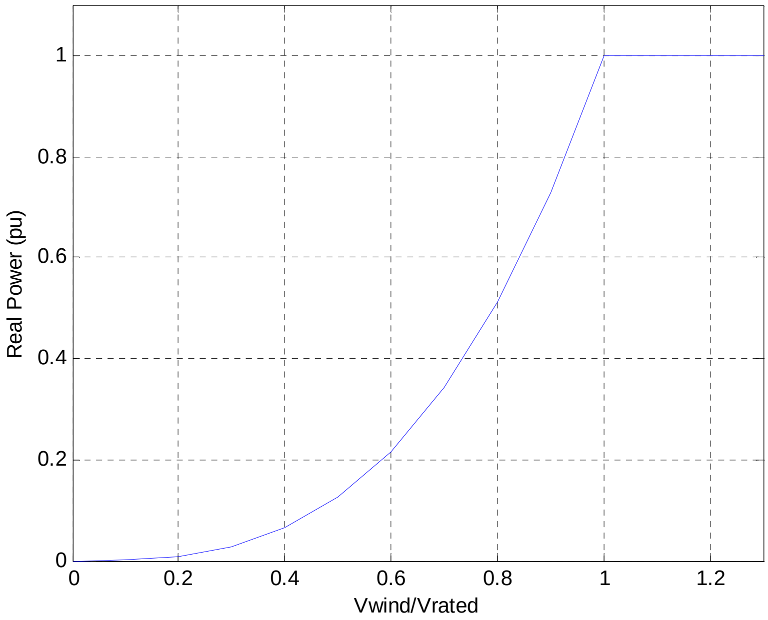

Figure 2.19: Real Power vs Wind Speed Curve

where

- H is the inertia constant or the stored kinetic energy in MJ at synchronous speed over the machine rating in MVA

- δ is the operating power angle

We also use the relation:

$$\omega = \omega_s + \frac{d\delta}{dt} \tag{2.78}$$

The complete single-mass Wind Turbine Model formed by interconnecting the various parts described above is shown in Figure 2.20.

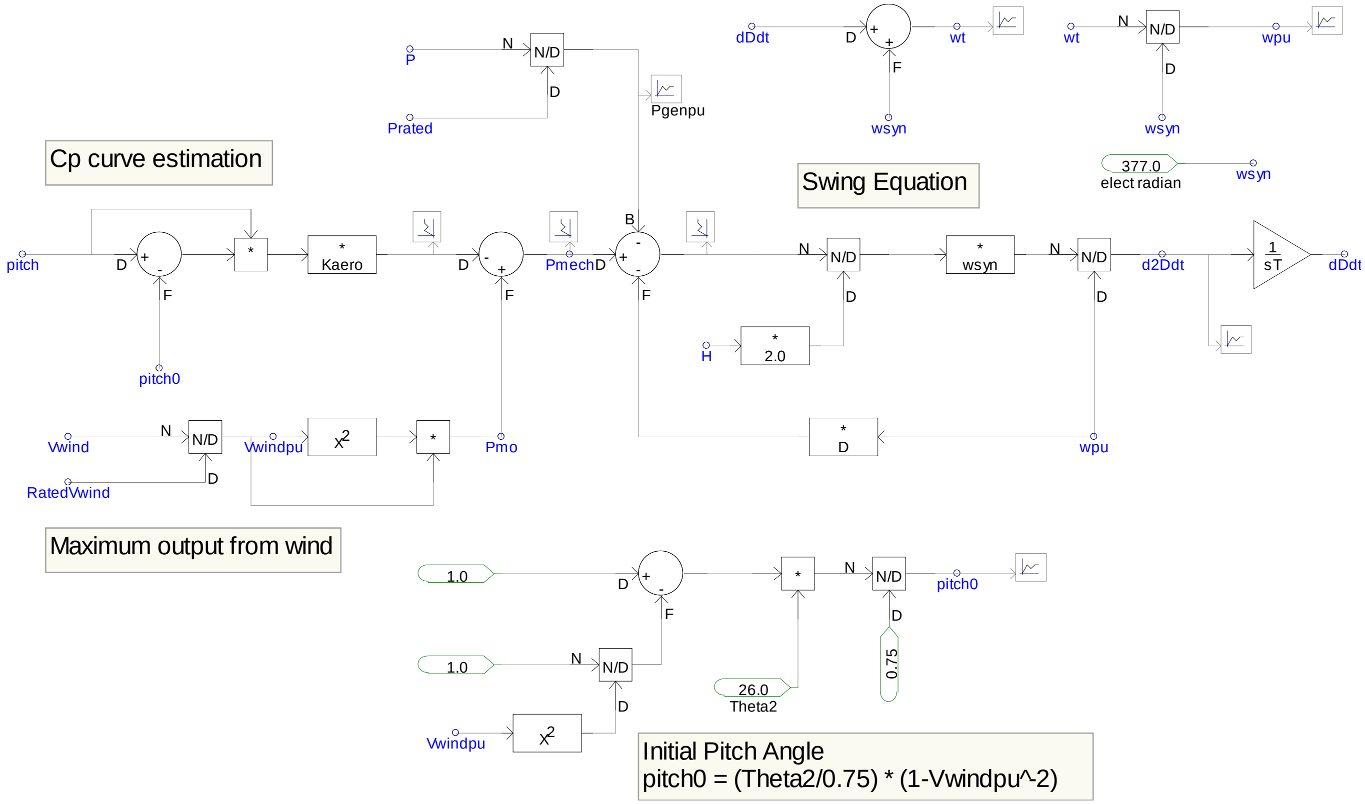

Figure 2.20: Single-Mass Wind Turbine Model

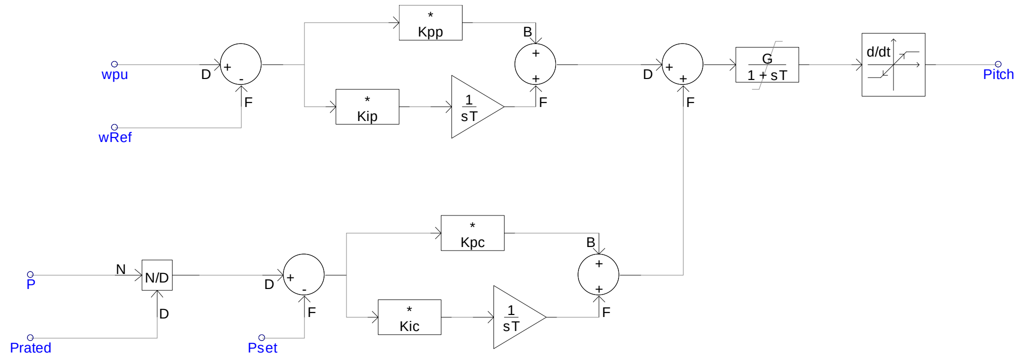

Figure 2.21: Pitch Control Model

2.3.5 Pitch Control Model

This model ensures that for wind speeds lesser than the rated speed, the pitch of the blades is kept at 0°. Above the rated speed it keeps the pitch at a fixed value. The variable $Pset$ fixes the percentage of the rated MW capacity that is required to be generated by the wind farm. It is usually kept fixed at 1 pu. The values of the constants and limits are very important in this block to ensure that the pitch remains zero at lesser wind speeds. The pitch output is very sensitive to changes in these values. The pitch depends therefore on both the instantaneous wind turbine generator speed as well as the real power output of the wind turbine. The Pitch Control model is shown in Figure 2.21.

2.4 Summary

In summary, the underlying principles behind DFIGs have been explained, the modeling approach has been elaborated and the time-domain wind plant model developed using this approach has been described in detail in this chapter. The next two chapters describe the performance of this model and its validation using real-world data.

Chapter 3

Performance of Doubly-Fed Induction Generator Wind Turbines

This chapter is part of the report prepared for NREL [1]. Mohit Singh took the lead for this part of the project.

The development of the DFIG wind power plant model in the time-domain, henceforth to be called the "time-domain model", described in the previous chapter required individual testing of each sub-model. This testing was carried out in detail and each sub-model was observed to operate as expected. The sub-models were then assembled into the complete time-domain model. The performance of this complete time-domain model under steady-state and quasi-steady-state conditions was studied. Quasi-steady-state conditions imply a changing reactive power demand and/or wind speed, but no short-circuit conditions on the system. To perform this testing, the time-domain model was connected to an ideal source (infinite bus) as shown in Figure 3.1.

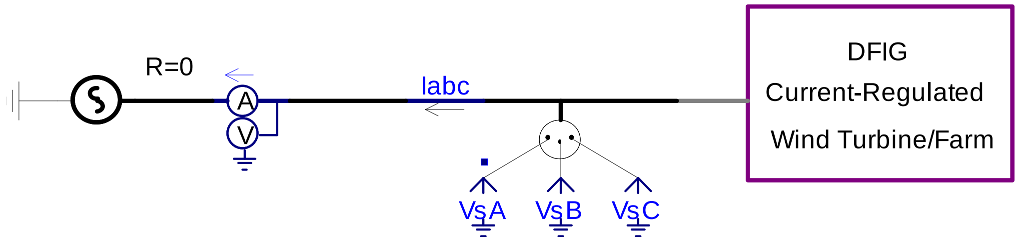

Figure 3.1: Time-domain wind plant model connected to ideal voltage source

3.1 Method of Computing Real and Reactive Power in the $qd0$ Frame and its Validation

For the purpose of calculating the real and reactive power flow out of the time-domain model into the infinite bus, the three-phase voltage and current data available at the model terminals are extracted and processed using a script developed in MATLAB. Here, they are transformed to the $qd0$-domain and then the power equations in the $qd0$ frame of reference described in Section 2.2 are employed. These real and reactive power calculations in the $qd0$-domain are first validated by comparing the results obtained with those from calculations in the steady-state phasor-domain.

For the comparison process we run the time-domain model with parameter values shown in Table 3.1. The current data is then extracted from the model upon simulation and used for the power calculations.

- *Vsource* is the fixed voltage of the ideal three-phase voltage source (infinite bus) connected to the time-domain DFIG wind plant model.
- *Prated* is the rated capacity of the wind plant in MW. This is the real

Vsource (kVrms LL)	***Prated*** (MW)	***QgenRef*** (Mvar)	***Wind Speed*** (m/s)
138	204	20	13 (rated)

Table 3.1: Parameter values for time-domain model to compare real and reactive power calculations between phasor and $qd0$ domains

power that the wind plant is expected to supply to the infinite bus at rated wind speed.

- *QgenRef* is the reactive power demanded from the wind plant i.e. it is the reactive power that the wind plant is expected to supply to the infinite bus.
- *Wind Speed* is the velocity of incident wind. The rated wind speed for the time-domain model is 13 m/s (see Section 3.1.3 for a more detailed discussion on the rated wind speed).

Note that since both real power and reactive power are flowing from the wind plant to the infinite bus, the signs of both will be the same (positive). The phasor-domain calculations and the $qd0$-domain calculations for real and reactive power are discussed in Sections 3.1.1 and 3.1.2 respectively.

3.1.1 Calculations in the Phasor-Domain

Instantaneous three-phase voltage and current waveforms are extracted from the infinite bus connected to the time-domain wind plant model. Per-phase real and reactive power is computed in the phasor-domain. The total three-phase power is the sum of the individual per-phase powers. Figures 3.2, 3.3 and 3.4 show normalized voltage and current waveforms for each phase. The voltage and current waveforms are shown in per-unit of their rated values for easy comparison. The RMS values of voltage and current were determined by finding the peak values of the waveforms and dividing by the square root of two. The voltage in each phase is seen to lead the current implying a positive phase difference.

<u>Phase A Calculations:</u>

Here,

$V_{rms} = 79.67\ kV$

$I_{rms} = 857.52\ A$

$V_{phase} - I_{phase} = +5.59^\circ$

This gives us:

$$Real\ Power = V_{rms} \cdot I_{rms} \cdot \cos(V_{phase} - I_{phase}) = 68\ MW \tag{3.1}$$

$$Reactive\ Power = V_{rms} \cdot I_{rms} \cdot \sin(V_{phase} - I_{phase}) = 6.66\ Mvar \tag{3.2}$$

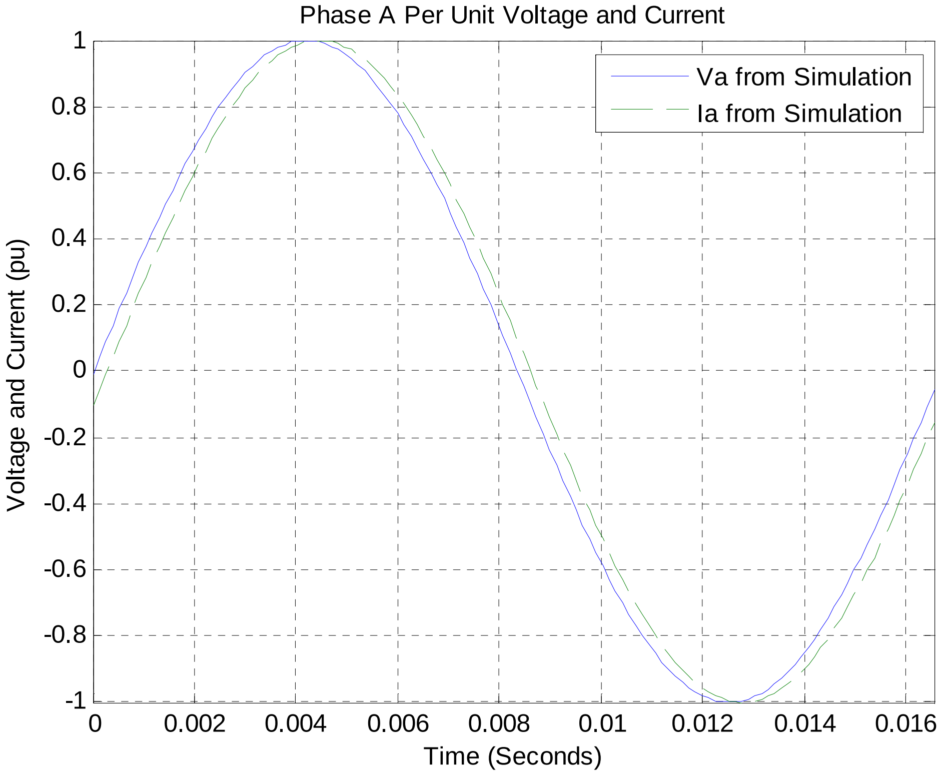

Figure 3.2: Phase *A* per-unit voltage and current

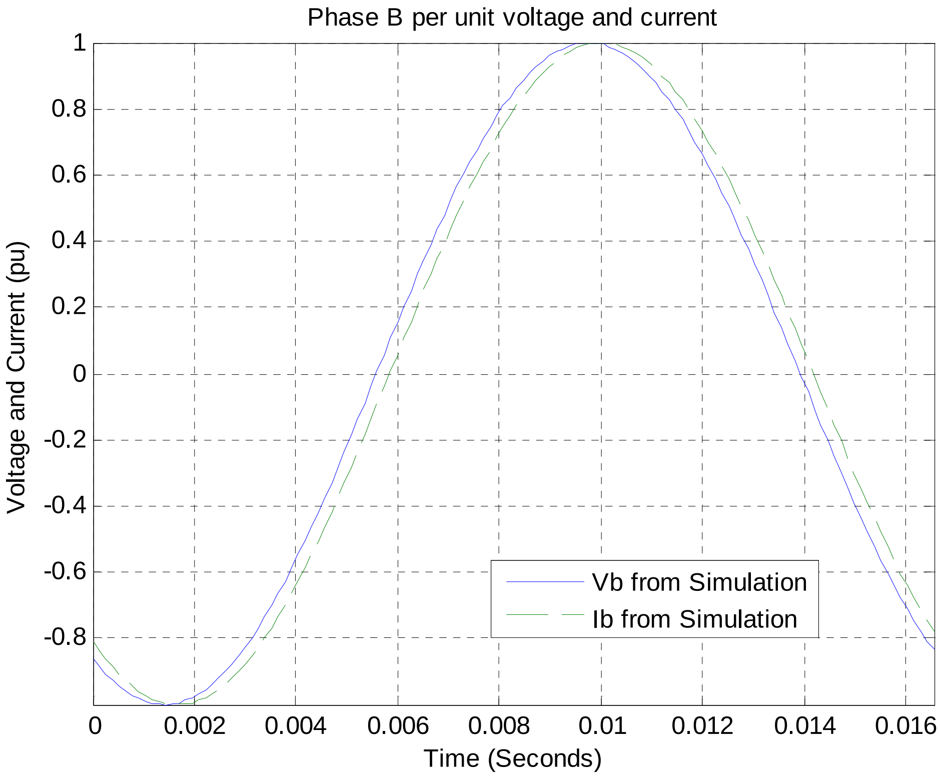

Figure 3.3: Phase B per-unit voltage and current

Phase B Calculations:

Here,

$V_{rms} = 79.67\ kV$

$I_{rms} = 857.51\ A$

$V_{phase} - I_{phase} = +5.585\circ$

$Real\ Power = 67.99\ MW$

$Reactive\ Power = 6.65\ Mvar$

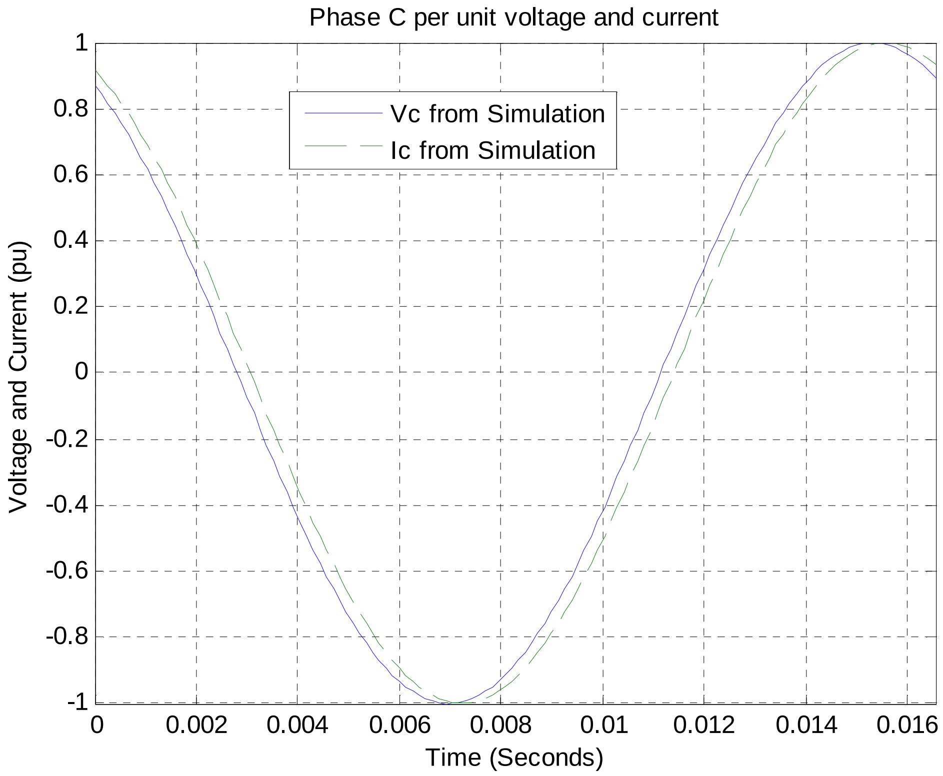

Figure 3.4: Phase C per-unit voltage and current

Phase C Calculations:

Here,

$V_{rms} = 79.65 \ kV$

$I_{rms} = 857.31 \ A$

$V_{phase} - I_{phase} = +5.58 \circ$

$Real \ Power = 67.96 \ MW$

$Reactive \ Power = 6.64 \ Mvar$

Thus, the total three-phase complex power supplied to the grid is given by:

$$\begin{aligned} Total\ Real\ Power &= 68 + 67.99 + 67.96 = \mathbf{203.95\ MW} \\ Total\ Reactive\ Power &= 6.66 + 6.65 + 6.64 = \mathbf{19.95\ Mvar} \end{aligned} \tag{3.3}$$

The real and reactive power outputs from this calculation match the reference (desired) control parameters inputted from Table 3.1. The calculations in the $qd0$ domain are verified in the next subsection and the real and reactive power results are shown to be identical to the results from the phasor-domain calculations.

3.1.2 Calculations in the $qd0$ Reference Frame Domain

The following calculations are carried out in MATLAB. The voltage V_{abcs} and current I_{abcs} extracted from the time-domain model are converted from values in the stationary abc frame to equivalent values in the rotating $qd0$ reference frame. This is done using the Park Transform shown below (refer to Appendix B for more details):

$$[T_{abc2qd0}] = \begin{bmatrix} \cos(\theta_q) & \cos(\theta_q - \frac{2\pi}{3}) & \cos(\theta_q + \frac{2\pi}{3}) \\ \sin(\theta_q) & \sin(\theta_q - \frac{2\pi}{3}) & \sin(\theta_q + \frac{2\pi}{3}) \\ \frac{1}{2} & \frac{1}{2} & \frac{1}{2} \end{bmatrix} \tag{3.4}$$

where θ_q is the angle measured from the positive stationary a-axis to the rotating q-axis.

The transformation equations used are [6]:

$$[V_{qd0s}] = \frac{2}{3} \cdot [T_{abc2qd0}] \cdot [V_{abcs}] \tag{3.5}$$

$$[I_{qd0s}] = \frac{2}{3} \cdot [T_{abc2qd0}] \cdot [I_{abcs}] \tag{3.6}$$

The real and reactive power in the stator are calculated using Eqns. 2.61 and 2.62 in Section 2.2. They are reproduced below.

$$P_s = \frac{3}{2}(V_{ds} \cdot i_{ds} + V_{qs} \cdot i_{qs}) \tag{2.61}$$

$$Q_s = \frac{3}{2}(V_{ds} \cdot i_{qs} - V_{qs} \cdot i_{ds}) \tag{2.62}$$

The results obtained for real and reactive power are:

$$\textit{Total Real Power} = \boldsymbol{204\ MW} \tag{3.7}$$

$$\textit{Total Reactive Power} = \boldsymbol{19.99\ Mvar} \tag{3.8}$$

Thus, the error between the phasor-domain and $qd0$-domain calculation methods is less than 0.2%. This validates the use of the power calculation method using the $qd0$ reference frame.

3.1.3 Wind Power Curve

The rated wind speed of the turbines used in the wind plant is fixed at 13 m/s. This means that when the wind-speed is 13 m/s, the wind plant generates the rated real power (204 MW). The cut-in speed for the turbines is set at 6 m/s. This is the minimum speed required for the wind turbine to start generating power. The wind turbine cut-out speed is 20 m/s. This is the speed above which damage can occur to the turbine and hence when the wind speed is above cut-out, the turbine is shut down by the application of brakes.

Wind Speed Range	**Real Power Generated by Turbine**
Below cut-in speed	Zero output power
Between cut-in and rated speeds	Power generated is maximum extractable from the wind (refer to Section 2.3.4)
Between rated and cut-out speeds	Power generated is the rated output of the wind plant (refer to Section 2.3.4)
Above cut-out speed	Zero output power

Table 3.2: Real power output for various wind speed ranges

In this section we evaluate the wind turbine over the gamut of its wind speed range. The expected power outputs for a DFIG wind plant over different speed ranges is tabulated above in Table 3.2.

The time-domain model is run with the set of parameters shown in Table 3.3. All these parameters are held constant throughout the simulation. The time-domain model is first run with wind speed equal to 6 m/s (cut-in). The generated real power P, generated reactive power Q and the pitch angle are measured and tabulated in Table 3.4. The maximum available power from the wind is also calculated and tabulated for comparison with the generated real power. The wind speed is varied from 6 m/s to 20 m/s (cut-out) in steps of 1m/s and the above process is repeated after each simulation.

For wind speeds greater than or equal to the rated speed, the DFIG should give a constant power output, which is the rated power. This is accomplished by the pitching of the turbine blades when the wind speed goes

Vsource (kVrms LL)	***Prated*** (MW)	***QgenRef*** (Mvar)
138	204	20

Table 3.3: Parameter values for time-domain model to obtain the Wind Power Curve

above rated speed. The maximum pitch has been limited to 30° because for pitch angles above this value the Cp curve of the turbine causes the maximum real power extractable from the wind to be less than the rated value. Also, values of pitch above 30° would be required only for wind speeds above 20 m/s, which is the cut-off speed and is thus of no importance. This may be seen from Table 3.4. The turbine is not run above cut-out speed, although theoretically in can be accomplished in the simulation. In real life, the turbine would be turned out of the wind and brakes would be applied if a similar situation occurred.

From Table 3.4 it is seen that the experimental results from the time-domain model closely match the theoretical results for maximum power extractable from the wind, for wind speeds below rated speed. This shows that the real power controller is functioning optimally. The reactive power is held virtually constant, verifying that a change in the real power output does not cause a change in reactive power output. This hints that the real power and reactive power control are decoupled, but this can only be confirmed if the reactive power controller is shown to have no effect on real power output. The

Wind Speed (m/s)	**Measured *P*** (MW)	**MPEW**[a] (MW)	**Measured *Q*** (Mvar)	***Pitch*** (°)
6	20.38	20.06	19.99	0
7	31.85	31.85	19.99	0
8	47.54	47.54	20.38	0
9	67.69	67.69	19.99	0
10	92.85	92.85	19.98	0
11	123.59	123.59	19.99	0
12	160.45	160.45	19.98	0
13	204	204	19.99	0
14	204	254.79	19.98	8.81
15	204	313.38	19.99	14.07
16	204	380.33	19.98	18.47
17	204	456.19	19.99	22.31
18	204	541.52	19.98	25.76
19	204	636.88	19.99	28.92
20	204	742.83	19.99	31.86

[a] Maximum Power Extractable from Wind = $\textit{rated } P \times \left(\frac{\textit{Wind Speed}}{\textit{Rated Speed}}\right)^3$

Table 3.4: Power generated for various wind speeds

Vsource (kVrms LL)	***Wind Speed*** (m/s)
138	13

Table 3.5: Parameter values for time-domain model to test reactive power control

real power and pitch are plotted versus the wind speed in Figures 3.5 and 3.6 respectively.

3.2 Reactive Power Control and Less-Than-Maximum-Power Output

In this section the effects of changes in reactive power demand on the performance of the time-domain model are observed while keeping the wind speed fixed at the rated value of 13 m/s. The ability of the controller to extract less than maximum extractable power from the wind (governor action) is also examined. The parameters shown in Table 3.5 are held constant throughout the simulation in this section.

To simulate governor action and thus change the amount of maximum real power extractable from the wind, the value of the parameter $Pset$ is changed in the Pitch Control Model (refer to Section 2.3.5). This parameter can be changed only at the beginning of the simulation; hence true governor action cannot be simulated. Changes later on in the simulation are observed to have no effect on the output. For a given constant wind speed, $Pset$ must not

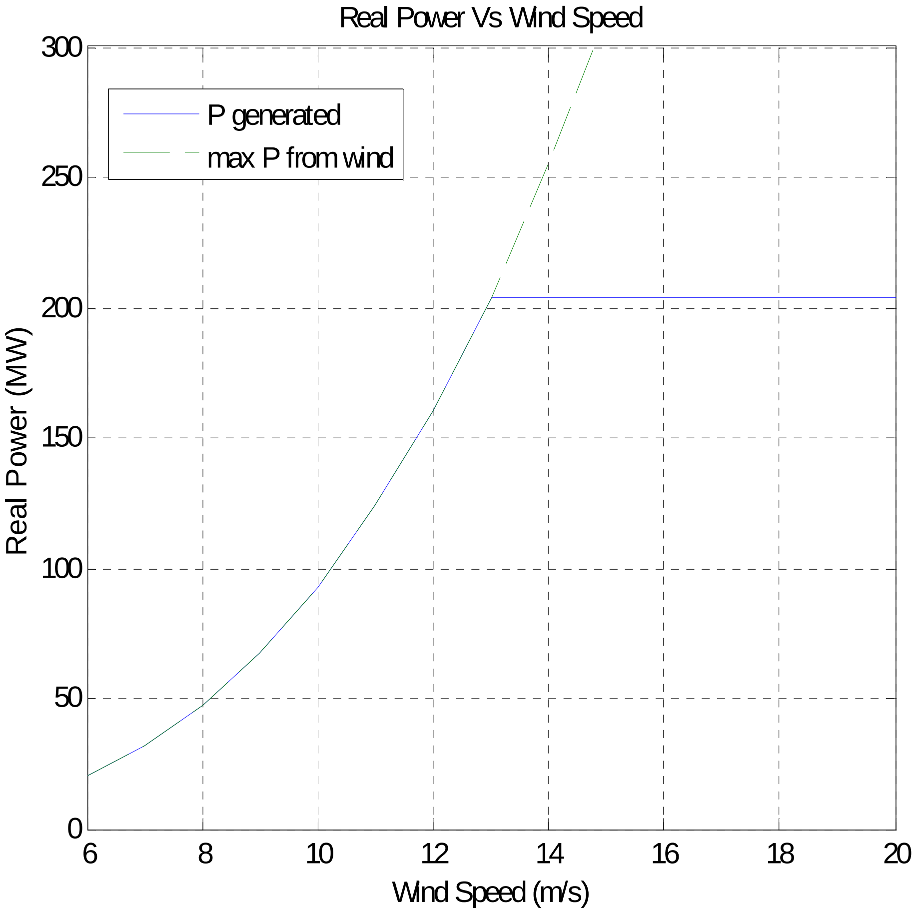

Figure 3.5: Wind Power Curve: Real Power (MW) vs Wind Speed(m/s)

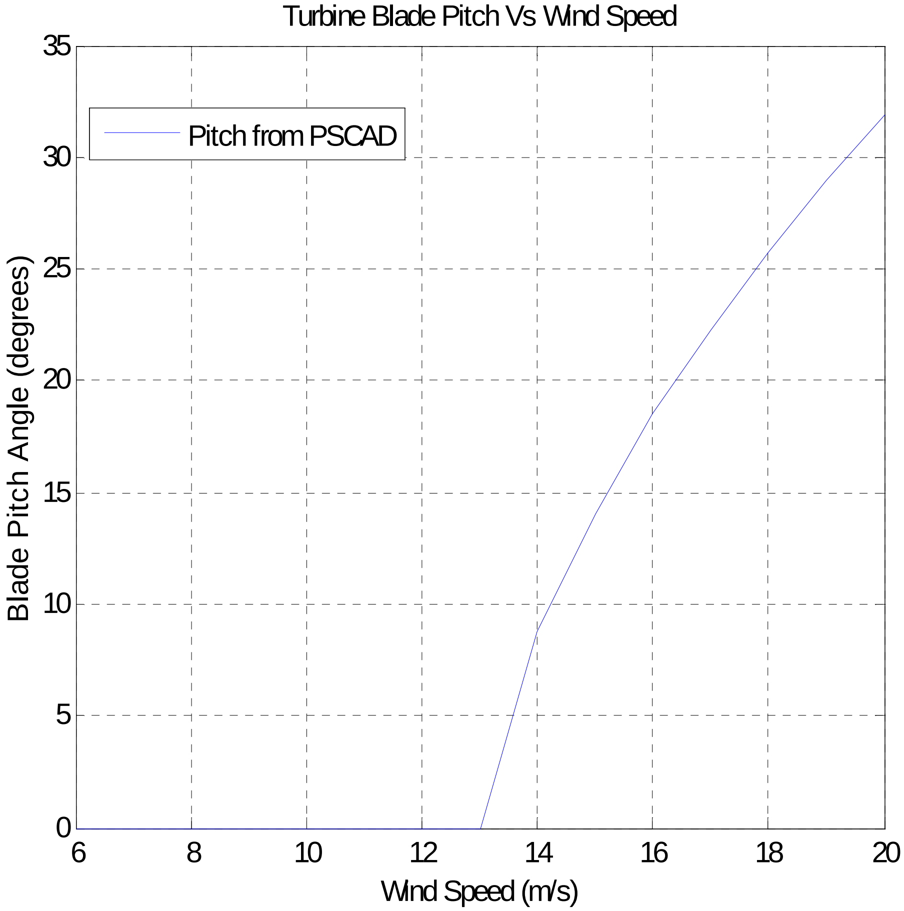

Figure 3.6: Pitch Angle (degrees) vs. Wind Speed (m/s) curve

Case	***Pset*** (pu)	***QgenRef* initial** (Mvar)	***QgenRef* final** (Mvar)
P-1	1 (204 MW)	0	-10
P-2	0.8 (163.2 MW)	0	10

Table 3.6: Changes made to reactive power demand while wind speed is held constant for each of the two cases

be set to such a value so as to try and generate power beyond the maximum power extractable from the wind at that fixed speed.

Two cases, Case P-1 and Case P-2 are simulated. Here "P" stands for Performance Test. Parameter values for both cases are shown in Table 3.6. During simulation, a steady-state is reached at 80 seconds. For each case, the required reactive power is then changed from its initial to final value according to Table 3.6 at time t = 90s.

For the first case, Case P-1, $Pset$ is set equal to 1 pu, corresponding to 100% of extractable power being extracted, which causes the wind plant to generate real power equal to the its rated MW capacity which is 204 MW. With the wind plant operating at this rated power output, the reactive power demand parameter $QgenRef$ is changed in the Reactive Power Control Model (refer to Section 2.3.3). This case is used to determine if the reactive power controller is working correctly and is achieving the output of demanded reactive power. Also, if the reactive power controller's operation is shown to have no effect on the real power output, it shall be confirmed that the real power and reactive power controllers are decoupled. The output for this case is shown in Figure 3.7.

In Figure 3.7, the real and reactive power variation for Case P-1 is shown. The reactive power demand is changed from 0 Mvar to -10 Mvar at time t=90s. The wind speed (and hence the real power extracted) is kept constant. It can be seen that the change in reactive power demand causes the reactive power controller to change the reactive power output to the desired value, and it eventually achieves this value at time t=180s. The active power output remains unchanged during the change in reactive power, suggesting that the real and reactive power controllers are decoupled.

For the second case, Case P-2, $Pset$ is set equal to 0.8 pu, corresponding to 80% of extractable power being extracted. The expected power output of the wind plant is 163.2 MW (80% of 204 MW). The reactive power demand is changed once again during the simulation. This case is used to determine if the change in $Pset$ produces the expected reduced real power, and if the change in reactive power (while $Pset$ is set to less than unity) is different from when $Pset$ is unity. The output for this case is shown in Figure 3.8.

Figure 3.8 shows that the real power output is indeed 80% of the extractable power and therefore implies the correct operation of the governor $Pset$. Again, the change in reactive power from 0 Mvar to 10 Mvar at t = 90s is shown to have no effect on the real power output. The behavior of the real and reactive power controllers thus remains decoupled.

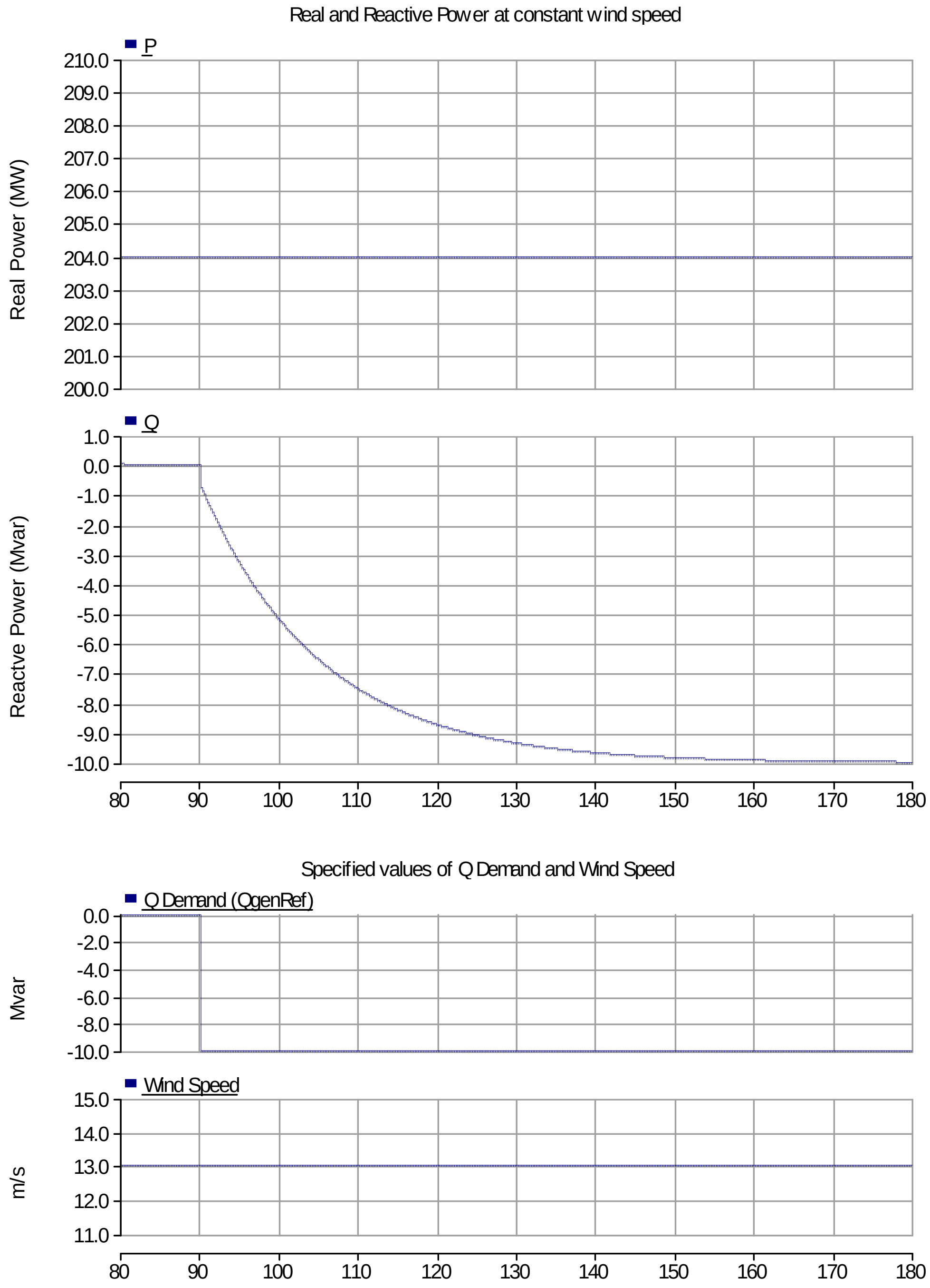

Figure 3.7: Case P-1 ($Pset = 1$): Real and Reactive Power Output

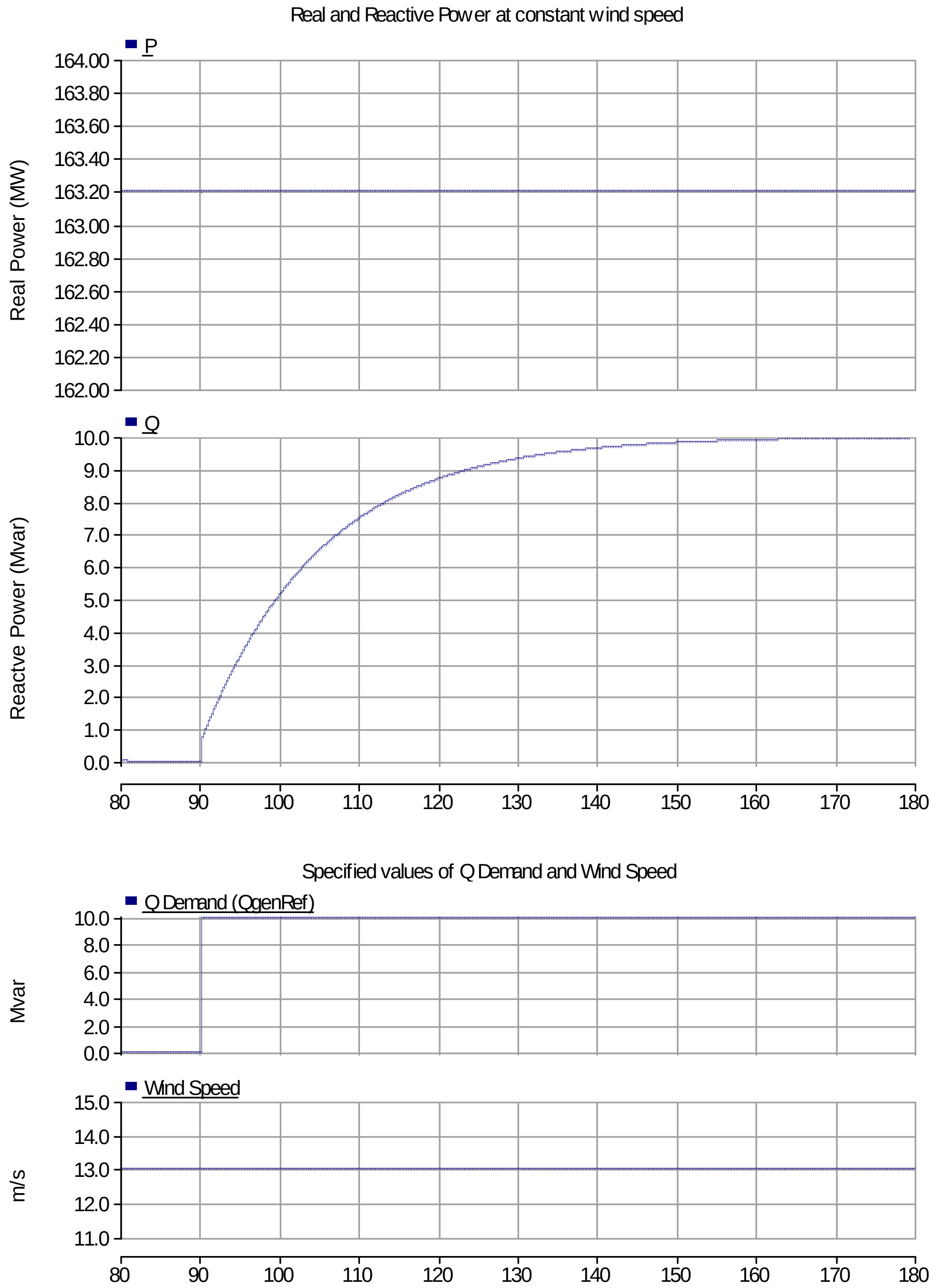

Figure 3.8: Case P-2($Pset = 0.8$: Real and Reactive Power Output

Vsource (kVrms LL)	***Prated*** (MW)	***QgenRef*** (Mvar)	***Wind Speed*** (m/s)
138	204	0	13 (rated)

Table 3.7: Parameter values for time-domain model to test reaction to changes in wind speed

The lower part of each of the figures shows the changes in the control values, while the upper part of each of the figures shows the changes in output real and reactive power. The output figures of both cases show that the simulation result from the time-domain model matches the theoretical result. Change in reactive power had no effect on the real power output in either case and the reactive power controller was observed to be working as expected. Thus the real and reactive power controllers are indeed decoupled.

3.3 Changes in Wind Speed

This section verifies the control action of the real and reactive power modules for variations in the wind speed. The reactive power demand is kept constant, $Pset$ is set to unity and the wind speed is varied. The time-domain model should maintain values as shown in Table 3.4. The initial values are set according to Table 3.7. A steady-state is reached at 80 seconds. After this changes are made shown in wind speed according to Table 3.8 and the generated real power P is measured. If the modules are functioning correctly, then there should be no change in the power outputs.

Case	***Wind Speed*** **initial** (m/s)	***Wind Speed*** **final** (m/s)	**Measured *P*** (MW)
P-3	13	16	204
P-4	13	11	123.59

Table 3.8: Changes made to wind speed while reactive power demand is held constant for each of the two cases

Figure 3.9 depicts Case P-3 wherein the real and reactive power variation during an increase in wind speed above its rated value is shown. In the time-domain model, the wind speed is changed from 13 m/s (rated) to 16 m/s (above rated) at time t=90s. The demanded reactive output power is kept constant. Here too, the lower part of the figure shows the changes in the control values, while the upper part of each of the figures shows the changes in output real and reactive power.It can be seen that the change in wind speed caused the real power controller in the time-domain model to change the real power output to a higher-than-rated value only briefly (a few seconds) before the output is once again lowered to rated real power. This steady output following a transient is as expected, and the behavior of the model is consistent with that of real-world DFIG wind plants.

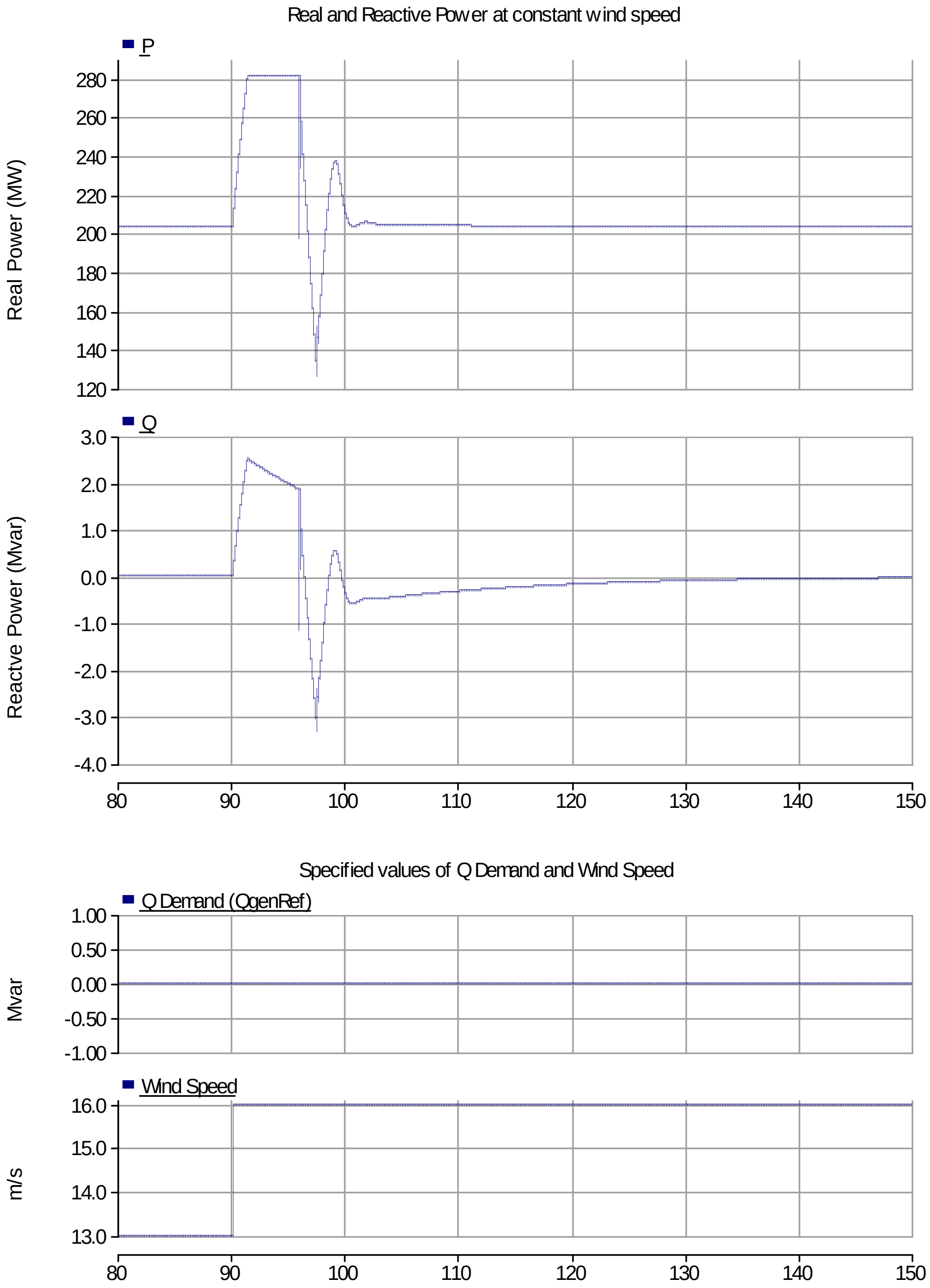

Figure 3.9: Case P-3: Effect of change in wind speed to higher than rated

Figure 3.10 depicts Case P-4 and shows the change in real and reactive power output when the wind speed drops from 13 m/s (rated) to 11 m/s (below rated). The simulation of the time-domain model shows that the real power output changes from rated power to maximum extractable power at 11 m/s ($123.59MW = 204 \times \left(\frac{11}{13}\right)^3 MW$). Reactive power output shows the same behavior as in Figure 3.9. This too is similar to the behavior of real-world DFIG wind plants.

The reactive power output in both cases remains (relatively) unchanged during the change in reactive power, showing a variation that is an order of magnitude smaller than the real power variation. This suggests that the real and reactive power controllers are truly decoupled.

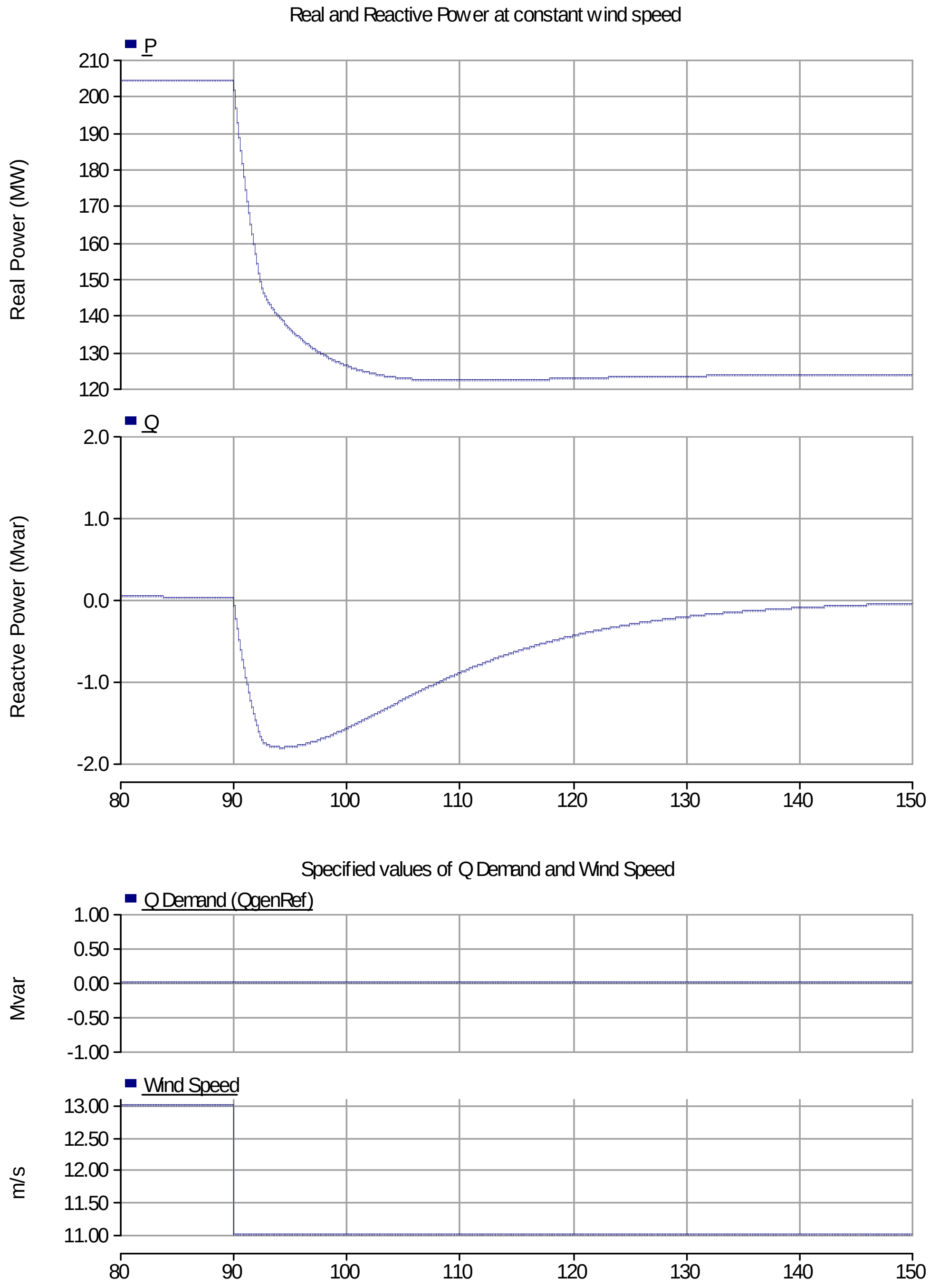

Figure 3.10: Case P-4: Effect of change in wind speed to lower than rated

3.4 Summary

The basic issues about the performance of the time-domain model have been addressed in this chapter. The model was shown to provide a good approximation of real-world DFIG wind plant behavior during steady-state and quasi-steady-state operation. The claim made in Chapter 2 that the real and reactive power could be controlled independently has also been verified. The next step is to study the time-domain model's response during fault conditions. The validation of the model using available fault data from an actual wind plant is described in the next chapter.

Chapter 4

Validation of the Time-Domain DFIG Wind Plant Model

This chapter is also an expansion of the work done for NREL in [1]. It also uses material from [2]. The lead for this part of the project was taken by Mohit Singh.

The purpose of the validation process described in this chapter is to show that the time-domain model truly behaves like a real-world DFIG wind plant, especially during fault conditions. During steady-state and dynamic stability conditions, the validation process proved that the time-domain model results closely matched the real-world results.

4.1 Introduction to the Validation Process

The time-domain DFIG wind plant model was introduced and developed in Chapter 2. In Chapter 3 for the purpose of performance testing it was connected to an infinite bus directly at the wind power plant terminals. Thus, the responses obtained were ideal. To validate the real and reactive power response during a fault event accurately, it is necessary to include a model of the collector system (described in Section 4.2) used by the real world wind farm. The collector system model is connected at the wind plant terminals to form a combined collector and wind plant model. The infinite bus is replaced by a variable voltage source capable of inputting unbalanced voltages into the combined collector and wind plant model.

The time-domain model is tested using four fault cases, Cases V-1, V-2, V-3 and V-4. Here, "V" stands for validation. Cases V-1, V-2 and V-3 pertain to one wind farm. Case V-4 pertains to another wind farm and is dealt with in a separate section at the end of this chapter. For each case, data has been provided from a real-world wind power plant. This includes actual measurements of three-phase voltages and currents at the bus where the collector system is connected to the grid. During simulation, the reactive power demand was set to zero for all cases. However, the real power (dependent on the wind speed) was set to a different constant value for each case. For validation purposes, the three-phase actual voltage data is fed into the time-domain model using the variable voltage source during the simulation. The resulting three-phase currents at the interconnection bus are extracted. This extracted current data is compared with the actual current data and to see if they match closely. A MATLAB script has been developed for the purpose of calculating the real and reactive power flows at the bus, using

- the actual three phase voltage and current data to get one real and reactive power dataset (dataset 1), and
- the three-phase voltage and extracted current from the time-domain sim-

ulation to get another real and reactive power dataset (dataset 2).

The MATLAB script uses the $qd0$-domain calculation method described in Section 3.1.2 to calculate real and reactive power flows through the bus using the voltage and current at the bus. The real and reactive power datasets 1 and 2 are plotted on the same graph and compared by visual inspection. If the match between the two datasets is good, the model is considered to be validated. A flowchart detailing the validation process is shown in Figure 4.1. The time-domain model was successfully validated using this process.

4.2 Collector System

A wind farm consists of wind turbines and a collector system that channels the generated power from the turbines to a collector substation. A transmission line then connects the collector substation to the grid. The point where the collector system connects to the grid is known as the Point of Interconnection or POI. The collector system typically consists of the following passive elements:

- Individual generator transformers (usually pad-mounted units at the base of each turbine) that step up voltage from the below 1 kV level at the generator to medium-voltage levels (34.5 kV is typical)
- Medium-voltage underground cables between the individual turbines
- Medium-voltage overhead lines from the turbine rows to the collector substation

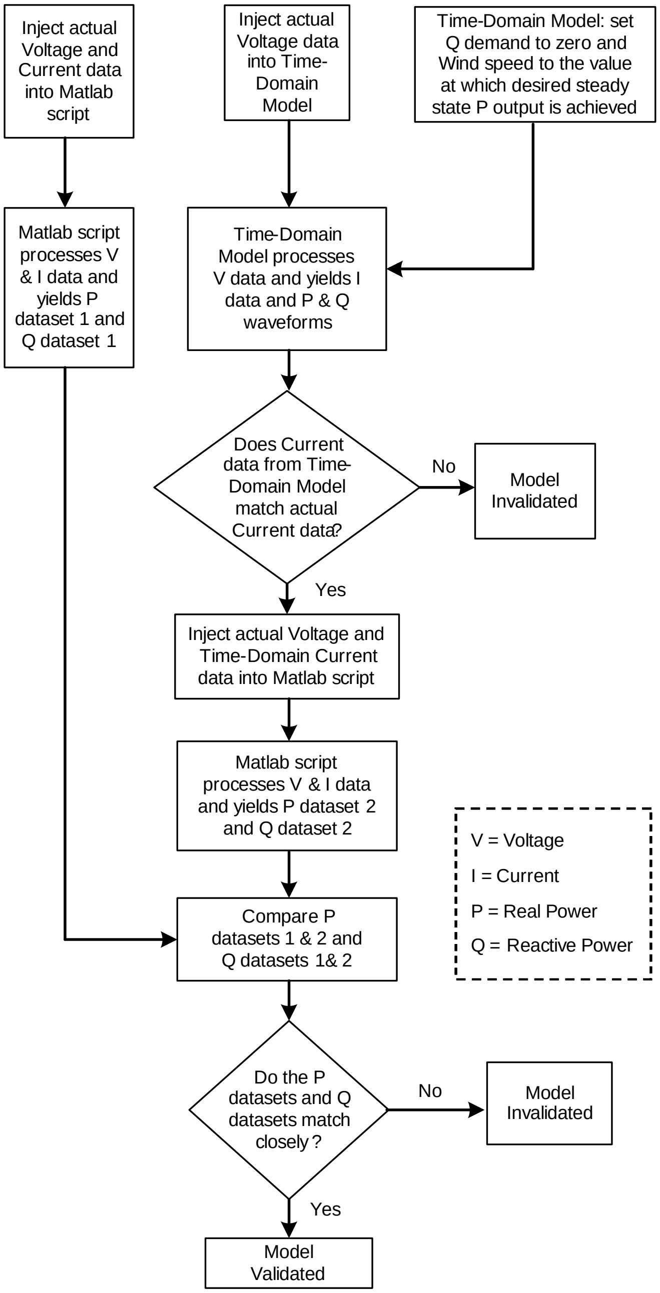

Figure 4.1: Flowchart for Validation Process

- Step-up transformer(s) at the collector substation that raise the voltage to transmission levels

In order to accurately model the behavior of the DFIG wind plant during fault conditions, a collector system model was included in the time-domain model. To create the collector system model, the unit transformers were lumped and modeled as one transformer, and the cables connecting the turbine rows were also lumped and modeled as one impedance element. Since the DFIG wind plant model represents an entire multi-turbine wind farm as a single machine, the approximation of the collector system as lumped elements is justified as it has to be connected to the terminals of this single machine. Reactive power compensation may also be provided at the substation. The collector system model is shown in Figure 4.2.

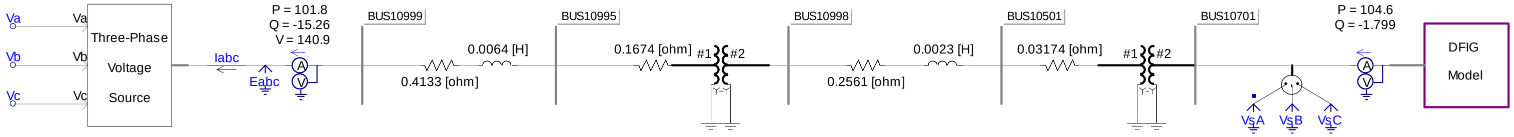

Figure 4.2: Time-domain model: Collector system

4.3 Steady-State Validation: Pre-fault

The correct performance of the time-domain model during steady-state conditions must be verified before it can tested for fault conditions. As mentioned earlier, the actual data provided by the first wind farm contains three-phase voltages and currents at the POI during three different fault conditions. This data also includes about 25 ms of pre-fault voltages and currents which represents their steady-state values. The comparison of this real world pref-fault data with the pre-fault data obtained by simulating the time-domain model can be used to validate the steady-state performance of the model. The MATLAB script mentioned earlier is used to process the pre-fault voltage and current data and get real and reactive power flows. All three cases from the first wind farm were used for the validation. The results from the time-domain model matched the results calculated from the actual data in each case and the model was validated.

The pre-fault validation process is carried out in two stages (phasor and $qd0$ domains) for each case. For the first stage, one cycle of pre-fault voltage and current is extracted from the model at the POI. This is used to calculate the pre-fault real and reactive power in the phasor-domain. Since the system is in steady-state and the voltages are balanced, data from one phase is sufficient to perform the calculations, as the real and reactive power contribution from each phase is identical. This calculation requires the assumption that there are no harmonic distortions in the current and voltage waveforms. While this assumption is true here since the system is in steady-state, a more general and reliable method of calculating magnitude and phase of a signal is to perform a Fast-Fourier Transform (FFT) on it. Results from the FFT method were compared to those from the phasor-domain method and were found to be almost identical. Steady-state real and reactive power was calculated using the RMS values of voltage and current and the phase difference between the two waveforms using calculations similar to those shown in Section 3.1.1. These values multiplied by 3 give the three-phase pre-fault real and reactive power of the system. These values of power in the phasor-domain give an initial estimate of what the powers should be in the time-domain.

The next stage of the validation was to use the MATLAB script to convert the actual data and time-domain model output data to the $qd0$ domain, process the data to find real and reactive power flows, and plot them overlaid on one another. These time-domain results are then compared with the estimate initially calculated from the phasor-domain.

Case V-1

For Case V-1, one cycle of the steady-state voltage and current for phase A is shown in Figure 4.3. The figure shows that the current waveform is leading the voltage waveform by 8.96°. We can employ the same phasor-domain calculations and the same sign convention used in Section 3.1.1 to determine the real and reactive power magnitude and direction of power flow. The sign convention used in Section 3.1.1 is to consider real and reactive power flowing out of the wind plant model to be positive and into the wind plant model be negative. In Figure 4.2, it can be seen that the ammeter direction is such that current into the grid is considered positive.

The calculations for phase A may be performed as follows:

$V_{rms} = 80.74\ kV$

$I_{rms} = 559.38\ kA$

$V_{phase} - I_{phase} = -8.96°$

$Real\ Power = V_{rms} \cdot I_{rms} \cdot \cos(V_{phase} - I_{phase}) = 44.61\ MW$

$Reactive\ Power = V_{rms} \cdot I_{rms} \cdot \sin(V_{phase} - I_{phase}) = -7.03\ Mvar$

Since the voltages and currents are balanced in steady-state, we can assume that the contribution to real and reactive power from phases B and C is the same as that from phase A. The three-phase real and reactive power output for Case V-1 can be calculated as:

$$Three\text{-}Phase\ Real\ Power = 3 \times 44.61\ MW = 133.84\ MW$$

$$Three\text{-}Phase\ Reactive\ Power = 3 \times -7.03\ Mvar = -21.10\ Mvar$$

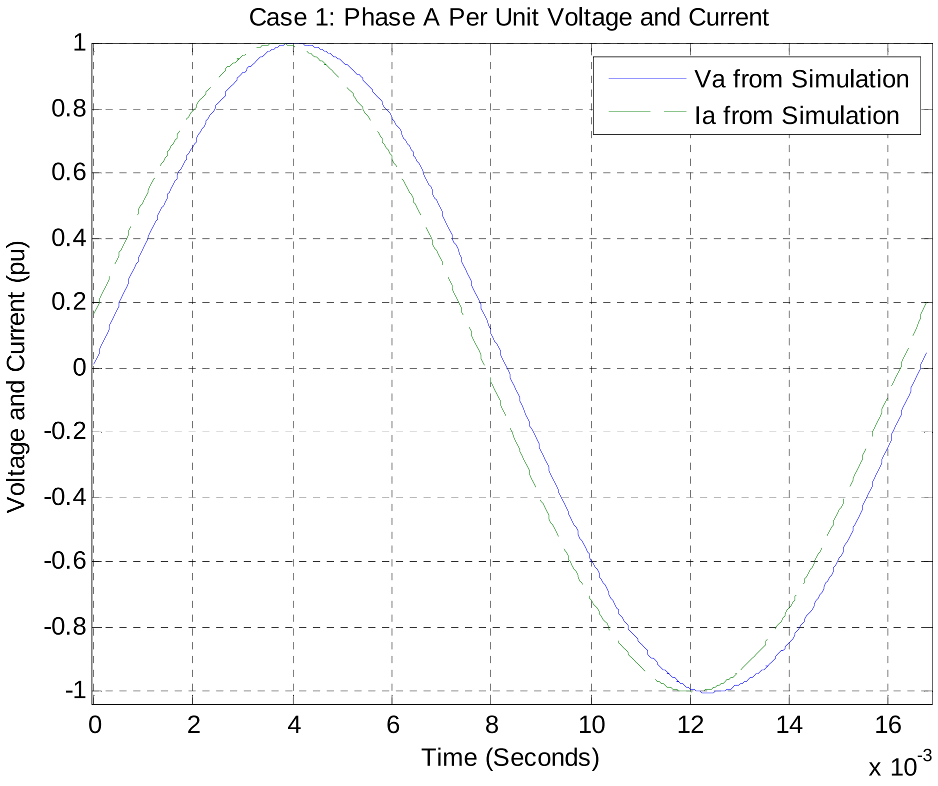

Figure 4.3: Case V-1: One cycle of pre-fault voltage and current data for phase A

The results in Figure 4.4 show that the results from the actual data and the time-domain model match each other closely, as well as matching the estimate from the phasor-domain. The steady-state operation of the time-domain is thus validated for Case V-1.

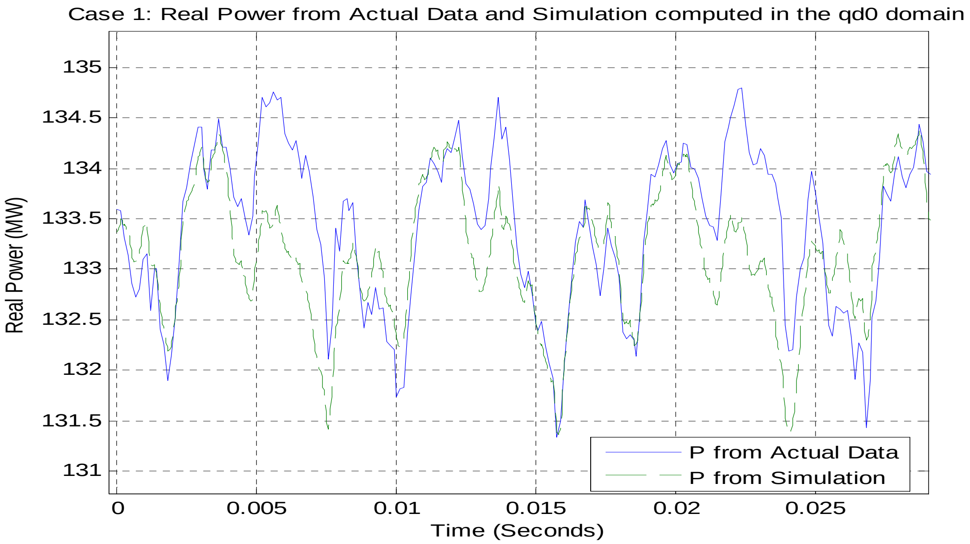

(a) Case V-1: Real Power Comparison: Actual vs. Time-Domain Model

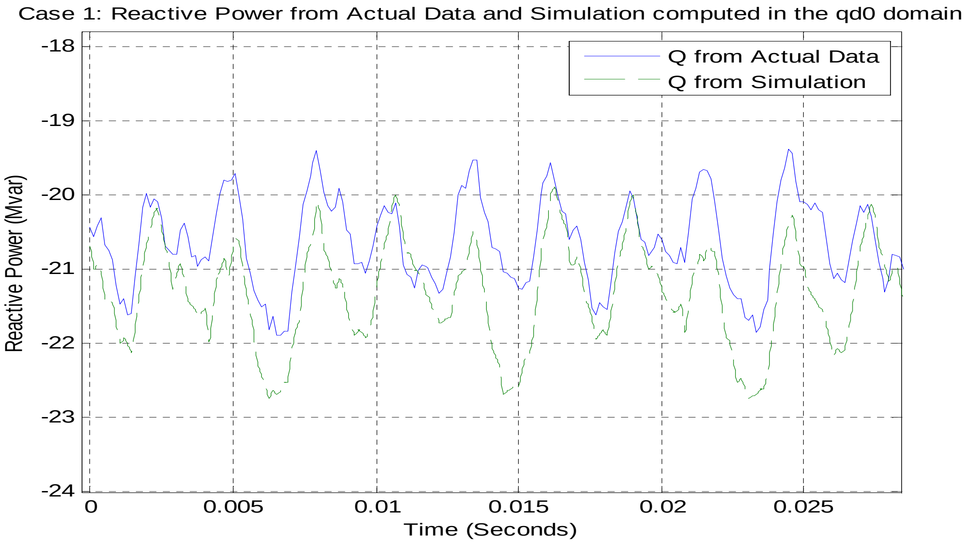

(b) Case V-1: Reactive Power Comparison: Actual vs. Time-Domain Model

Figure 4.4: Case V-1: Pre-fault Real and Reactive Power Comparison: Actual vs. Time-Domain Model

Case V-2

An analysis similar to that for Case V-1 is carried out for Case V-2. One cycle of steady-state voltage and current data for phase A is shown in Figure 4.5. The calculations are as follows:

$V_{rms} = 81.85\ kV$

$I_{rms} = 477.20\ A$

$V_{phase} - I_{phase} = -6.59°$

$Real\ Power = V_{rms} \cdot I_{rms} \cdot \cos(V_{phase} - I_{phase}) = 38.8\ MW$

$Reactive\ Power = V_{rms} \cdot I_{rms} \cdot \sin(V_{phase} - I_{phase}) = -4.48\ Mvar$

The three-phase real and reactive power output for Case V-2 can once again be calculated as:

$$Three\text{-}Phase\ Real\ Power = 3 \times 38.8\ MW = 116.4\ MW$$

$$Three\text{-}Phase\ Reactive\ Power = 3 \times -4.48\ Mvar = -13.45\ Mvar$$

The results in Figure 4.6 show that the results from the actual data and the time-domain model match each other closely, as well as matching the estimate from the phasor-domain. The steady-state operation of the time-domain is thus also validated for Case V-2.

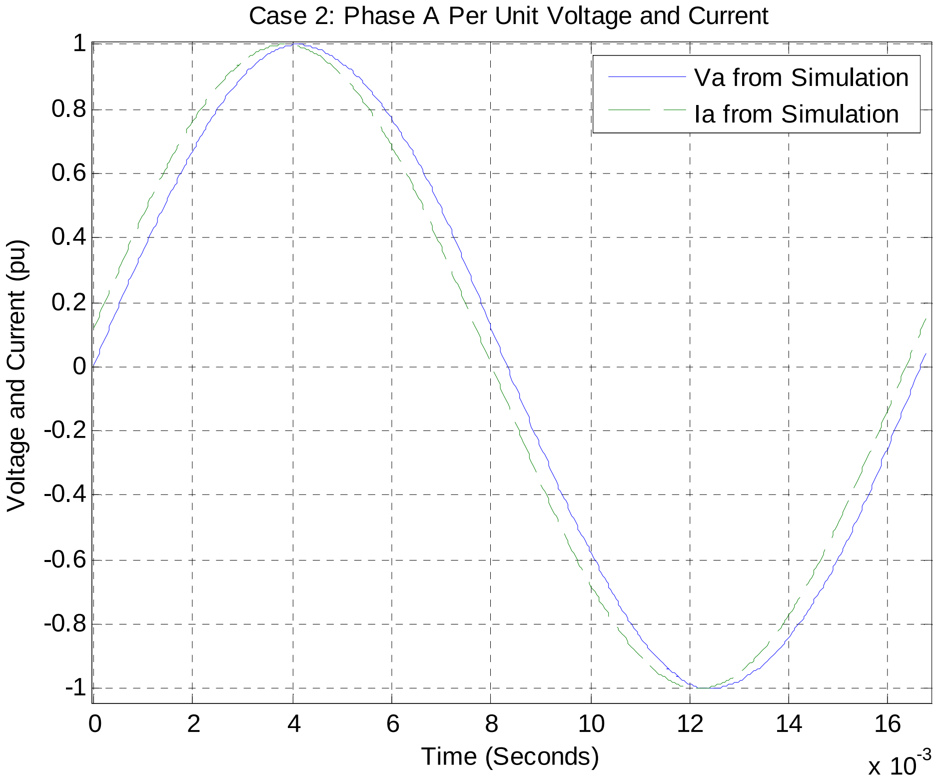

Figure 4.5: Case V-2: One cycle of pre-fault voltage and current data for phase A

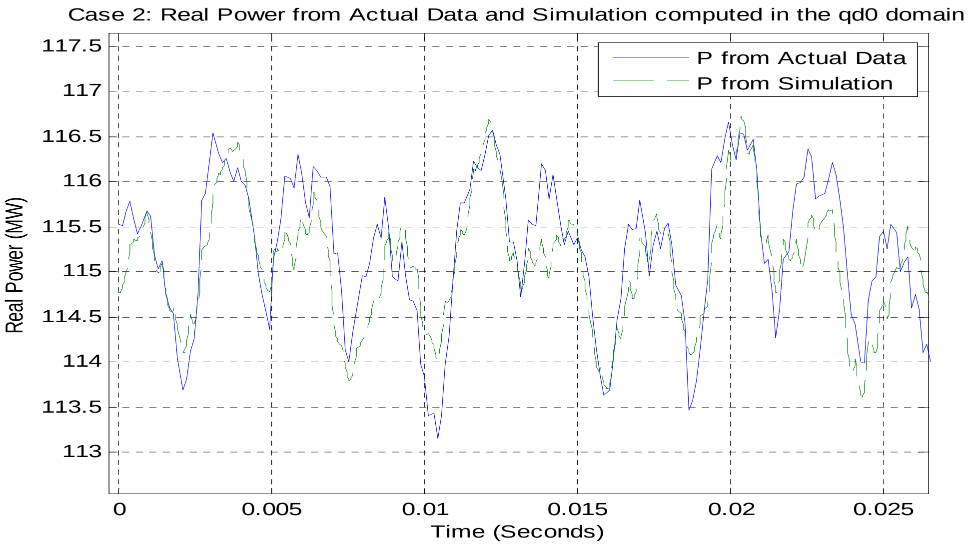

(a) Case V-2: Real Power Comparison: Actual vs. Time-Domain Model

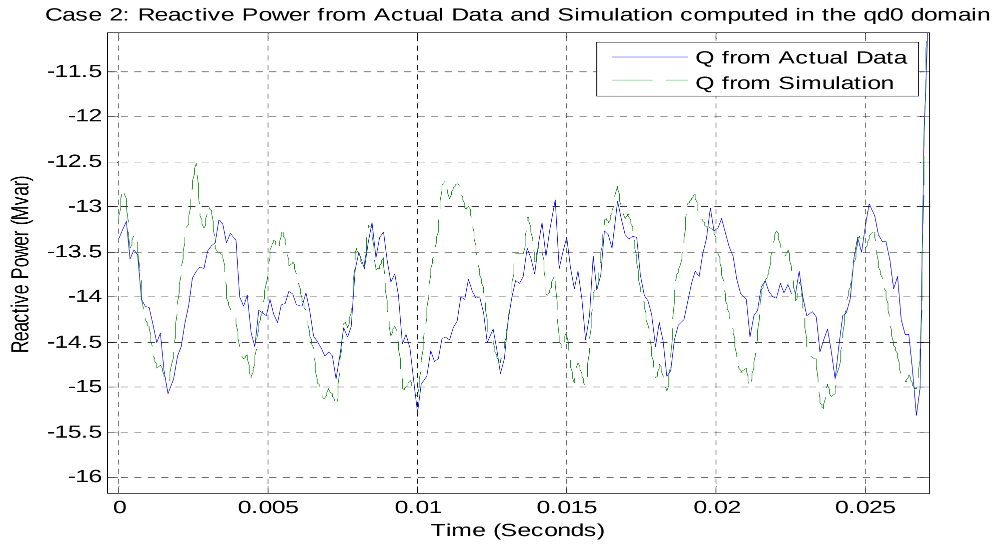

(b) Case V-2: Reactive Power Comparison: Actual vs. Time-Domain Model

Figure 4.6: Case V-2: Pre-fault Real and Reactive Power Comparison: Actual vs. Time-Domain Model

Case V-3

The same analysis was carried out for Case V-3 as well. One cycle of steady-state voltage and current data is shown in Figure 4.7. The calculations for phase A are as follows:

$V_{rms} = 81.77\ kV$

$I_{rms} = 426.94\ A$

$V_{phase} - I_{phase} = -8.56^\circ$

$\mathit{Real\ Power} = V_{rms} \cdot I_{rms} \cdot \cos(V_{phase} - I_{phase}) = 34.52\ MW$

$\mathit{Reactive\ Power} = V_{rms} \cdot I_{rms} \cdot \sin(V_{phase} - I_{phase}) = -5.20\ Mvar$

The three-phase real and reactive power output for Case V-3 can once again be calculated as:

$$\mathit{Three\text{-}Phase\ Real\ Power} = 3 \times 34.52\ MW = 103.57\ MW$$

$$\mathit{Three\text{-}Phase\ Reactive\ Power} = 3 \times -5.20\ Mvar = -15.59\ Mvar$$

The results in Figure 4.8 show that the results from the actual data and the time-domain model match each other closely, as well as matching the estimate from the phasor-domain. The steady-state operation of the time-domain is thus also validated for Case V-3.

For each of the three cases, the real power and reactive power values generated from the actual data and the data extracted from the time-domain model match closely. They also match the values obtained from the phasor-domain calculations. Thus, it can be concluded that the model is functioning

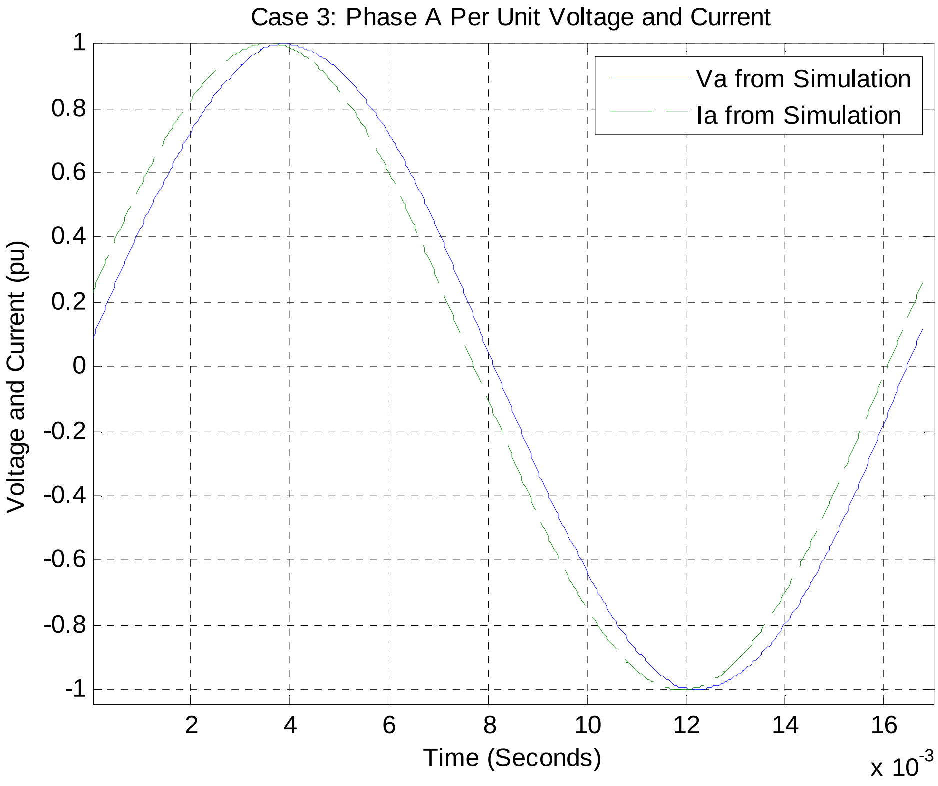

Figure 4.7: Case V-3: One cycle of pre-fault voltage and current data for phase A

correctly in steady-state. The operation of the model during fault time can now be tested for each case as explained in the next section.

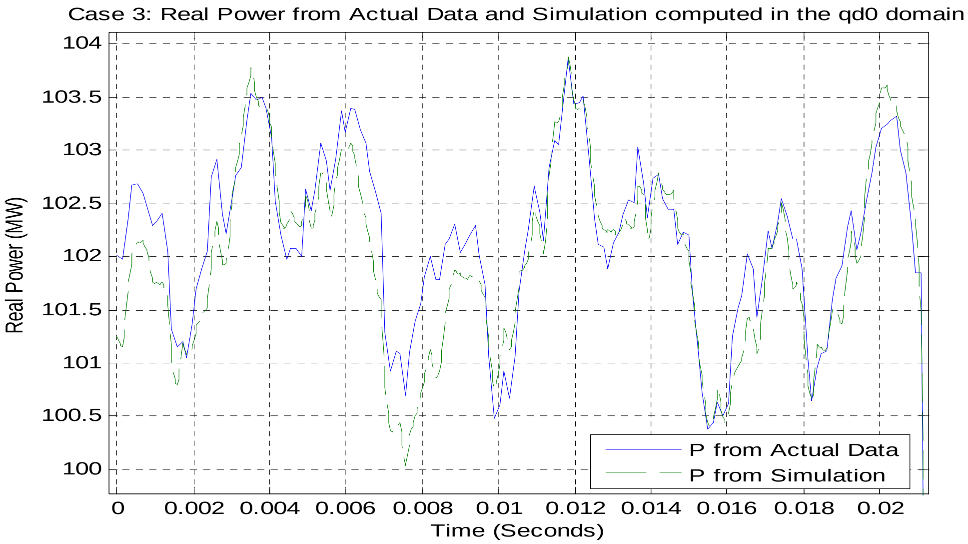

(a) Case V-3: Real Power Comparison: Actual vs. Time-Domain Model

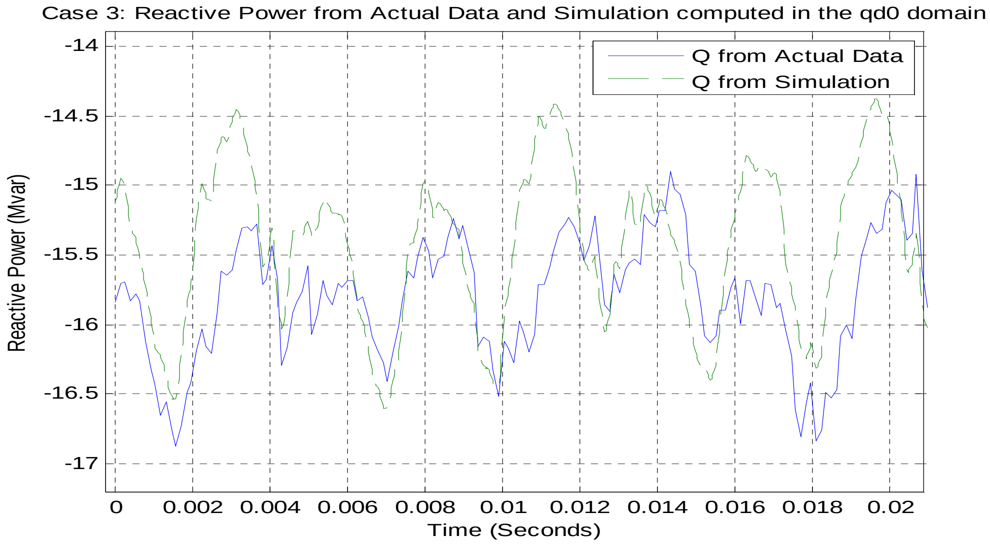

(b) Case V-3: Reactive Power Comparison: Actual vs. Time-Domain Model

Figure 4.8: Case V-3: Pre-fault Real and Reactive Power Comparison: Actual vs. Time-Domain Model

4.4 Dynamic Performance

The process shown in the flowchart in Figure 4.1 is used to evaluate the dynamic performance of the time-domain model during fault conditions. This is repeated for each fault case.

A preliminary check is made by comparing the simulation and actual fault voltages and currents. These waveforms of phase A for one case (Case V-2) are shown in Figure 4.9. It can be seen that the voltages from the actual data and the time-domain model are identical. This shows that the voltage data is being injected correctly into the model. The DC component from the actual voltage data needed to be removed before inputting it to the time-domain model, in order to avoid excessive numerical oscillations. The currents though observed to match closely, are however not identical. This may be due to the fact that the time-domain model is a considerably simplified model of a real-world wind plant. The other two phases for Case V-2 and also all three phases for Cases V-1 and V-3 yielded results in which the matching between actual data and time-domain model data was very close. The matchings are close enough to allow us to proceed with the validation.

The next step is to generate the real and reactive power datasets 1 and 2 from calculations in the $qd0$ domain (refer to Figure 4.1) and plot them together in order to compare the closeness of the match. The results are shown for Case V-1 in Figure 4.10, Case V-2 in Figure 4.11 and Case V-3 in Figure 4.12.

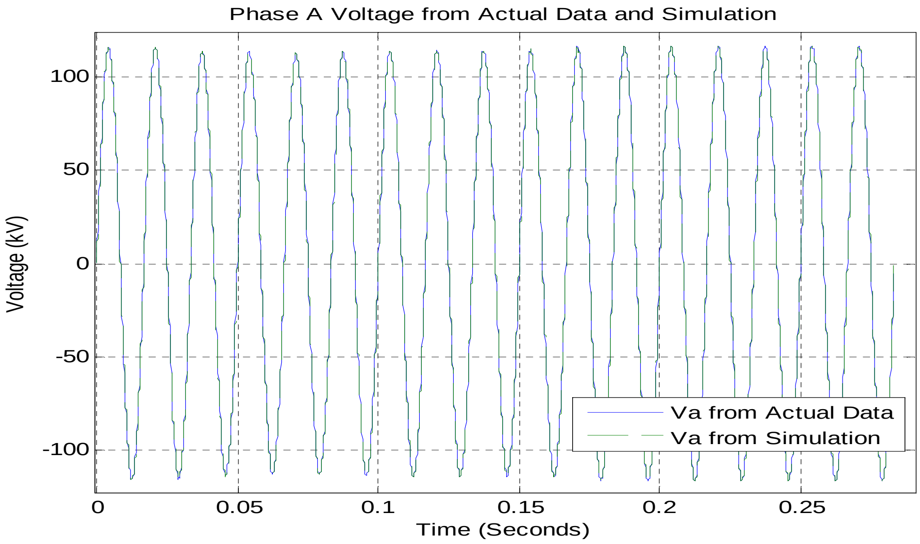

(a) Case V-2: Voltage Comparison for phase A during Fault

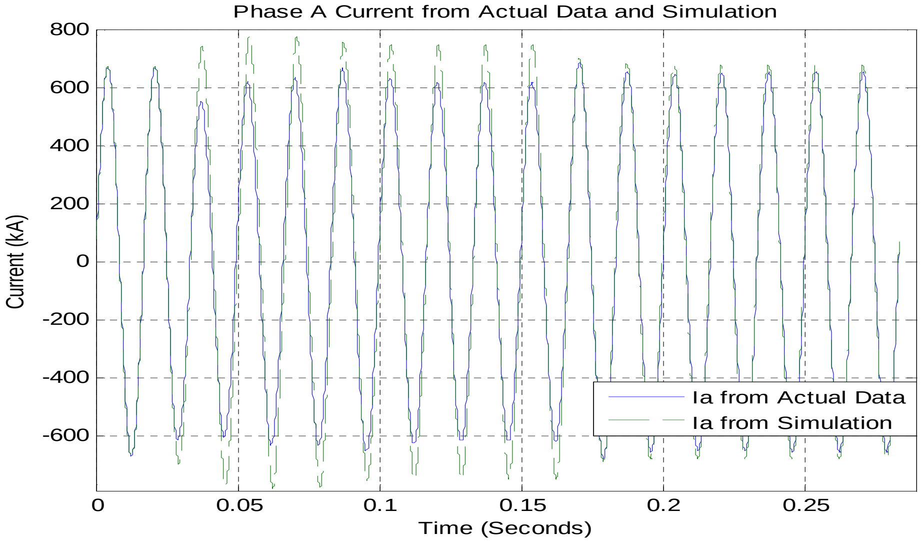

(b) Case V-2: Current Comparison for phase A during Fault

Figure 4.9: Case V-2: Voltage and Current Comparison for phase A: Actual vs. Time Domain Model

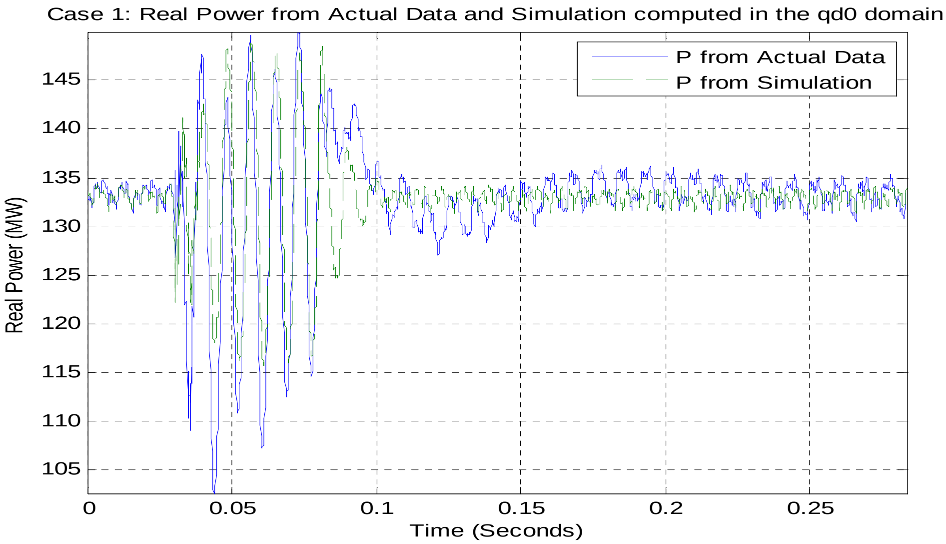

(a) Case V-1: Real power comparison

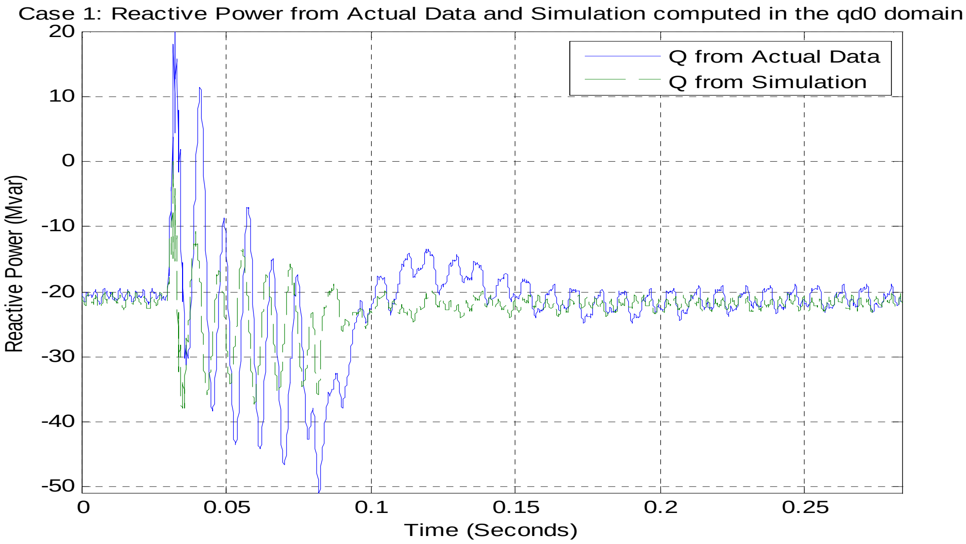

(b) Case V-1: Reactive power comparison

Figure 4.10: Case V-1: Comparison between actual and simulation-based real power and reactive power during fault condition

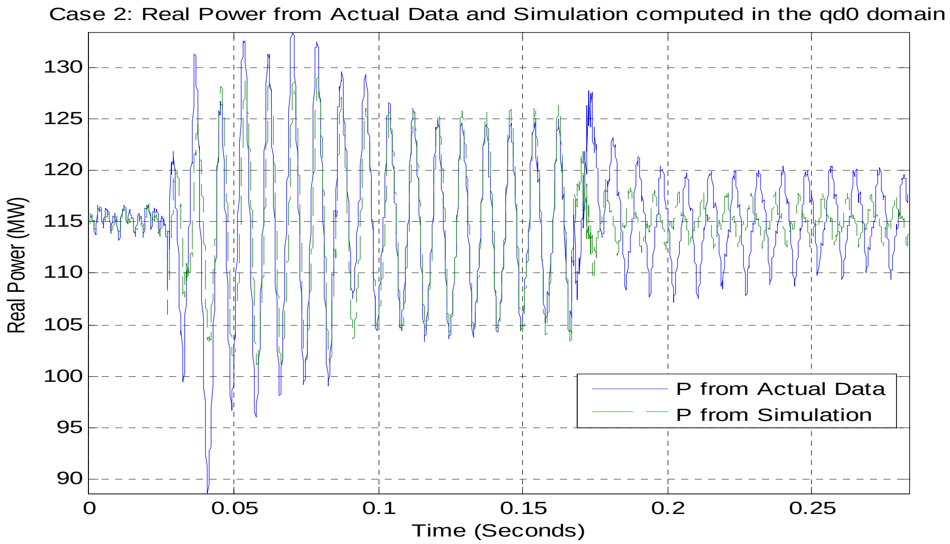

(a) Case V-2: Real power comparison

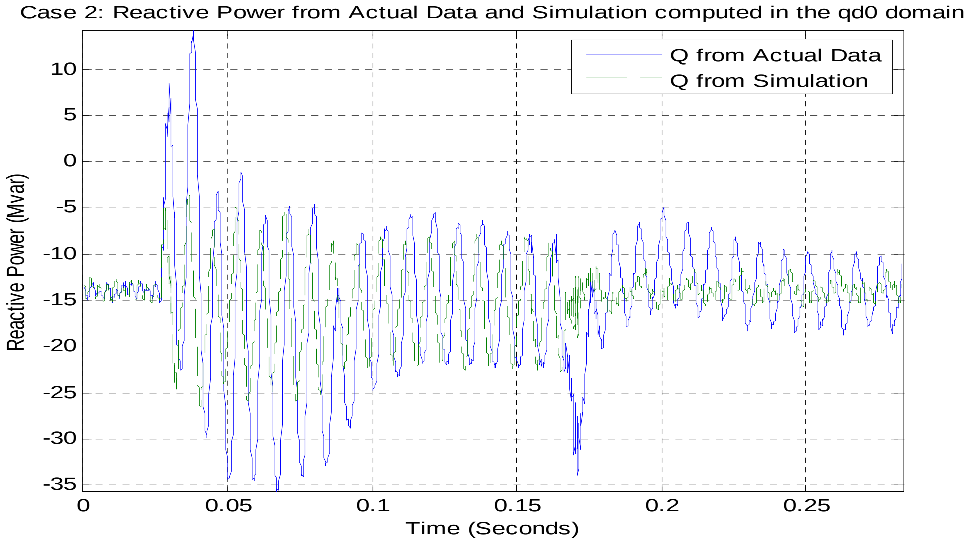

(b) Case V-2: Reactive power comparison

Figure 4.11: Case V-2: Comparison between actual and simulation-based real power and reactive power during fault condition

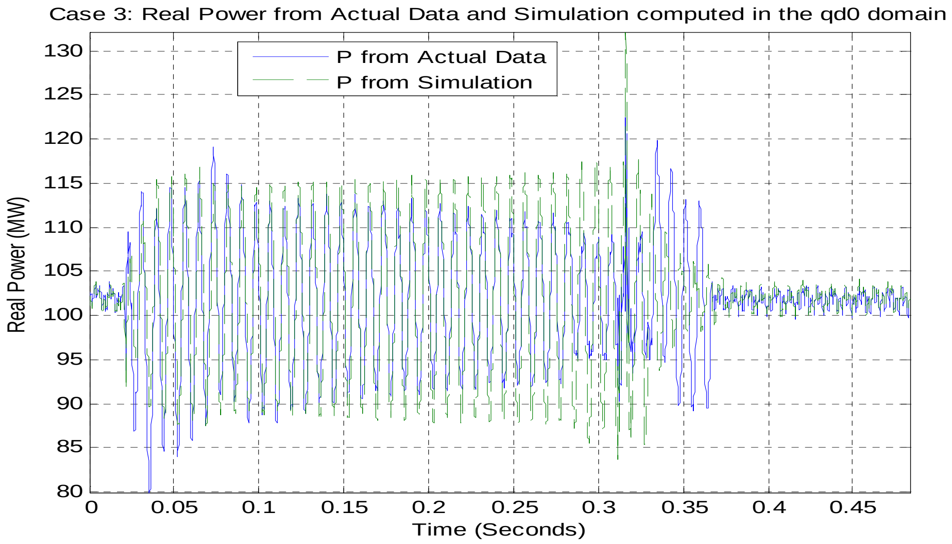

(a) Case V-3: Real power comparison

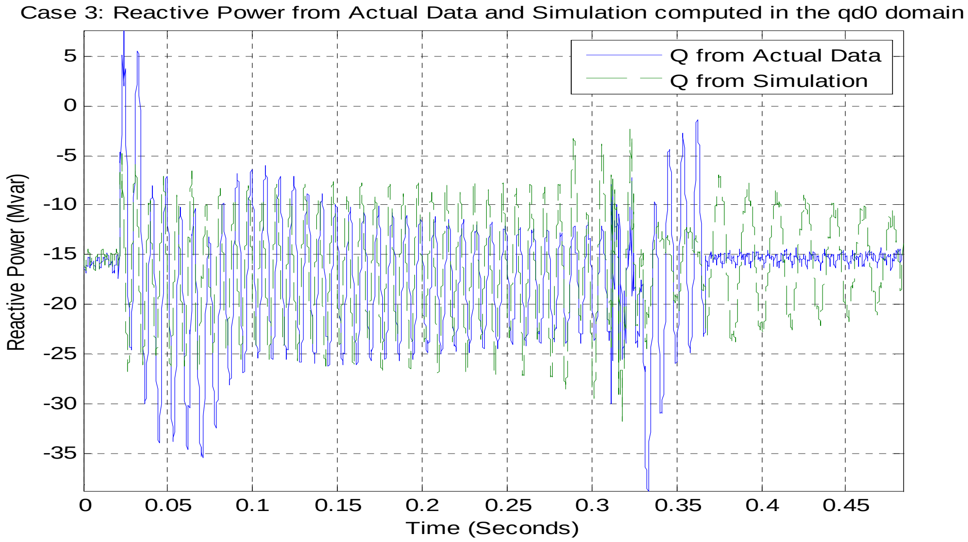

(b) Case V-3: Reactive power comparison

Figure 4.12: Case V-3: Comparison between actual and simulation-based real power and reactive power during fault condition

The results show that for each case, the two datasets match closely, both in magnitude and phase. The model is therefore validated for dynamic studies. It can now be used for fault analysis, since it approximates well the behavior of an actual wind plant under steady-state and fault conditions.

It is to be observed that the real and reactive waveforms from the simulation follow those from the actual data closely but not exactly. There are some small discrepancies between the plots obtained from datasets 1 and 2. The real power plot for Case V-2 (Figure 4.11(a)) is an example of such a discrepancy. In this plot, the power output for both datasets is very similar for the first half of the fault duration. But halfway through the fault, the real power from the actual data begins to lag the real power from the simulation data and remains there till the fault time ends. Such discrepancies seen in the plots may be due to the fact that the induction generator itself is not explicitly modeled, and neither is the power electronic converter. Such simplifications have been made to the time-domain model to preserve its generic nature.

4.4.1 Effect of Proportional Gain on q-axis Current PI Controller

Tuning of the parameters of the PI controllers present in the time-domain model has an impact on the output power and therefore the waveforms obtained from dataset 2 (simulation). In particular, the value of the proportional gain setting on the q-axis current (Iq_cmd) PI controller has a pronounced impact on the real power output from the time-domain model.

For example, consider the fault data from Case V-2. With a low value of gain ($K = 2$), the output response is relatively damped as can be seen in Figure 4.13. Here, the real power calculated during the fault from the time-domain model does not vary as much as that calculated from the actual data. Figure 4.14 shows the improvement in matching when the gain is increased to a high value ($K = 25000$). Thus, a much higher value of gain is seen to improve the response of the controller and match the variation of the output from the actual data. This high value was arrived at by trial and error, and provides good matching for all the fault cases.

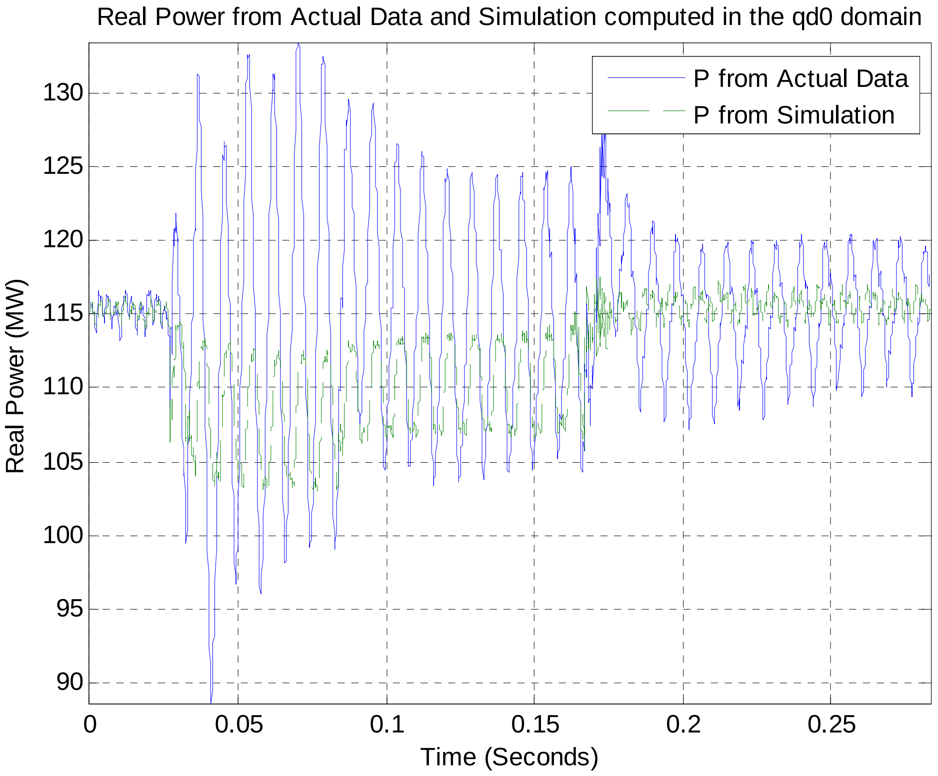

Figure 4.13: Case V-2: Comparison between actual and simulation-based real power during fault condition (controller gain K = 2)

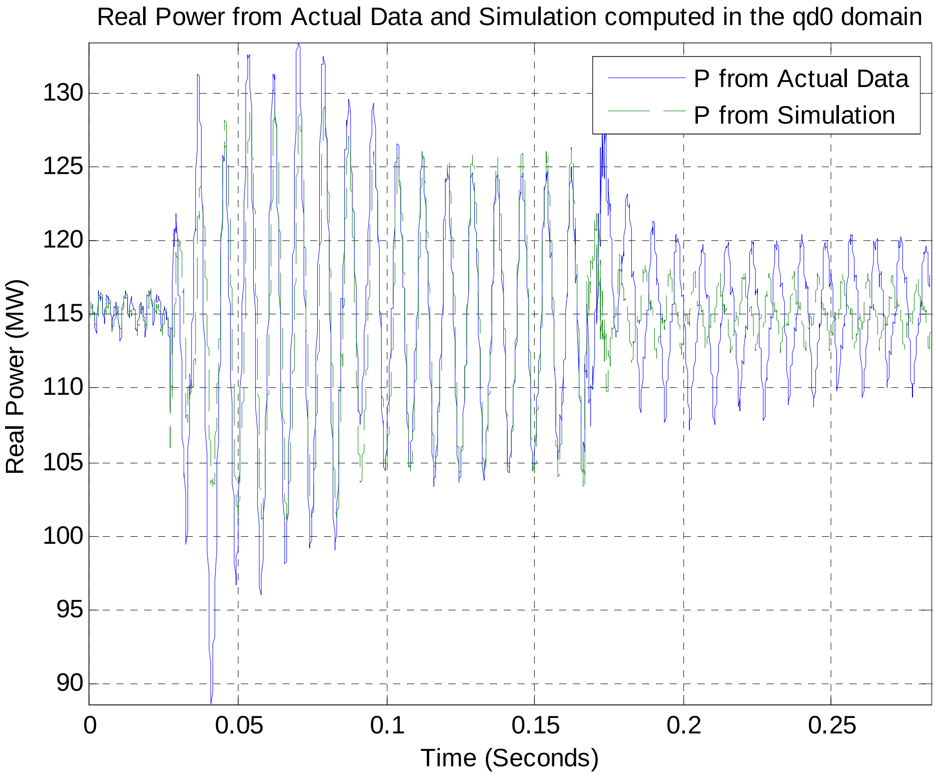

Figure 4.14: Case V-2: Comparison between actual and simulation-based real power during fault condition (controller gain K = 25000)

4.5 Validation of the Time-Domain DFIG Wind Plant Model using Case V-4

Case V-4 is the case where fault data was obtained from the second wind farm that uses DFIG turbines. This data was recorded using line-current differential relays on the high side of the main step-up transformer at the collector substation. The data was accessed using standard relay software on a desktop connected to the wind company's network. The resolution of this data was 4 points/cycle. Interpolation was carried out to achieve the much higher resolution of 128 points/cycle. This data was then used to validate the time-domain model.

The wind farm has a rated real power of 100 MW. The turbines have a rated wind speed of 14.5 m/s. The cut-in and cut-out speeds are 3.5 m/s and 25 m/s respectively. The individual turbine pad-mount transformer ratings as well as the ratings and lengths of all the conductors in the collector system were obtained. These were used to calculate a single equivalent lumped pad-mount transformer rating and lumped collector system impedance. The pad-mount transformers step up the turbine voltage from 575 V to the collector bus voltage of 34.5 kV. The main step-up transformer at the collector sub-station steps up the voltage from 34.5 kV to the transmission voltage of 138 kV. All these parameters were entered into the time-domain model shown in Figure 4.15.

Similar to the other cases, the time-domain model was run until the system reached a steady-state. The fault voltage was then injected at the terminals of the main step-up transformer and the resulting current was observed.

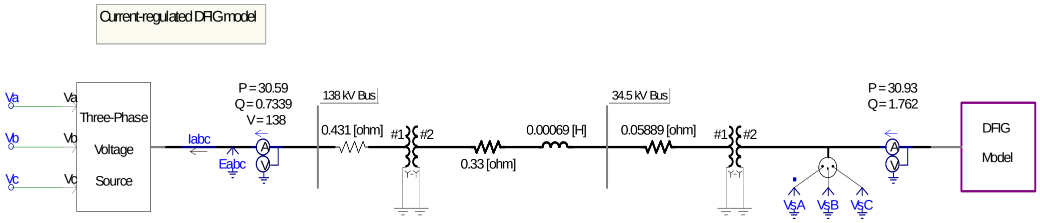

Figure 4.15: Time-domain model for Case V-4

The voltage and current were extracted from the model and compared with the wind farm's data.

The steady-state or pre-fault real and reactive power are compared first. One cycle of the steady-state voltage and current for phase A is shown in Figure 4.16. These are used to perform phasor-domain calculations to obtain the real and reactive power.

The calculations for phase A may be performed as follows:

$V_{rms} = 81.85\ kV$

$I_{rms} = 127.04\ A$

$V_{phase} - I_{phase} = -4.9°$

$Real\ Power = V_{rms} \cdot I_{rms} \cdot \cos(V_{phase} - I_{phase}) = 10.36\ MW$

$Reactive\ Power = V_{rms} \cdot I_{rms} \cdot \sin(V_{phase} - I_{phase}) = -0.887\ Mvar$

Since the voltages and currents are balanced in steady-state, we can assume that the contribution to real and reactive power from phases B and C is the same as that from phase A. The three-phase real and reactive power

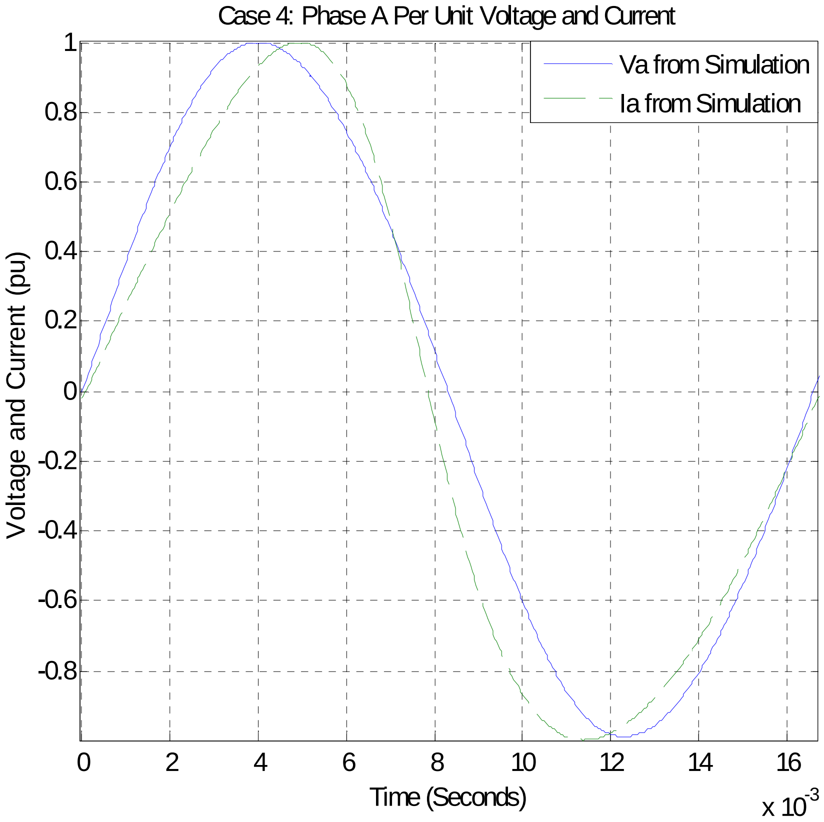

Figure 4.16: Case V-4: One cycle of pre-fault voltage and current data for phase A

output for Case V-1 can be calculated as:

$$\textit{Three-Phase Real Power} = 3 \times 10.36\ MW = 31.08\ MW$$

$$\textit{Three-Phase Reactive Power} = 3 \times -0.887\ Mvar = -2.66\ Mvar$$

Figure 4.17 shows that the results from the actual data and the time-domain model. The pre-fault real power results match each other closely, as

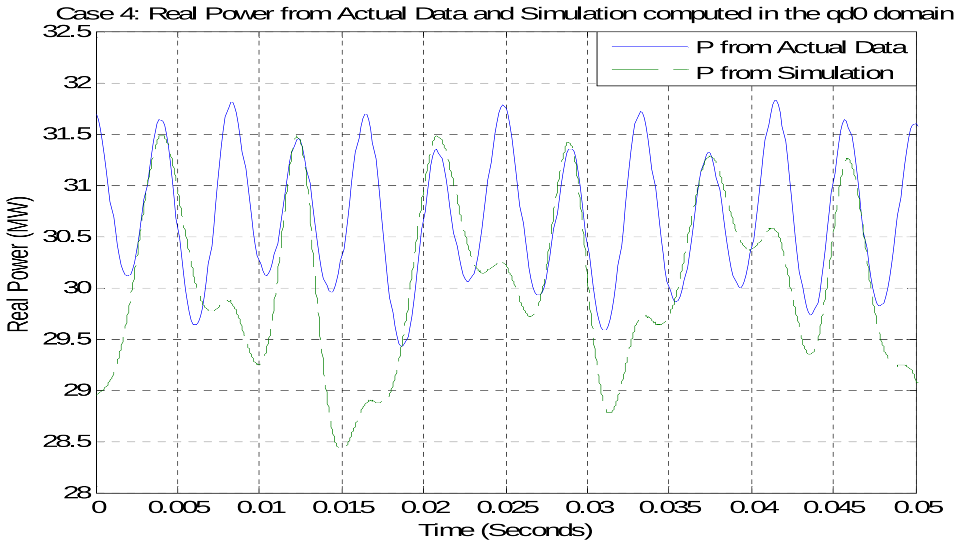
Case 4: Real Power from Actual Data and Simulation computed in the qd0 domain

(a) Case V-4: Real Power Comparison: Actual vs. Time Domain Model

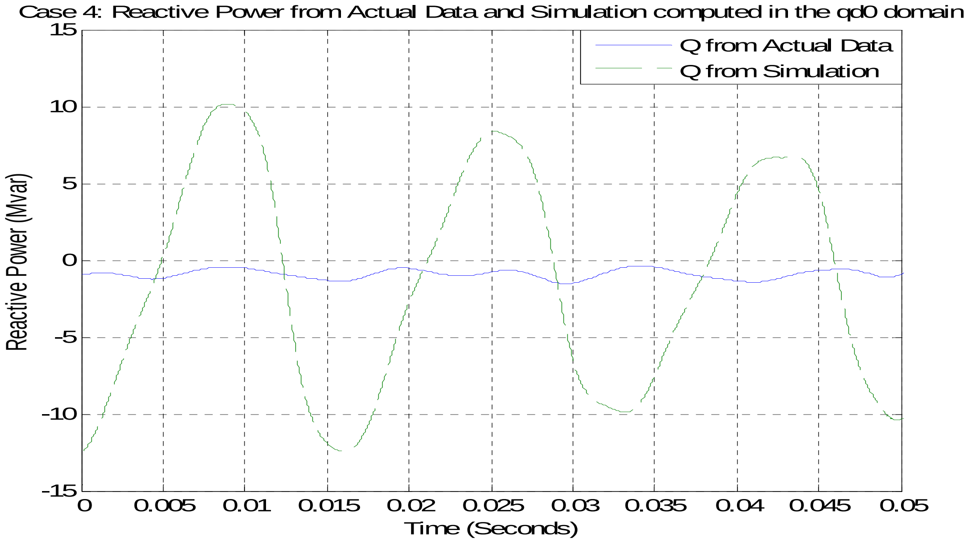
Case 4: Reactive Power from Actual Data and Simulation computed in the qd0 domain

(b) Case V-4: Reactive Power Comparison: Actual vs. Time Domain Model

Figure 4.17: Case V-4: Pre-fault Real and Reactive Power Comparison: Actual vs. Time Domain Model

well as matching the estimate from the phasor-domain. The pre-fault reactive power generated in the simulation is has a much larger amplitude than that from the wind farm. However, its average value matches the pre-fault reactive power from the wind farm as well as the estimate from the phasor-domain. The steady-state operation of the time-domain is thus validated for Case V-4.

As with the other cases, the dynamic performance of the time-domain model during fault conditions is evaluated using the process shown in the flowchart in Figure 4.1.

The simulation and actual fault voltages and currents are first compared as a check. The fault voltage and current waveforms of phase A are shown in Figure 4.18. The voltages from the actual data and the time-domain model are identical. Thus, the voltage data is being inputted correctly into the model. The DC component from the actual voltage data was removed before inputting it to the time-domain model, in order to avoid excessive numerical oscillations. The currents are seen to match closely but are not exactly identical; this may be due to the fact that the time-domain model is a considerably simplified model of a real-world wind plant. The other two phases for Case V-4 also yielded results in which the matching between actual data and time-domain model data was very close. These close matchings allow us to proceed with the validation.

The real and reactive power during the fault are calculated in the $qd0$ domain using the MATLAB script from the simulation and actual data. They are compared as shown in Figure 4.19.

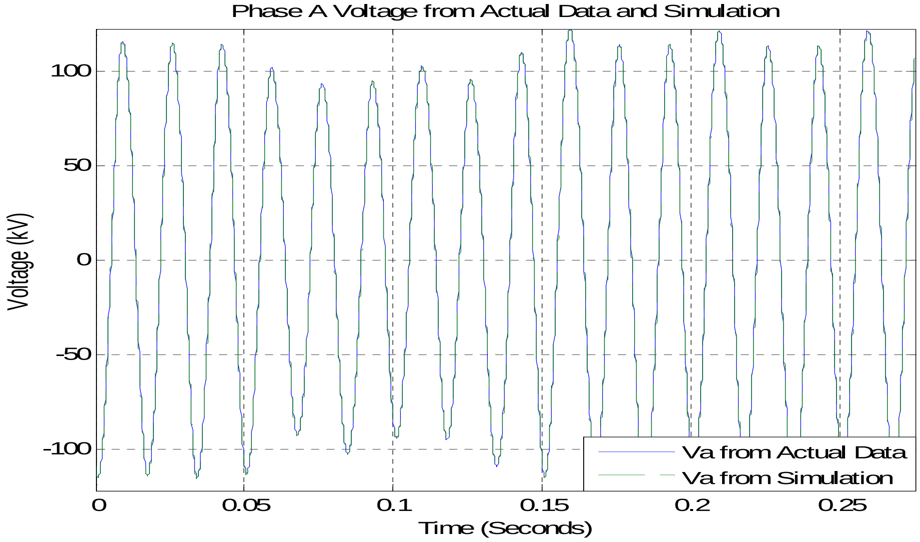

(a) Case V-4: Voltage Comparison for phase A during Fault

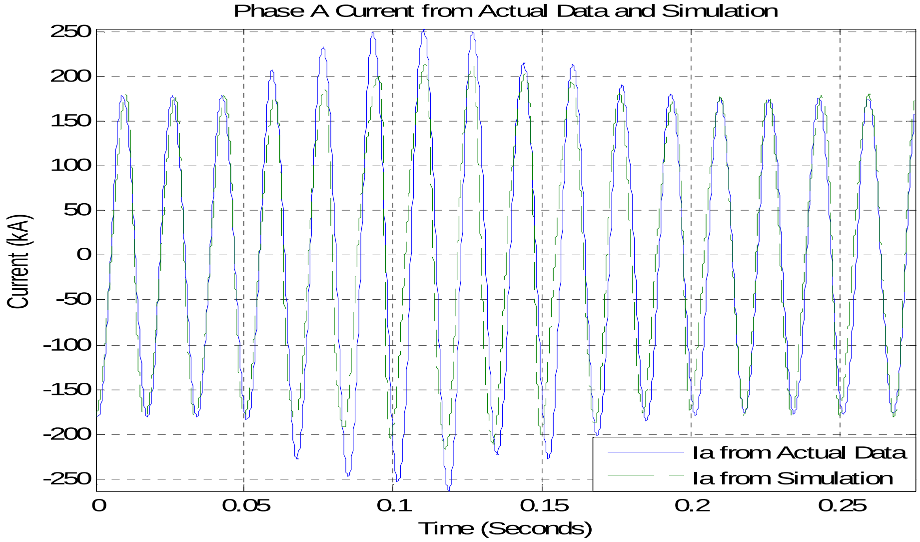

(b) Case V-4: Current Comparison for phase A during Fault

Figure 4.18: Case V-4: Voltage and Current Comparison for phase A: Actual vs. Time-Domain Model

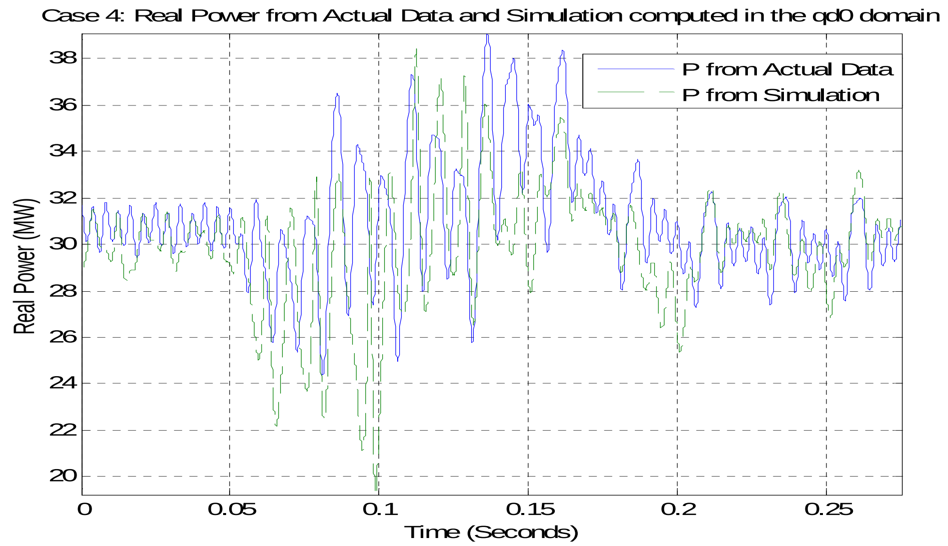

(a) Case V-4: Real power comparison

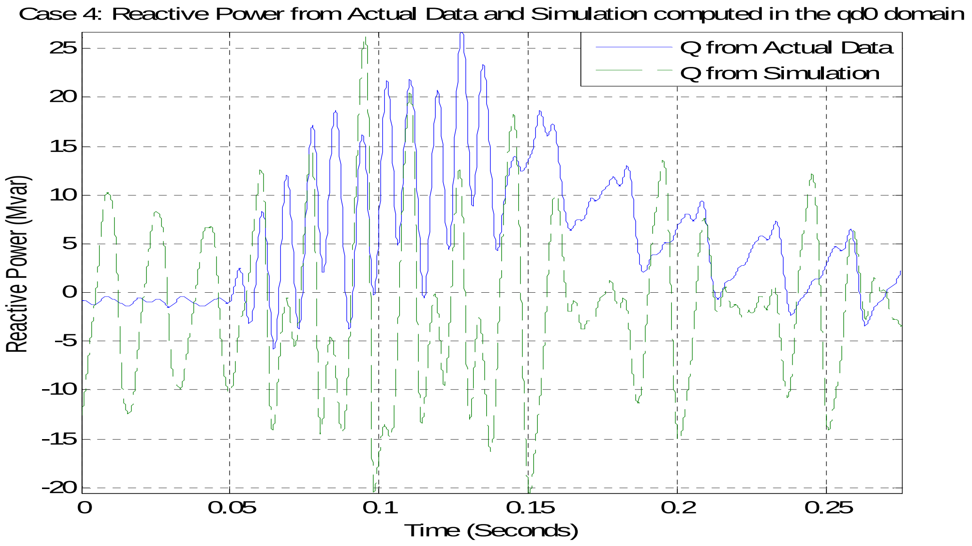

(b) Case V-4: Reactive power comparison

Figure 4.19: Case V-4: Comparison between actual and simulation-based real power and reactive power during fault condition

The results show that for the real power, the two datasets match closely, both in magnitude and phase. The reactive power datasets however, have discrepancies in the magnitude. This can be attributed to the simplifications made to the time-domain model. Thus, the validity of the model has been established for Case V-4 as well. This proves once again that the time-domain model provides a good approximation of the behavior of an actual wind plant under steady-state and fault conditions.

4.6 Summary

This chapter described the validation of the developed time-domain model under four different fault conditions. The model was validated for each case, and the response of the model closely approximated that of a real world DFIG wind farm in each case, both during steady-state and fault conditions. The validation process is thus complete and the time-domain model is ready for use for fault studies.

Chapter 5

Validation of the Positive Sequence DFIG Wind Plant Model

The time-domain model of a wind farm has been discussed in detail in the previous chapters. This chapter explores the phasor-domain or positive-sequence model of the same wind plant. This model is built completely in Simulink. The following sections describe the differences between both these models. The phasor-domain model is subjected to performance tests to validate its steady state operation. Fault analysis is then carried out using the model. The phasor-domain model results are found to match the actual wind farm results to a good extent.

5.1 The Phasor-Domain DFIG Wind Turbine Model

The phasor-domain model has the same building blocks as the time-domain model. That is, it has generator, converter control, wind turbine and pitch control sub-systems that are combined to give the complete model. There are however, a few differences. The voltage input to the system is assumed to be balanced and that only the positive sequence component is present. Hence, the phasor domain model is also called the positive squence model. The system can hence be simplified and represented as a single-phase system rather than the three-phase time-domain system. All the quantities from the time-domain model are accordingly scaled down. The sub-systems used in this model are exactly the same as the time-domain model, except for the generator sub-system. Also, the collector system model is a single-phase equivalent of the three-phase collector system.

5.1.1 Generator Model in Phasor-Domain

The generator sub-system here is completely different as compared to that of the time-domain model. There are no calculations in the $qd0$ reference frame as all quantities are single-phase phasors in this model. Like the time-domain generator model, this model does not include any mechanical state variables for the machine rotor. The quick response of the commands from the converter control sub-system are incorporated by eliminating all flux dynamics from this model [8]. The generator is finally modeled as a controlled-current source that injects the current required by the grid in response to control signals from the real and reactive power control blocks. All the signals in the generator model are in per-unit. The generator sub-system in shown in Figure 5.1.

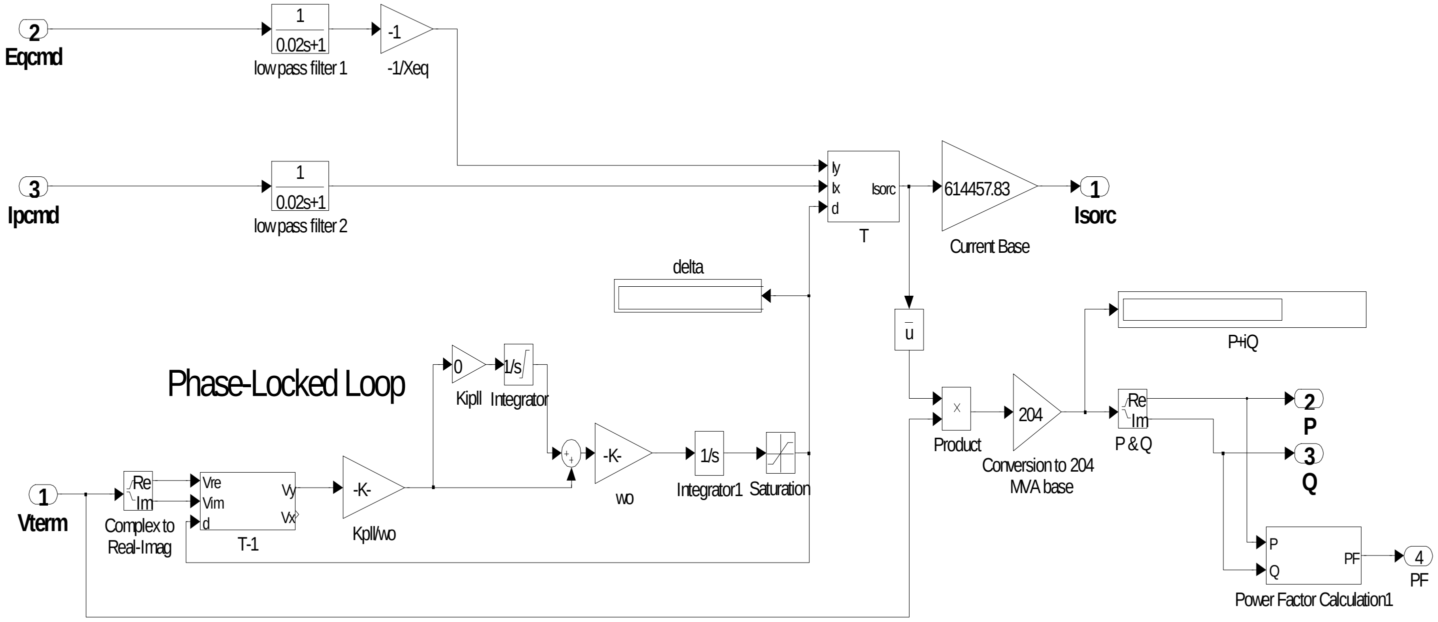

Figure 5.1: Generator sub-system in the phasor-domain model

The generator model receives the *Eqcmd* and *Ipcmd* command signals from the reactive power control and real power control sub-systems respectively. Both these signals are held constant for a given time-step by their respective subsytems in response to the demanded reactive and real power. These signals are passed through low-pass filters that represent the fast electronic control system and high frequency components are eliminated. The *Eqcmd* signal is similar to the *Id_cmd* command signal in the time-domain model. It is the voltage that is required to generate the demanded reactive power. This voltage is divided by the generator's effective equivalent reactance Xeq to give the Y-axis component of the required current Iy as shown in Figure 5.1. Similarly, the *Ipcmd* signal is similar to the *Iq_cmd* signal in the time-domain model. It represents the X-axis component of the current Ix required by the system. There is a phase-locked loop included to synchronize the rotor currents with the stator. The real and imaginary components of the voltage at the wind farm terminals $Vterm$ are used to determine $delta = \delta$, the rotor operating angle. In the steady state, the X-axis of the current is aligned with $Vterm$. Once Ix and Iy are obtained, they are transformed into real and imaginary currents and thus into the phasor-domain using the following transform:

$$\begin{bmatrix} Ire \\ Iim \end{bmatrix} = \begin{bmatrix} \cos(\delta) & -\sin(\delta) \\ \sin(\delta) & \cos(\delta) \end{bmatrix} \cdot \begin{bmatrix} Ix \\ Iy \end{bmatrix} = [T] \cdot \begin{bmatrix} Ix \\ Iy \end{bmatrix} \tag{5.1}$$

The real and imaginary parts of the current are finally combined to give the total current $Isorc$. $Isorc$ is then fed as a control input into a controlled current source (not shown in the figure) which converts it into a proportional current and feeds it to the collector system. All feed-back signals (voltage, real and reactive power, etc) in the complete positive-sequence model are converted into per-unit and then processed. They are therefore multipied by their respective base values before being displayed or injected into the system. The total apparent power S of the system is obtained by the phasor equation:

$$\begin{aligned} S = Vterm \cdot \overline{Isorc} &= (Vterm_{re} + iVterm_{im}) \cdot (Ire - iIim) \qquad (5.2) \\ &= (Vterm_{re} \cdot Ire - Vterm_{im} \cdot Iim) + i(Vterm_{re} \cdot Iim + Vterm_{im} \cdot Ire) \end{aligned}$$

The real power P is defined to be the real part of S and the reactive power Q is defined to be the imaginary part of S. Thus

$$P = Vterm_{re} \cdot Ire - Vterm_{im} \cdot Iim \qquad (5.3)$$

$$Q = Vterm_{re} \cdot Iim + Vterm_{im} \cdot Ire \qquad (5.4)$$

The generator model developed here is connected to the other subsystems as described in Chapter 2 to form the complete positive sequence model. This model is tested in the following sections.

5.2 Performance of the Phasor-Domain Model

The positive-sequence model is subjected to exactly the same tests as the time-domain model. The same initial conditions and inputs are applied and the results are exactly the same as obtained in Chapter 3. Here too, The wind farm is connected to an ideal source. The difference is that the voltage of this source is equal to the per-phase voltage of the time-domain ideal voltage source i.e 79674 Vrms. The results obtained show that the phasor-model provides a good approximation of real-world DFIG wind plant behavior during steady-state and quasi-steady-state operation. They also show that the real and reactive power controls are decoupled.

5.3 Validation of the Phasor-Domain Model

The dynamic response of the positive-sequence model during fault conditions is studied in this chapter. A single phase collector system is connected to the wind farm terminals for this purpose. A controlled voltage source is connected at the other end of this collector system. This voltage source inputs voltage in rms values into the system.

The phasor-model is tested using a single fault case; Case V-2 from the time-domain model study. The real world voltage data for this case is available in rms values as well as true values. These rms values are injected into the phasor-model using the variable voltage source. The base voltage at the wind farm terminals in the time-domain model was 575 Vrms Line-to-Line. Thus, here in the phasor-domain model, the single-phase voltage base at 332 Vrms. The power base is 204 MW. This together with the voltage base causes the current base to be $\frac{204\text{ MW}}{332\text{ Vrms}} = 614.46$ kA. This multiplication factor for the current is shown in Figure 5.1. Here too, the reactive power demand was set to zero and the real power available was set to a fixed value. The model reaches steady state after around 60 seconds. The fault is then applied at 70 seconds and lasts for about 0.27 seconds. During simulation, the model calculates the real and reactive power using Eqn. 5.3. These values are then extracted into MATLAB and plotted against the power calculated from the actual data using the time-domain equations. The results are shown in Figure 5.2

The results show that there is a reasonable degree of matching between the real power waveforms from the actual data and the positive-sequence model. It can be seen though, that during the first half of the fault, the real power waveform from the actual data leads that of the model by a small amount. Whereas, during the next half of the fault, the real power waveform from the actual data lags that of the model. This may be due to the simplification done to the model to keep it generic by eliminating flux dynamics, etc. Also, there is a severe discrepancy in magnitude and phase between the reactive power waveforms from the actual data and the positive-sequence model. The magnitude of the reactive power waveform from the actual data is around five times greater than that of the model throughout the fault. Along with the simplification of the model, this maybe due to the simplification of the reactive elements in the collector system. Thus, during faults, this positive-sequence model is good for analysis of real power only. The three-phase time-domain model from the previous chapters is clearly a much more accurate model than this single-phase phasor-domain model.

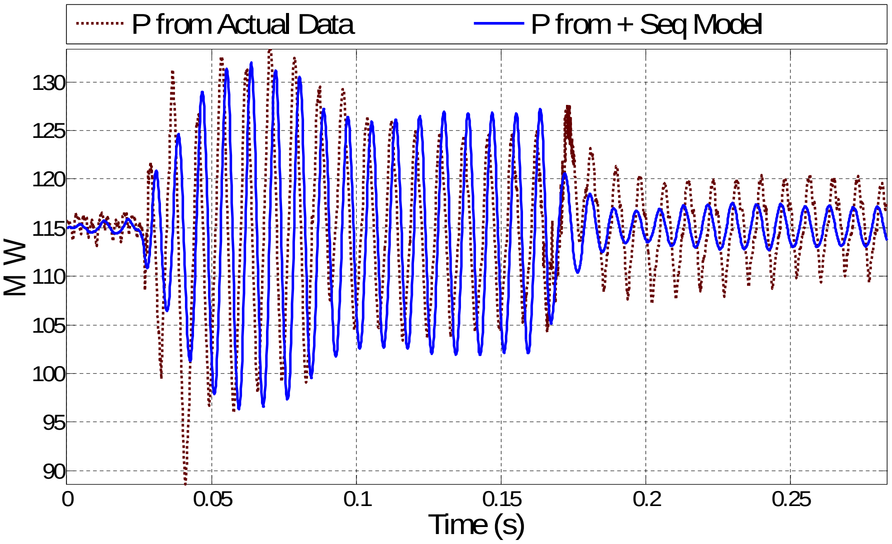

(a) Positive-sequence model real power comparison

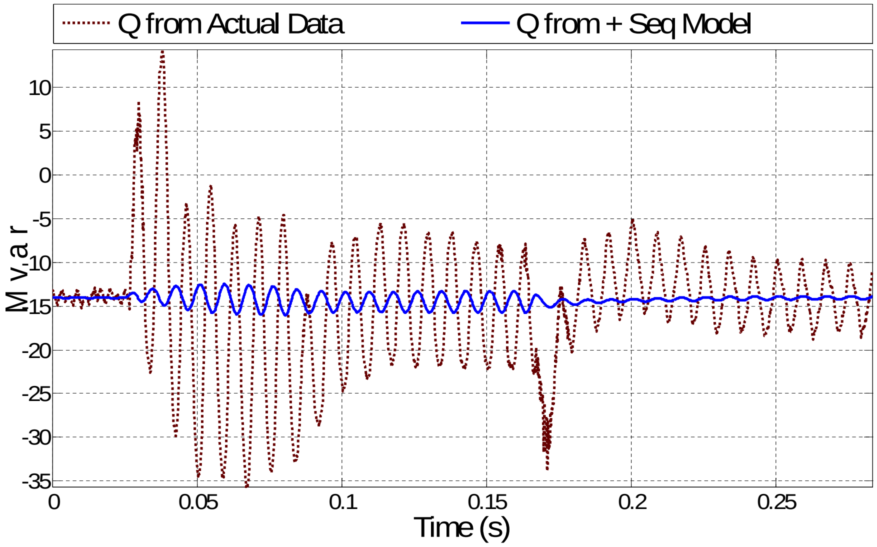

(b) Positive-sequence model reactive power comparison

Figure 5.2: Comparison between actual and positive-sequence model-based real power and reactive power during fault condition

5.4 Summary

This chapter described the modeling of the positive-sequence model of the DFIG-based wind turbine farm. The differences between this phasor-domain model and the time-domain model were discussed. The model was tested to be a good approximation of an actual wind plant during steady-stae and quasi-steady-state operation. Dynamic testing showed that the model is only good for real power analysis during faults. The time-domain model has therefore been shown to be a more accurate model as it approximates an actual wind farm for both real and reactive power analysis during faults.

Appendices

Appendix A

Referral of Rotor Quantities to the Stator

Voltage equations of the following form are obtained for the rotor side of the induction machine from Figure 2.2(b):

$$V_{jr} = r_r \cdot i_{jr} + \frac{d\lambda_{jr}}{dt} \tag{A.1}$$

where the subscript j can be either a, b or c.

Each of the quantities in Eqn. A.1 is referred to the stator side to give a new set of voltage equations as follows. All parameter symbols are the same as in Chapter 2, Section 2.1.1.

Rotor voltages are referred to the stator as

$$[V'_{abcr}] = \begin{bmatrix} V'_{ar} \\ V'_{br} \\ V'_{cr} \end{bmatrix} = \frac{N_s}{N_r} \cdot \begin{bmatrix} V_{ar} \\ V_{br} \\ V_{cr} \end{bmatrix} = \frac{N_s}{N_r} \cdot [V_{abcr}] \tag{A.2}$$

Rotor currents are referred to the stator as

$$[i'_{abcr}] = \begin{bmatrix} i'_{ar} \\ i'_{br} \\ i'_{cr} \end{bmatrix} = \frac{N_s}{N_r} \cdot \begin{bmatrix} i_{ar} \\ i_{br} \\ i_{cr} \end{bmatrix} = \frac{N_s}{N_r} \cdot [i_{abcr}] \tag{A.3}$$

Rotor resistance is referred to the stator as

$$r_r^{'} = \left(\frac{N_s}{N_r}\right)^2 \cdot r_r \tag{A.4}$$

To refer rotor flux linkages to the stator, a little more effort is required. The flux linkages of the machine in matrix notation are as follows:

$$\left[\begin{array}{c} \lambda_{as} \\ \lambda_{bs} \\ \lambda_{cs} \\ \hline \lambda_{ar} \\ \lambda_{br} \\ \lambda_{cr} \end{array}\right] = \left[\begin{array}{ccc|ccc} L_{asas} & L_{asbs} & L_{ascs} & L_{asar} & L_{asbr} & L_{ascr} \\ L_{bsas} & L_{bsbs} & L_{bscs} & L_{bsar} & L_{bsbr} & L_{bscr} \\ L_{csas} & L_{csbs} & L_{cscs} & L_{csar} & L_{csbr} & L_{cscr} \\ \hline L_{aras} & L_{arbs} & L_{ascs} & L_{asar} & L_{asbr} & L_{ascr} \\ L_{bras} & L_{brbs} & L_{bscs} & L_{bsar} & L_{bsbr} & L_{bscr} \\ L_{cras} & L_{crbs} & L_{cscs} & L_{csar} & L_{csbr} & L_{cscr} \end{array}\right] \cdot \left[\begin{array}{c} i_{as} \\ i_{bs} \\ i_{cs} \\ \hline i_{ar} \\ i_{br} \\ i_{cr} \end{array}\right] \qquad \text{(A.5)}$$

Let

$$[\lambda_{abcs}] = \begin{bmatrix} \lambda_{as} \\ \lambda_{bs} \\ \lambda_{cs} \end{bmatrix}, [\lambda_{abcr}] = \begin{bmatrix} \lambda_{ar} \\ \lambda_{br} \\ \lambda_{cr} \end{bmatrix}, [i_{abcs}] = \begin{bmatrix} i_{as} \\ i_{bs} \\ i_{cs} \end{bmatrix} \text{ and } [i_{abcr}] = \begin{bmatrix} i_{ar} \\ i_{br} \\ i_{cr} \end{bmatrix}$$

Then Eqn. A.5 can be compactly written as

$$\begin{bmatrix} [\lambda_{abcs}] \\ [\lambda_{abcr}] \end{bmatrix} = \begin{bmatrix} [L_{ss}] & [L_{sr}] \\ [L_{sr}]^{\mathrm{T}} & [L_{rr}] \end{bmatrix} \cdot \begin{bmatrix} [i_{abcs}] \\ [i_{abcr}] \end{bmatrix} \qquad \text{(A.6)}$$

where from Eqns. 2.10, 2.14, 2.15, 2.17, 2.18, 2.20 and 2.21,

$$[L_{ss}] = \begin{bmatrix} L_{ls} + L_{ms} & -\frac{1}{2}L_{ms} & -\frac{1}{2}L_{ms} \\ -\frac{1}{2}L_{ms} & L_{ls} + L_{ms} & -\frac{1}{2}L_{ms} \\ -\frac{1}{2}L_{ms} & -\frac{1}{2}L_{ms} & L_{ls} + L_{ms} \end{bmatrix}, \qquad \text{(A.7)}$$

$$[L_{sr}] = L_{sr} \cdot \begin{bmatrix} \cos(\theta_r) & \cos(\theta_r + \frac{2\pi}{3}) & \cos(\theta_r - \frac{2\pi}{3}) \\ \cos(\theta_r - \frac{2\pi}{3}) & \cos(\theta_r) & \cos(\theta_r + \frac{2\pi}{3}) \\ \cos(\theta_r + \frac{2\pi}{3}) & \cos(\theta_r - \frac{2\pi}{3}) & \cos(\theta_r) \end{bmatrix} \text{ and} \qquad \text{(A.8)}$$

$$[L_{rr}] = \begin{bmatrix} L_{lr} + L_{mr} & -\frac{1}{2}L_{mr} & -\frac{1}{2}L_{mr} \\ -\frac{1}{2}L_{mr} & L_{lr} + L_{mr} & -\frac{1}{2}L_{mr} \\ -\frac{1}{2}L_{mr} & -\frac{1}{2}L_{mr} & L_{lr} + L_{mr} \end{bmatrix} \qquad \text{(A.9)}$$

Now, using Eqns. 2.9, 2.16 and 2.19, we get

$$L_{ms} = \frac{N_s}{N_r} \cdot L_{sr} \tag{A.10}$$

and

$$L_{mr} = \left(\frac{N_s}{N_r}\right)^2 \cdot L_{ms} \tag{A.11}$$

From Eqn. A.10 $[L_{sr}]$ is transferred to the stator side by premultiplying $\frac{N_s}{N_r}$ to each of its terms as follows:

$$[L'_{sr}] = \frac{N_s}{N_r} \cdot [L_{sr}] = \frac{N_s}{N_r} \cdot L_{sr} \cdot \begin{bmatrix} \cos(\theta_r) & \cos(\theta_r + \frac{2\pi}{3}) & \cos(\theta_r - \frac{2\pi}{3}) \\ \cos(\theta_r - \frac{2\pi}{3}) & \cos(\theta_r) & \cos(\theta_r + \frac{2\pi}{3}) \\ \cos(\theta_r + \frac{2\pi}{3}) & \cos(\theta_r - \frac{2\pi}{3}) & \cos(\theta_r) \end{bmatrix}$$

$$\therefore [L'_{sr}] = L_{ms} \cdot \begin{bmatrix} \cos(\theta_r) & \cos(\theta_r + \frac{2\pi}{3}) & \cos(\theta_r - \frac{2\pi}{3}) \\ \cos(\theta_r - \frac{2\pi}{3}) & \cos(\theta_r) & \cos(\theta_r + \frac{2\pi}{3}) \\ \cos(\theta_r + \frac{2\pi}{3}) & \cos(\theta_r - \frac{2\pi}{3}) & \cos(\theta_r) \end{bmatrix} \tag{A.12}$$

Note that

$$L'_{lr} = \left(\frac{N_s}{N_r}\right)^2 \cdot L_{lr} \tag{A.13}$$

and from Eqn. A.11,

$$L'_{mr} = \left(\frac{N_s}{N_r}\right)^2 \cdot L_{mr} = L_{ms} \tag{A.14}$$

To refer $[L_{rr}]$ to the stator, all its terms are premultiplied with $\left(\frac{N_s}{N_r}\right)^2$ and Eqns. A.13 and A.14 are used to simplify it as follows.

$$[L'_{rr}] = \left(\frac{N_s}{N_r}\right)^2 \cdot \begin{bmatrix} L_{lr} + L_{mr} & -\frac{1}{2}L_{mr} & -\frac{1}{2}L_{mr} \\ -\frac{1}{2}L_{mr} & L_{lr} + L_{mr} & -\frac{1}{2}L_{mr} \\ -\frac{1}{2}L_{mr} & -\frac{1}{2}L_{mr} & L_{lr} + L_{mr} \end{bmatrix}$$

$$\therefore [L'_{rr}] = \begin{bmatrix} L'_{lr} + L_{ms} & -\frac{1}{2}L_{ms} & -\frac{1}{2}L_{ms} \\ -\frac{1}{2}L_{ms} & L'_{lr} + L_{ms} & -\frac{1}{2}L_{ms} \\ -\frac{1}{2}L_{ms} & -\frac{1}{2}L_{ms} & L'_{lr} + L_{ms} \end{bmatrix} \tag{A.15}$$

Using Eqns. A.12 and A.15, Eqn. A.5 can be rewritten with all terms referred to the stator as

$$\begin{bmatrix} [\lambda_{abcs}] \\ [\lambda'_{abcr}] \end{bmatrix} = \begin{bmatrix} [L_{ss}] & [L'_{sr}] \\ [L'_{sr}]^{\mathrm{T}} & [L'_{rr}] \end{bmatrix} \cdot \begin{bmatrix} [i_{abcs}] \\ [i'_{abcr}] \end{bmatrix} \tag{A.16}$$

Therefore using Eqns. A.2, A.3, A.4 and A.16, the rotor voltage equation (Eqn. A.1) can be rewritten with all terms referred to the stator as

$$V'_{jr} = r'_r \cdot i'_{jr} + \frac{d\lambda'_{jr}}{dt} \tag{A.17}$$

where the subscript j can be either a, b or c.

Appendix B

Reference Frames

To simplify calculations, quantities in the stationary *abc* reference frame of the stator of an induction machine are often converted into equivalent quantities in other reference frames. This is because if the reference frame chosen is rotating at synchronous speed, then the time-varying quantities in the stationary *abc* frame become time-invariant in this synchronous reference frame. This conversion process is described below.

Let the following currents be flowing in the three-phase stator windings shown in Figure B.1:

$$i_{as} = I_{max} \cdot \cos\left(\omega t + \theta_a\right) \tag{B.1}$$

$$i_{bs} = I_{max} \cdot \cos\left(\omega t + \theta_a - \frac{2\pi}{3}\right) \tag{B.2}$$

$$i_{cs} = I_{max} \cdot \cos\left(\omega t + \theta_a + \frac{2\pi}{3}\right) \tag{B.3}$$

where

-θ_a is the initial phase of the wave

-ω is the electrical angular velocity

-I_{max} is the amplitude of the sinusoidal wave

The resulting magnetic flux intensities are proportional to their respective

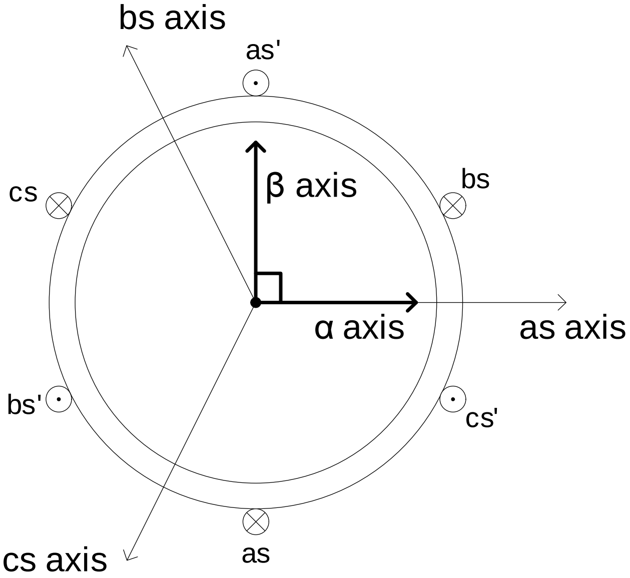

Figure B.1: *abc* stationary axes and $\alpha\beta$ stationary axes on an induction machine

currents. They would be along the fixed *abc* axes as shown in Figure B.1 and expressed as follows:

$$\begin{aligned} H_{as} &= H_{max} \cdot \cos\left(\omega t + \theta_a\right) \angle 0 & &= H_{as}(t)\angle 0 & \text{(B.4)} \\ H_{bs} &= H_{max} \cdot \cos\left(\omega t + \theta_a - \frac{2\pi}{3}\right) \angle{+}\frac{2\pi}{3} & &= H_{bs}(t)\angle{+}\frac{2\pi}{3} & \text{(B.5)} \\ H_{cs} &= H_{max} \cdot \cos\left(\omega t + \theta_a + \frac{2\pi}{3}\right) \angle{-}\frac{2\pi}{3} & &= H_{cs}(t)\angle{-}\frac{2\pi}{3} & \text{(B.6)} \end{aligned}$$

Note these are time varying phasors fixed in space. However, the total magnetic flux intensity obtained by adding the phasors above gives us a rotating magnetic field given by:

$$H_{total} = \frac{3}{2} H_{max} \angle(\omega t + \theta_a) \tag{B.7}$$

Thus, ω is also the constant speed of the rotating magnetic flux. Note the magnitude of this resultant total flux ($\frac{3}{2}H_{max}$) is also constant in time. This rotating flux is subjected to the Clarke Transformation [7], which resolves it into components along two fixed, mutually-perpendicular axes called the α and β axes as shown in Figure B.1. The Clarke Transformation is shown below:

$$\begin{bmatrix} H_\alpha \\ H_\beta \\ H_0 \end{bmatrix} = [T_{abc2\alpha\beta0}] \cdot \begin{bmatrix} H_{as}(t) \\ H_{bs}(t) \\ H_{cs}(t) \end{bmatrix} \tag{B.8}$$

where $[T_{abc2\alpha\beta0}]$ is the Clarke Transform matrix given by

$$[T_{abc2\alpha\beta0}] = \begin{bmatrix} 1 & \cos\left(\frac{2\pi}{3}\right) & \cos\left(\frac{2\pi}{3}\right) \\ 0 & \sin\left(\frac{2\pi}{3}\right) & -\sin\left(\frac{2\pi}{3}\right) \\ \frac{1}{2} & \frac{1}{2} & \frac{1}{2} \end{bmatrix} \tag{B.9}$$

A factor of $\frac{2}{3}$ can be included in the above equation for scaling purposes. The inverse of matrix $[T_{abc2\alpha\beta0}]$ is used to transform quantities from the $\alpha\beta$ frame back to the *abc* frame in what is called the Inverse Clarke Transform.

This rotating flux in the stationary $\alpha\beta$ frame reduces complications in analysis, but the quantities such as inductance etc. are still time-varying. Therefore, to completely solve this problem, a new reference frame rotating at the speed of the rotating flux ω is defined as the $qd0$ reference frame. Its position is measured by the time-varying angle θ_q measured from the positive α axis as shown in Figure B.2.

As the speed of the rotating flux and the $qd0$ frame is the same, the position of the rotating flux is fixed with respect to the q- and d-axes. This causes the resolved components of the rotating flux to be constant along the

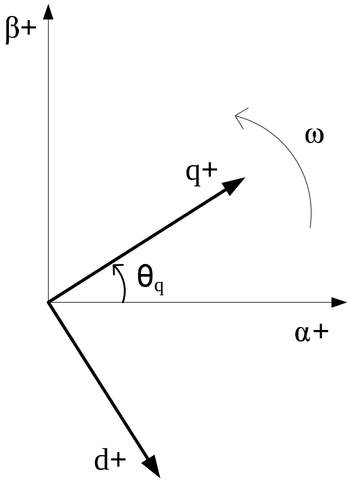

Figure B.2: $qd0$ rotating axes and $\alpha\beta$ stationary axes

q- and d-axes, thus making the quantities time-invariant with respect to the $qd0$ frame. The conversion from the $\alpha\beta$ frame to $qd0$ frame is done as follows:

$$\begin{bmatrix} H_q \\ H_d \\ H_0 \end{bmatrix} = \begin{bmatrix} \cos(\theta_q) & \sin(\theta_q) & 0 \\ \sin(\theta_q) & -\cos(\theta_q) & 0 \\ 0 & 0 & 1 \end{bmatrix} \cdot \begin{bmatrix} H_\alpha \\ H_\beta \\ H_0 \end{bmatrix} \tag{B.10}$$

The total transform from the stationary abc frame to the rotating $qd0$ frame is called the Park Transform. The Park Transform matrix is given by:

$$[T_{abc2qd0}] = \begin{bmatrix} \cos(\theta_q) & \sin(\theta_q) & 0 \\ \sin(\theta_q) & -\cos(\theta_q) & 0 \\ 0 & 0 & 1 \end{bmatrix} \cdot [T_{abc2\alpha\beta 0}]$$

$$\therefore [T_{abc2qd0}] = \begin{bmatrix} \cos(\theta_q) & \cos(\theta_q - \frac{2\pi}{3}) & \cos(\theta_q + \frac{2\pi}{3}) \\ \sin(\theta_q) & \sin(\theta_q - \frac{2\pi}{3}) & \sin(\theta_q + \frac{2\pi}{3}) \\ \frac{1}{2} & \frac{1}{2} & \frac{1}{2} \end{bmatrix} \tag{B.11}$$

Equation B.11 can be used to convert any quantity like voltage, etc. from the abc frame to the $qd0$ frame. However, care must me taken to use the appropriate quantity ω while performing the conversions. It is in this $qd0$ frame that all the processing of signals from the model is done. The required reference current signals are generated and then using inverse transforms converted back into the abc frame as has been explained in the Chapter 2.

Bibliography

[1] S. Santoso, M. Singh, and K. Faria. Modeling and validation of doubly-fed induction generator wind turbines. Technical report, Prepared for NREL by The University of Texas at Austin, September 2008.

[2] M. Singh, K. Faria, S. Santoso, and E. Muljadi. Validation and analysis of wind power plant models using short-circuit field measurement data. In *Power Engineering Society General Meeting, 2009, IEEE*, July 26–30 2009.

[3] S. Santoso and H. T. Le. Fundamental time-domain wind turbine models for wind power studies. *Renewable Energy, An International Journal*, 32:2436–2452, November 2007.

[4] A. Arulampalam, G. Ramtharan, N. Jenkins, V. K. Ramachandaramurthy, J. B. Ekanayake, and G. Strbac. Trends in wind power technology and grid code requirements. In *International Conference on Industrial and Information Systems, 2007. ICIIS 2007*, pages 129–134, August 9-11 2007.

[5] N. W. Miller, J. J. Sanchez-Gasca, W. W. Price, and R. W. Delmerico. Dynamic modeling of ge 1.5 and 3.6 mw wind turbine-generators for stability simulations. In *Power Engineering Society General Meeting, 2003,*

IEEE, volume 3, pages 1977–1983, July 13-17 2003.

[6] P.C. Krause. *Analysis of Electric Machinery.* McGraw Hill Co., New York, 1986.

[7] E.Clarke. *Circuit Analysis of A-C Power Systems*, volume 1. John Wiley & Sons, New York, 1943.

[8] WECC Wind Generator Modeling Group. Generic type-3 wind turbine-generator model for grid studies. Technical Report Version 1.1, Western Electricity Coordinating Council, September 14 2006.

[9] J.F. Manwell, J.G. McGowan, and A.L. Rogers. *Wind Energy Explained.* John Wiley & Sons, 2002.

[10] J.D. Glover and M.S. Sarma. *Power System Analysis and Design.* PWS Publishing Co., Boston, 2nd edition, 1994.

Vita

Keith Joseph Faria was born in Jeddah, Saudi Arabia on the 5th of March 1985, the son of Ronald J. Faria and Petronella T. Faria. He continued his education from the fifth grade onwards in India. He received the Bachelor of Technology degree in Electrical Engineering from the Government College of Engineering, Pune (COEP) in 2007. He applied to the University of Texas at Austin for enrollment in their Electrical Engineering program. He was accepted and commenced graduate studies in September, 2007.

Permanent address: 4210 Red River Street
Austin, Texas 78751

This thesis was typeset with LaTeX[†] by the author.

[†] LaTeX is a document preparation system developed by Leslie Lamport as a special version of Donald Knuth's TeX Program.